High-Energy-Density Physics Experiments of Rayleigh-Taylor Instability Growth at Low-Density-Contrast

by

Laura E. Elgin

A dissertation submitted in partial fulfillment
of the requirements for the degree of
Doctor of Philosophy
(Electrical Engineering)
in The University of Michigan
2019

Doctoral Committee:

Associate Professor Carolyn C. Kuranz, Co-Chair
Assistant Professor Louise Willingale, Co-Chair
Professor R. Paul Drake
Associate Professor Ryan D. McBride
Professor Duncan G. Steel

"I would not give a fig for the simplicity on this side of complexity, but I would give my life for the simplicity on the other side of complexity."

- Oliver Wendell Holmes

Laura Elgin

lelgin@umich.edu

ORCID iD: 0000-0002-1212-5033

ACKNOWLEDGEMENTS

I would like to thank the following organizations and individuals: Lawrence Livermore National Laboratory (LLNL) and the National Nuclear Security Administration (NNSA) for funding this work. All the people at the Laboratory for Laser Energetics (LLE) at the University of Rochester, who made these experiments possible. The Lurie Nanofabrication Facility (LNF) at the University of Michigan for providing the facilities, equipment, and training for specialized metrology of target components. Carlos Di Stefano and Joe Cowan at Los Alamos National Laboratory (LANL) for X-ray metrology scans of target physics packages. My doctoral committee for their mentorship, advice, and feedback on this dissertation. Tim Handy, Rachel Young, and Matt Trantham for numerical simulations.

Sallee Klein deserves special recognition for her skill, technical expertise, creativity, and work ethic in all aspects of target fabrication and for providing logistical support during shot days. Additionally, these experiments would not have been successful without Sallee's excellent company and sense of humor throughout all the long days and nights in the lab and drives between Ann Arbor, MI and Rochester, NY.

On a personal note, I would like to thank my family and friends for their love, support, and understanding, without which I would not have been able to complete this dissertation. In particular: my parents, Susan and Walt Elgin, my sister, Leah Elgin, my dear friends, Liz Dryer, Nicole Pothier McGillivray, Betsy Beckerman, Don Hammond, Linda Alvira, Dina Sheldon, Alisha Niehaus Berger, BJ Baule, and Carla Ahlschwede, and my adorable cat, Sir Winston Furchill.

TABLE OF CONTENTS

LIST OF FIGURES

Figure

LIST OF TABLES

LIST OF APPENDICES

Appendix

LIST OF ABBREVIATIONS

1D one-dimensional

2D two-dimensional

3D three-dimensional

CAD computer-aided design

CHI Iodine-doped polystyrene, $C_{50}H_{47}I_3$

CRF carbonized resorcinol-formaldehyde, $C_{1000}O_{48}H_{65}$

DNS direct numerical simulations

EM electro-magnetic

EOS equation of state

FFT fast Fourier transform

FOV Field-of-view

FWHM full width at half-maximum

HED High-energy-density

ICF inertial confinement fusion

IR infrared

KH Kelvin-Helmholtz

KHI Kelvin-Helmholtz instability

LANL Los Alamos National Laboratory

LES large eddy simulations

LLE Laboratory for Laser Energetics

LLNL Lawrence Livermore National Laboratory

LNF Lurie Nanofabrication Facility

LTE local thermodynamic equilibrium

NIF National Ignition Facility

NIST National Institute of Standards and Technology

NNSA National Nuclear Security Administration

NS Navier-Stokes

ODE ordinary differential equation

PAI polyamide-imide, $C_{22}H_{14}N_2O_4$

PFM pulse-forming module

PI polyimide, $C_{22}H_{10}N_2O_5$

PIV particle-image velocimetry

PLAS Path length adjustment system

PLIF planar laser-induced fluorescence

RANS Reynolds-averaged Navier-Stokes

RID Request identification number

RM Richtmyer-Meshkov

RMI Richtmyer-Meshkov instability

RT Rayleigh-Taylor

RTI Rayleigh-Taylor instability

SNR signal-to-noise ratio

SRF Shot request form

SSD smoothing by spectral dispersion

TIM ten-inch manipulator

UV ultraviolet

WLI white-light interferometer

XRFC X-ray framing camera

XTVS X target-viewing system

YTVS Y target-viewing system

LIST OF VARIABLES

A	Atwood number
c_s	sound speed
C_p	specific heat capacity at constant pressure
C_v	specific heat capacity at constant volume
E_R	radiation energy density
f_m	mass-fraction (of a constituent in a mixed fluid)
f_v	volume fraction (of a constituent in a mixed fluid)
$\boldsymbol{F}_{EM}$	force density due to interaction of charged particles with an EM field
$\boldsymbol{F}_R$	radiative energy flux
$\boldsymbol{g}$	acceleration
I	intensity
k	wavenumber, $\frac{2\pi}{\lambda}$
k_B	Boltzmann constant
l_T	eddy mixing-length
$\ln \Lambda$	Coulomb logarithm
m_p	proton mass
M_at	average atomic mass
M_mol	average molecular mass
p	pressure
p_R	radiation pressure
$\boldsymbol{Q}$	energy flux from heat conduction

t_m	equal-mass time
t_s	shock breakout time
t_T	eddy turn-over time
T	temperature
T_e	electron temperature
T_i	ion temperature
$\boldsymbol{u}$	velocity
Z	average level of ionization
γ	adiabatic index
$\gamma_{_{RT}}$	linear Rayleigh-Taylor growth rate
$\gamma_{_{KH}}$	linear Kelvin-Helmholtz growth rate
Γ	circulation
Δ	(Δ_x, Δ_y, Δ_z, Δ_r) grid size in a numerical simulation
ϵ	specific internal energy
η_{mT}	turbulent mass diffusivity
η_{QT}	turbulent thermal diffusivity
Θ	Young's molecular mix parameter
κ	X-ray opacity (mass-attenuation coefficient) [area/mass]
λ	wavelength (of the Rayleigh-Taylor mode, unless otherwise specified)
λ_{mfp}	mean-free path
μ	dynamic viscosity
μ_{vol}	bulk viscosity
ν	kinematic viscosity
ν_{num}	numerical viscosity
ν_T	turbulent kinematic viscosity (eddy viscosity)
ρ	mass density [mass/volume]
ρ_a	areal mass density [mass/area]

σ	shear stress
$\underline{\boldsymbol{\sigma}}$	viscous stress tensor
σ_{ij}	$\underline{\boldsymbol{\sigma}}$ expressed in Cartesian coordinates with index notation
τ	non-dimensional time scale for Rayleigh-Taylor growth
ϕ	velocity potential, where $\boldsymbol{u} = \nabla\phi$
$\boldsymbol{\omega}$	vorticity

ABSTRACT

This dissertation describes experiments performed at the Omega-60 laser facility to investigate the nonlinear growth stage of the Rayleigh-Taylor instability (RTI) at a low-density-contrast embedded interface initialized with 2D and 3D single-mode sinusoidal perturbations. RTI occurs at the interface between two fluids of different densities when the lower-density fluid pushes the higher-density fluid. Such a system is energetically unstable: a small-amplitude perturbation at the interface evolves into features described as "bubbles" (parcels of light-fluid rising upward) and "spikes" (regions of heavy-fluid falling downward). Bubbles and spikes interpenetrate across the interface, forming a mixed-fluid region which continues to grow, thereby lowering the potential energy of system. This fundamental hydrodynamic instability is encountered throughout nature and engineered systems. In the realm of high-energy-density (HED) physics, RTI occurs in astrophysical phenomena such as supernovae explosions and in the laboratory during implosion of inertial confinement fusion (ICF) capsules. The ability to model and predict the evolution of RTI has important consequences for fundamental scientific understanding and engineering applications.

Theoretical approaches to RTI consider three separate cases: single-mode, multi-mode, and turbulent mixing, which evolve differently. Analytical models successfully predict macroscopic growth rates of the mixed-fluid layer for these three cases under certain conditions, but neglect the small-scale mixing dynamics, which are essential to describing transitional states. To develop reliable predictive capabilities, we must understand how the seed spectrum, density contrast of the two fluids, miscibility,

acceleration history, and Reynolds number affect the evolution of RTI. Experiments with well-controlled initial conditions enable us to isolate and study particular aspects of the problem. Recent classical fluids experiments and numerical simulations investigate the late-nonlinear growth stage of single-mode RTI and dependence on density contrast. At low-density-contrast, single-mode RTI growth appears to reaccelerate, beyond the terminal velocity predicted by potential-flow models. In the late-nonlinear stage, secondary instabilities arise which modify the internal mixing dynamics and growth rate. No existing models describe this stage of RTI growth, where the mixed-fluid region is partially coherent, partially chaotic, but not fully turbulent. The work presented here investigates this regime in a high-energy-density system relevant to astrophysics and ICF.

In this dissertation, I describe experiments performed at Omega-60, a 10-kJ-class laser facility. In this experimental platform, a blast wave drives RTI growth at an embedded interface inside a shock tube. Using dual-axis X-ray radiography, we observed the evolution of the mixed-fluid region from 17-47 ns. Experimentally measured spike- and bubble-front positions are compared with buoyancy-drag models and radiation-hydrodynamics simulations. The experiments at Omega-60 did not sustain acceleration for long enough to drive RTI into the desired regime, but provided valuable information to inform the design of future experiments at the National Ignition Facility, a MJ-class laser facility.

CHAPTER I

Introduction

1.1 High-Energy-Density Physics, Inertial Confinement Fusion, and Laboratory Facilities

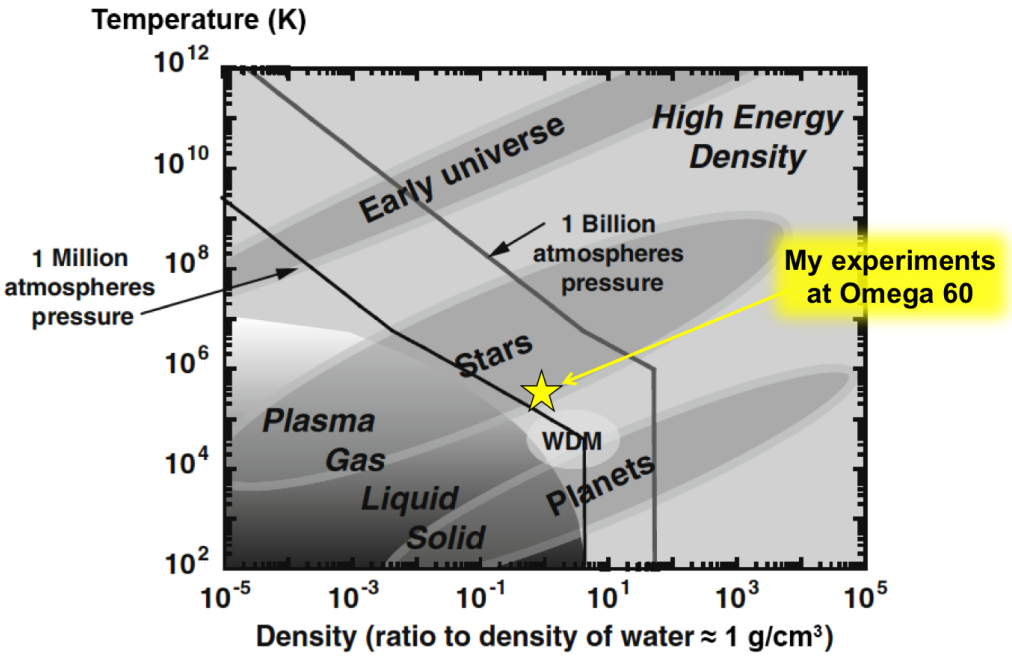

Figure 1.1: Regimes of high-energy-density physics, modified from figure by R.P. Drake [1].

High-energy-density (HED) refers to systems with pressure exceeding 1 Mbar (one million times atmospheric pressure on Earth) [1]. This corresponds to temperatures

high enough to ionize solid-density materials, creating a plasma state too dense to be described by traditional plasma physics. These conditions naturally exist in astrophysical phenomena, such as stars, giant planets, and supernovae, and can be created by human engineering. The first such demonstration was the detonation of a nuclear weapon at the Trinity test site in 1945. At present, the United States nuclear stockpile consists of approximately 4,000 weapons, most of which were built in the 1950s and 1960s. Scientists trained in high-energy-density physics must ensure that this aging stockpile remains safe, secure, and reliable. Modern laboratory facilities can safely create HED conditions on a microscopic scale, where experiments are performed to study the physical phenomena of interest and validate the results of radiation-hydrodynamics simulations, thereby sustaining expertise needed for national security and advancing fundamental scientific knowledge. Research into inertial confinement fusion (ICF) directly supports these goals.

Figure 1.2: National Ignition Facility at Lawrence Livermore National Laboratory [2]

In the United States, there are two large laser facilities designed for ICF. The

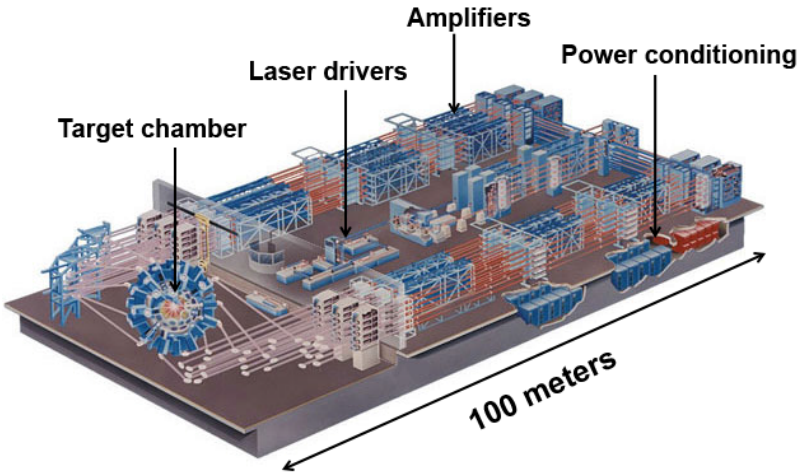

Figure 1.3: Omega-60 Laser Facility at the University of Rochester Laboratory for Laser Energetics [3]

Omega laser facility at the Laboratory for Laser Energetics (LLE) in Rochester, NY enables direct-drive research (Figure 1.3). The National Ignition Facility (NIF), located at the Lawrence Livermore National Laboratory in Livermore, CA, pursues an indirect-drive approach (Figure 1.2). The experiments for this dissertation work were performed in the Omega-60 target chamber at LLE (Figure 1.3). At the center of a spherical chamber, sixty laser beams can focus up to 30 kJ of energy onto a target that measures less than one millimeter in diameter in approximately one billionth of a second. The NIF is an even more energetic facility, with 192 beams delivering 1.8 MJ of laser energy, divided between two beam clusters at opposite poles of the target chamber.

The basic concept of laser-driven ICF is illustrated in Figure 1.4. The spherical capsule consists of a deuterium or tritium fuel core surrounded by a low-atomic-number material shell. High-intensity laser beams (direct drive) or X-rays emitted from a laser-driven hohlraum (indirect drive) irradiate the surface of the shell, rapidly heating it and causing it to explode outward. (This process is also known as "ablation.") In reaction to this force, the remaining capsule material implodes, creating a shock wave that travels inward, thereby compressing and heating the fuel. As it travels through

more mass, the shock wave decelerates and stagnates. The goal is to symmetrically implode the capsule and reach a compression ratio sufficient to ignite a central "hot spot," where nuclear fusion occurs. Thermonuclear chain reactions propagate the burn to the surrounding (cooler) fuel, at a rate much faster than the capsule can expand outward. The hot, dense plasma is confined by the inertia of its own mass.

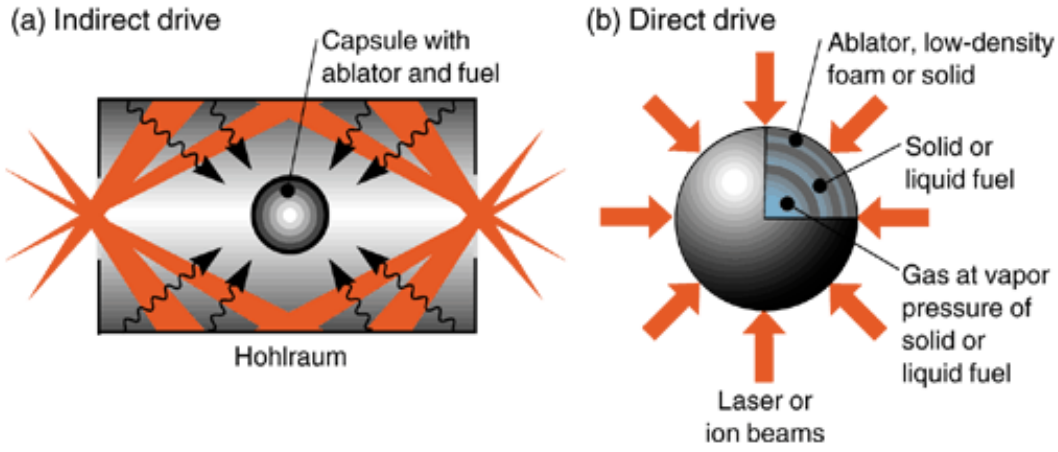

Figure 1.4: Conceptual illustration of the two versions of laser-driven ICF (figure from [4]). (a) For indirect drive, the capsule is positioned in the center a hollow, gold cylinder called a hohlraum. Laser beams enter through both ends of the cylinder and irradiate the interior walls of the hohlraum. The gold material absorbs the laser energy and emits X-rays, which irradiate the capsule from all sides. This is in contrast to direct drive (b), where laser beams configured in a spherical geometry directly irradiate the capsule.

In addition to ICF research, these facilities have enabled "laboratory astrophysics" [5]. Experiments with well-controlled initial conditions allow us to isolate and study physical processes and material properties in astrophysical phenomena. Appropriate temporal and spatial scaling enables comparisons between laboratory results and astrophysical observations [6] [7].

1.2 Notation and Units

Throughout this text, I will use the subscripts $_1$ and $_2$ to denote the denser and less-dense fluids, respectively. Subscripts $_{i,\ e,\ R}$ represent ions, electrons, and the

radiation field, respectively. For example, T_i is the temperature of the ions and p_R is the radiation pressure. The subscript $_T$ denotes turbulent quantities, such as eddy viscosity, ν_T. Variables without these subscripts $\{_{i,\ e,\ R\ ,\ T}\}$ describe bulk-fluid or generalized field properties. I will use italicized text for *scalars* (and in some cases, for unidirectional vectors where the direction is implied by the context), italic-bold for ***vectors***, and italic-bold-underscore for ***tensors*** (rank ≥ 2). Sometimes it is more useful to express tensors in Cartesian coordinates with index notation. For example, $\underline{\boldsymbol{\sigma}}$ and σ_{ij} both refer to the viscous stress tensor (and in this case, the subscript $_i$ is an index and does not refer to ions).

The HED community uses a hybrid system of units because such extreme physical conditions don't translate well to ordinary scales and colloquial language. Numerical computations are typically performed in the centimeter-gram-second (cgs) system of units. Many radiation-hydrodynamics codes specify input/output parameters in cgs units for everything except temperature, which is given in eV. For any system of units, the Boltzmann constant k_B describes the relationship between energy and temperature: $E = k_B\, T$, where $k_B = 8.61733 \times 10^{-5}$ $^{\mathrm{eV}}/_{\mathrm{K}}$. As a rough approximation, 1 eV $\approx 10^4$ Kelvin. For purposes of scientific communication (in conversations, text and figures), pressure and energy density are often given in Mbar or GBar: 1 Mbar $= 10^{11}$ Pa (SI) $= 10^{12}$ Ba (cgs). Spatial and temporal scales are converted to units appropriate for the context (laboratory or astrophysics). For laboratory experiments, we typically use μm and ns. To put this into perspective: $1\,\mu\mathrm{m/ns} = 1\,\mathrm{km/s}$. Electromagnetic radiation in the infrared (IR) to ultraviolet (UV) spectrum is described in terms of wavelength, with units of either μm or nm. In the X-ray spectrum, photon energy is given in units of eV. Laser irradiance is typically given in units of $\mathrm{W/cm^2}$.

1.3 Fluid Description of the HED Plasma

At Omega-60, laser beams (or X-rays emitted from a laser-driven hohlraum) deposit energy in a ~ 1 ns pulse on the surface of a solid target, generating a peak ablation pressure of 10-50 Mbar and launching a strong shock into the target. The post-shock material is a hot ($1 - 100$ eV $\approx 10^4 - 10^6$ K), dense ($\sim 0.1 - 10$ g/cm^3), ionized plasma which behaves as a compressible fluid. The material may be in a state of partial or complete ionization, depending on its atomic composition.

The Navier-Stokes Equations (1.1a, 1.1b, 1.1c) describe the relationship between density, pressure, and internal energy of a moving fluid, and its interaction with external forces. This set of three equations expresses conservation of mass density, momentum density, and energy density. In the non-relativistic limit, the HED plasma can be described by single-fluid equations, where the atomic and ionic species and the electrons move at the same bulk velocity $\boldsymbol{u}$. Further, we assume the material is isotropic, so that it can be described by a scalar pressure p (the total pressure exerted by the ions and the electrons). A more physically accurate picture (which is implemented in the radiation-hydrodynamics code CRASH) uses single-fluid equations for mass and momentum density, but solves separate energy-density equations for electrons, ions, and radiation (using a multi-group diffusive radiation transport model) [8]. For simplicity, here I use a single-fluid energy-density equation and assume the ions and electrons are in local thermodynamic equilibrium (LTE) so that $T_i = T_e = T$:

Mass:
$$\frac{\partial \rho}{\partial t} + \nabla \cdot \rho \boldsymbol{u} = 0 \tag{1.1a}$$

Momentum:
$$\rho\big(\frac{\partial \boldsymbol{u}}{\partial t} + \boldsymbol{u} \cdot \nabla \boldsymbol{u}\big) + \nabla(p + p_R) - \nabla \cdot \underline{\boldsymbol{\sigma}} + \boldsymbol{F}_{\mathrm{EM}} + \boldsymbol{F}_{other} = 0 \tag{1.1b}$$

Energy:
$$\frac{\partial}{\partial t}\big(\rho\epsilon + \frac{\rho u^2}{2} + E_R\big) + \nabla \cdot \big(\rho \boldsymbol{u}\,(\epsilon + \frac{u^2}{2} + p\boldsymbol{u})\big) + ...$$
$$\nabla \cdot \big(\boldsymbol{F_R} + (p_R + E_R)\,\boldsymbol{u} + \boldsymbol{Q} - \underline{\boldsymbol{\sigma}} \cdot \boldsymbol{u}\big) + \boldsymbol{F}_{other} \cdot \boldsymbol{u} = 0 \tag{1.1c}$$

where ρ is mass density, ϵ is specific internal energy, p_R is radiation pressure, E_R is radiation energy density, $\boldsymbol{F}_{\mathrm{EM}}$ is force density due to interaction of charged particles with an electro-magnetic (EM) field, $\boldsymbol{F}_R$ is radiative energy flux, $\boldsymbol{Q}$ is energy flux from heat conduction, $\underline{\boldsymbol{\sigma}}$ is the viscous stress tensor, and $\boldsymbol{F}_{other}$ encompasses all other forces acting on the system. (As a relevant example, $\boldsymbol{F}_{other}$ may include $\rho\boldsymbol{g}$, where $\boldsymbol{g}$ is gravity).

For the class of experiments considered here, there is no externally applied magnetic field and the plasma is strongly collisional. By design (choice of materials and laser drive parameters), the post-shock fluid temperature is low enough so that material energy flux greatly exceeds energy flow by heat conduction and radiation flux. Under these conditions, classical hydrodyanmic behavior dominates [7]. The Euler Equations (1.2a, 1.2b, 1.2c) constitute a simplified version of the Navier-Stokes equations for the case where viscosity and thermal conductivity are negligible:

$$\frac{\partial \rho}{\partial t} + \nabla \cdot \rho \boldsymbol{u} = 0 \tag{1.2a}$$

$$\rho\big(\frac{\partial \boldsymbol{u}}{\partial t} + \boldsymbol{u} \cdot \nabla \boldsymbol{u}\big) + \nabla p = 0 \tag{1.2b}$$

$$\frac{\partial}{\partial t}\big(\rho\epsilon + \frac{\rho u^2}{2}\big) + \nabla \cdot \big(\rho \boldsymbol{u}\,(\epsilon + \frac{u^2}{2} + p\boldsymbol{u})\big) = 0 \tag{1.2c}$$

From here, we can see that a closure problem exists: three equations with four state variables $(\rho, \boldsymbol{u}, p, \epsilon)$. The equation of state (EOS) describes the thermodynamic relationship between these variables and provides closure to the Euler Equations.

1.3.1 Equation of State

For simple analytic calculations and conceptual understanding, an HED plasma can be modeled as ideal polytropic gas with EOS:

$$p = \frac{\rho(1+Z)k_B T}{M_{\rm at} m_p} \tag{1.3}$$

$$\epsilon = \frac{n}{2}\frac{(1+Z)k_B T}{M_{at} m_p} = \frac{p}{\rho(\gamma-1)} \tag{1.4}$$

$$c_s^2 = \left(\frac{\partial p}{\partial \rho}\right)_s = \gamma\frac{p}{\rho}, \text{ where the derivatitive is taken at constant entropy} \tag{1.5}$$

Here, $M_{\rm at}$ is the average atomic mass (of the ions), Z is the average level of ionization, m_p is the proton mass, n is the number of degrees of freedom, c_s is the sound speed, and the adiabatic index γ is the ratio of specific heat capacities:

$$\gamma \equiv \frac{C_p}{C_{\rm v}} = \frac{\frac{\partial \epsilon}{\partial T}\big|_p}{\frac{\partial \epsilon}{\partial T}\big|_{\rm v}} = 1 + \frac{2}{n} \tag{1.6}$$

where C_p, $C_{\rm v}$ are the specific heat capacities at constant pressure and volume, respectively. In the simplest approximation, γ is constant. For an ideal gas, $\gamma = 5/3$ and for a radiation-dominated plasma $\gamma = 4/3$ [1]. In reality, the polytropic gas EOS is a poor approximation to describe a partially ionized HED plasma. A more physically accurate model might involve other physical effects, such as Coulomb energy corrections, degenerate electrons, pressure ionization, continuum lowering, and the impact of bound electrons [1]. The situation becomes even more complicated in dynamic HED systems, where the materials transition through many different states.

Radiation-hydrodynamics simulations employ material-specific tabular equations of state. An EOS table specifies two of the thermodynamic variables (ρ, p, ϵ, T) in terms of the other two, for a discrete set of values. A computer algorithm then interpolates between the tabulated values to calculate the state of the system throughout the

simulation. Each EOS table is the product of extensive research efforts, incorporating limited experimental data, physics models, and molecular dynamics simulations. A given EOS only applies for a specific range of conditions (ρ, p, ϵ, T). When merging models that cover adjacent regimes, it can be difficult to maintain thermodynamic consistency (not violate the first law of thermodynamics). For many materials, no data exists and the EOS for a different material is applied.

1.3.2 Viscosity

Viscosity is the property of a fluid which characterizes its resistance to deformation. Conceptually, if adjacent layers within a fluid are in relative motion, a frictional force arises between the layers which resists their relative motion. Viscosity measures the strength of this internal force. Figure 1.5 illustrates the simple case of planar parallel flow of a Newtonian fluid. Here, the relative motion of the fluid layers is along the x-direction ($\boldsymbol{u} = u_x$). The dynamic viscosity μ is defined by Equation 1.7, which is known as Newton's law of viscosity:

$$\sigma = \mu \frac{\partial u_x}{\partial y} \tag{1.7}$$

where σ is the shear stress and $\partial u_x / \partial y$ is the local shear velocity (or strain rate).

More generally, viscous stresses occur in all directions, resulting from the relative motions of different fluid particles throughout the fluid. The viscous stress tensor $\underline{\boldsymbol{\sigma}}$ expresses the generalized form of Newton's law of viscosity:

$$\underline{\boldsymbol{\sigma}} = \mu[\nabla \boldsymbol{u} + (\nabla \boldsymbol{u})^{\dagger}] - (\frac{2}{3}\mu - \mu_{\text{vol}})(\nabla \cdot \boldsymbol{u})\underline{\boldsymbol{\delta}} \tag{1.8}$$

where $\underline{\boldsymbol{\delta}}$ is the unit tensor, the symbol † represents the transpose operator, the dynamic viscosity μ is the same scalar quantity as above, and μ_{vol} is the bulk (or volume) viscosity. The bulk viscosity represents a type of internal friction which resists

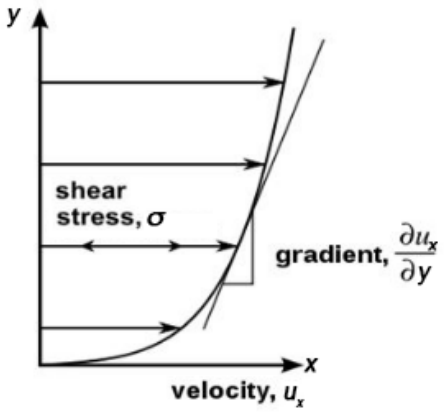

Figure 1.5: Illustration of Newton's law of viscosity in planar parallel flow (modified from figure by [9]).

non-shear compression or expansion. For example, μ_{vol} can be significant during shock-compression of a fluid. In classical fluids, this term can often be neglected. For a monoatomic gas, $\mu_{\text{vol}} = 0$. For an incompressible fluid, $\nabla \cdot \boldsymbol{u} = 0$, so the second term in Equation 1.8 drops out. Expressed in Cartesian coordinates with index notation, the viscous stress tensor (Equation 1.8) for an incompressible fluid becomes:

$$\sigma_{ij} = \mu\Big(\frac{\partial u_i}{\partial x_j} + \frac{\partial u_j}{\partial x_i}\Big) \tag{1.9}$$

The kinematic viscosity is defined as:

$$\nu \equiv \frac{\mu}{\rho} \tag{1.10}$$

Dynamic viscosity μ has units of [pressure $\cdot$ time] and kinematic viscosity ν has units of [area/time].

Viscosity can also be viewed from the perspective of kinematic transport theory: ν is the fluid property which measures momentum transport. Shear stress σ has units of pressure, which is equivalent to the units of momentum flux. In gases, viscosity arises primarily from molecular diffusion, which transports momentum within the flow. For

a low-density gas [10]:

$$\nu \approx \lambda_{\text{mfp}} \sqrt{\frac{2k_B T}{\pi M_{\text{mol}}}} \tag{1.11}$$

where λ_{mfp} is the mean-free path of the molecules and M_{mol} is the average molecular mass.

In an HED plasma, the kinematic viscosity is usually small and can be ignored in many applications. However, the physical mechanism of viscous dissipation stabilizes small-scale fluctuations in a boundary-layer flow. As will be explained in Chapter II, this situation relates to the late-stage growth of RTI, where a boundary layer develops between adjacent spikes and bubbles. A transition from laminar to turbulent flow is only possible above a critical Reynolds number, which corresponds to very small kinematic viscosity. To predict this regime, we require a model for kinematic viscosity.

Braginskii's formula is often used due to its simplicity. This model applies to unmagnetized, low density, high temperature, single-ion-species plasmas with weak ionic coupling [11]:

$$\nu \ [\text{cm}^2/\text{s}] \ = 3.3 \times 10^{-5} \frac{M_{\text{at}}^{1/2} \, T_i^{5/2} [\text{eV}]}{\ln \Lambda \, Z^4 \, \rho \ [\text{g/cm}^3]} \tag{1.12}$$

where M_{at} is the average atomic mass of the ions, Z is the average level of ionization, and $\ln \Lambda$ is the Coulomb logarithm. Unlike a classical fluid, the level of ionization strongly influences the kinematic viscosity. The more complicated model of Clérouin *et al.* (found in [12]) provides a more accurate estimate of kinematic viscosity for denser plasmas with mixing between two ionic species. Irrespective of the choice of model, the plasma parameter inputs cannot be measured experimentally and are predicted from numerical simulations. Therefore, uncertainty in the EOS compounds uncertainty in the kinematic viscosity.

(a)

(b)

(c)

Figure 1.6: Examples of vortices found in nature: (a) Tornadoes [13]; (b) Whirlpools on the surface of the ocean [14]; (c) Flow structures created by the passage of an airplane wing (in this image, revealed by colored smoke) [15]

1.4 Vorticies and Turbulence

In this section, I wish to clarify the terminology and what is meant by "vorticity," "circulation," "a vortex", and "an eddy." All four terms describe circular motion within a flow. Vorticity and circulation have specific mathematical definitions; whereas vortices and eddies are conceptual descriptions of rotational structures and the distinction between them is subtle. The eddy description arises primarily in the context of turbulence. A detailed discussion of turbulence is beyond the scope of this dissertation. I will merely introduce the concepts of eddy viscosity and turbulence models, so that their meanings are clear in subsequent chapters.

1.4.1 Vorticity and Circulation

Vorticity is the curl of the velocity field:

$$\boldsymbol{\omega} \equiv \nabla \times \boldsymbol{u} \tag{1.13}$$

The circulation Γ quantifies the amount of fluid rotation within a closed curve C:

$$\Gamma \equiv \oint_C \boldsymbol{u}\, d \cdot \boldsymbol{s} = \int_A \boldsymbol{\omega} \cdot \boldsymbol{n}\, dA \tag{1.14}$$

where $d\boldsymbol{s}$ is a differential line element along C, A is the surface bounded by the curve C, and $\boldsymbol{n}$ is the unit vector perpendicular to A. The second equality follows from Stokes' theorem and the definition of vorticity.

Baroclinicity quantifies the alignment between the pressure gradient and the density gradient in a stratified fluid:

$$\frac{1}{\rho^2} \nabla\rho \times \nabla p \tag{1.15}$$

In a barotropic fluid, the surfaces of constant density and the surfaces of constant pressure coincide (baroclinicity equals zero). In a baroclinic fluid, these surfaces intersect [16]. Kelvin's theorem states that in a flow with conservative body forces and inviscid, barotropic fluids, the circulation around a closed curve moving with the fluid is constant:

$$D\Gamma/Dt = 0 \tag{1.16}$$

where $D/Dt = \partial/\partial t + \boldsymbol{u} \cdot \nabla$ is the material derivative. The converse of Kelvin's theorem is also true, revealing the three ways to create or destroy vorticity in a flow [17]:

1. Non-conservative body forces. The Coriolis acceleration (which occurs in rotating frames of reference) is an example of a non-conservative force that generates

vorticity. Dissipative forces (such as friction) destroy vorticity.

2. A non-barotropic pressure-density relationship. This is the source of vorticity in the Richtmyer-Meshkov instability.

3. Non-zero net viscous torques. This is the source of vorticity in the Kelvin-Helmholtz instability.

1.4.2 Vortices

A vortex is a flow which revolves around a line axis. The region of the flow where the vorticity is non-zero is called a vortex tube, which is similar to a stream tube, illustrated in Figure 1.7. The strength of the vortex tube is the circulation, calculated along a closed-curve C which lies on the surface of the tube and encircles it just once.

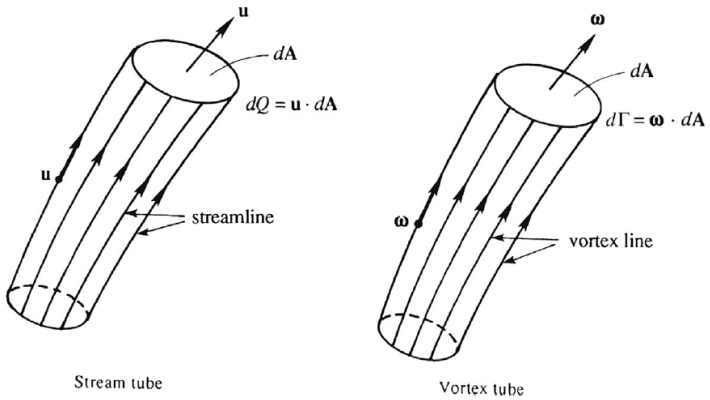

FIGURE 5.1 Analogy between stream tubes and vortex tubes. The lateral sides of stream and vortex tubes are locally tangent to the flow's velocity and vorticity fields, respectively. Stream and vortex tubes with cross-sectional area $d\mathbf{A}$ carry constant volume flux $\mathbf{u}\cdot d\mathbf{A}$ and constant circulation $\boldsymbol{\omega}\cdot d\mathbf{A}$, respectively.

Figure 1.7: Figure 5.1 from Kundu *et al.* [17] illustrates a vortex tube and provides an analogy with a stream tube.

Figure 1.8 shows two different types of steady flows with circular streamlines, which are both vortices. The first type of stationary vortex (Figure 1.8(a)) is rigid-body rotator. Each fluid element (located at radial distance r) spins about its own center at the same rate that it revolves around the origin. The fluid elements (bounded by the regions ABCD and A′B′C′D′) do not deform and their relative positions remain

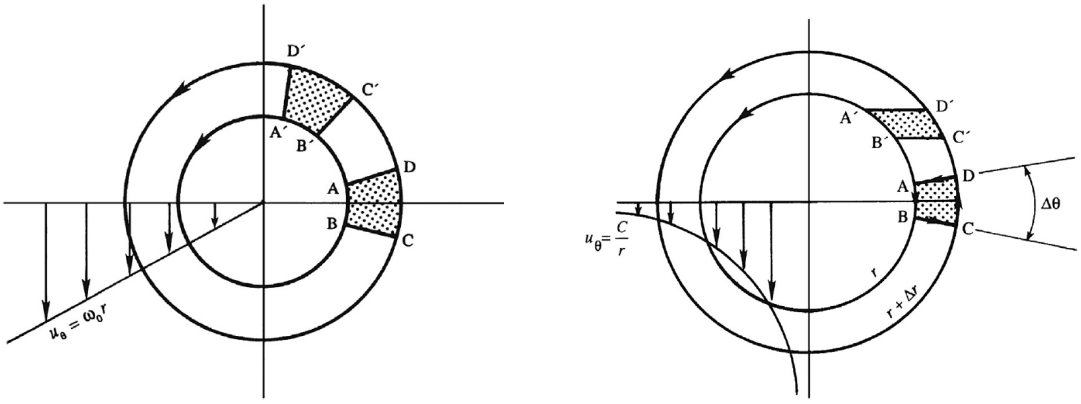

(a) (b)

Figure 1.8: Two types of steady vortex flows with circular streamlines, illustrated in figures from Kundu *et al.* [17] (a) Rigid-body rotator (Figure 3.16); (b) Irrotational line vortex (Figure 3.17)

constant. In cylindrical coordinates, the fluid velocity is $\boldsymbol{u}(r, \theta, z)$. Streamlines lie in the (r, θ) plane and are given by:

$$\begin{aligned} u_r &= 0 \\ u_\theta &= \omega_0 r \end{aligned} \tag{1.17}$$

where ω_0 is a constant equal to the angular velocity of a particle about the origin. The vorticity component in the z-direction is:

$$\omega_z = \frac{1}{r}\frac{\partial}{\partial r}(r u_\theta) - \frac{1}{r}\frac{\partial u_r}{\partial \theta} \tag{1.18}$$

Substitution of Equation 1.17 into Equation 1.18 yields $\omega_z = 2\omega_0 =$ constant. The circulation of the rigid-body rotator increases in proportion to the surface area bounded by the curve:

$$\Gamma = \oint_C \boldsymbol{u} \cdot \, d\boldsymbol{s} = \int_0^{2\pi} u_\theta r d\theta = 2\pi r u_\theta = 2\pi r^2 \omega_0 \tag{1.19}$$

Within the Rayleigh-Taylor literature, sometimes ω_0 is also called "the vorticity" in the context of theoretical models based on a rigid-body rotator description, such as Equation 4.1.

The second type of flow (Figure 1.8(b)) is an irrotational vortex. The streamlines are also circular, but the θ-component of the fluid velocity is inversely proportional to the radial distance:

$$\begin{aligned} u_r &= 0 \\ u_\theta &= \frac{B}{r}, \text{ where } B \text{ is a constant} \end{aligned} \tag{1.20}$$

Velocity shear causes deformation of the fluid elements, but the fluid elements do not spin. Evaluating Equation 1.18, one finds that the flow is irrotational ($\omega_z = 0$) everywhere except at the origin ($r = 0$), where the vorticity is infinite. The circulation is non-zero, finite, and independent of radius:

$$\Gamma = \int_0^{2\pi} u_\theta r d\theta = 2\pi r u_\theta = 2\pi B \tag{1.21}$$

Examples of vortices encountered in nature include tornadoes, whirlpools, and the flow structure created in the air by passage of an airplane wing, shown in Figure 1.6. Real-world vortices do not fit the description of either type of ideal mathematical vortex discussed above. Near the center of rotation, the flow resembles a rigid-body rotator, but at sufficient radial distance, the flow is nearly irrotational. Two common idealizations of the this behavior are the Rankine vortex (Equation 1.22) and the Gaussian vortex (Equation 1.23), where the core-size parameter r_0 specifies the radius of the vortex tube, which is the distance at which the behavior transitions from rigid-rotator to irrotational vortex.

Rankine vortex:

$$\omega_z(r) = \begin{cases} \Gamma/(\pi r_0^2) & \text{for } r \leq r_0 \\ 0 & \text{for } r > r_0 \end{cases}$$

$$u_\theta(r) = \begin{cases} \Gamma r/(2\pi r_0^2) & \text{for } r \leq r_0 \\ \Gamma/(2\pi r) & \text{for } r > r_0 \end{cases} \tag{1.22}$$

Gaussian vortex:

$$\omega_z(r) = \frac{\Gamma}{\pi r_0^2} \exp(^{-r^2}/_{r_0^2})$$

$$u_\theta(r) = \frac{\Gamma}{2\pi r} \left(1 - \exp(^{-r^2}/_{r_0^2})\right) \tag{1.23}$$

The axis of rotation need not be a straight line; it can also be a curve. Moreover, this curve can move and change shape, as is the case with tornadoes. Helmholtz's theorem applies to flows in an inertial reference frame where all body forces are conservative, there are no viscous forces along C, and the fluid is barotropic. Helmholtz's theorem states that [17]:

1. Vortex lines move with the fluid.
2. The strength of a vortex tube is constant along its length.
3. A vortex tube cannot end within the fluid. It must either end at a boundary or form a closed loop within the fluid.
4. The strength of a vortex tube remains constant in time.

An important consequence of Helmholtz's theorem is that a moving vortex carries with it the fluid contained inside the vortex tube. Therefore, vortices can transport

mass, momentum, and energy over considerable distances (much larger than their size).

Vortices located close to each other interact through their mutually induced velocities, generating complex flow patterns. An example of this is the von Kármán vortex street, shown in Figure 1.9. This atmospheric phenomenon can occur when low-altitude air flow deflects around an obstacle (in this case, the island of Guadalupe in the Pacific Ocean), forming a double-row of alternating vortices in the wake. Hydrodynamic instabilities generate smaller-scale vortices, which interact and lead to turbulence.

Figure 1.9: A type of turbulent atmospheric flow pattern known as the von Kármán vortex street. The alternating double row of vortices forms in the wake of an obstacle, in this case, the island of Guadalupe in the Pacific Ocean [18].

1.4.3 Eddies and Turbulence

Many people use the terms "vortex" and "eddy" synonymously. In my view, a semantic distinction exists. A vortex is an actual physical structure, within which the velocity field can be determined (at least in principle) at all length scales, from the outer size of the vortex tube, down to the molecular scale where viscous dissipation

occurs. An eddy is an approximation of a vortex, which models the macroscopic motion and interaction of the structure with the surrounding flow. The velocity field of an eddy is not resolved at the molecular scale.

The eddy description arises primarily in the context of turbulence, where the flow exhibits random fluctuations in the field observables (velocity, pressure, density, temperature, etc.) and strong nonlinearity in the equations of motion. The instantaneous Navier-Stokes (NS) Equations (1.1), plus an equation of state, are a complex system of nonlinear partial differential equations, which are impossible to solve analytically and extremely challenging to compute numerically. The Reynolds-averaged Navier-Stokes (RANS) Equations are a time-averaged version of the equations of motion, in which each flow-field quantity is decomposed into its mean value and a term representing the fluctuations about the mean:

$$\widetilde{u}_i \equiv U_i + u_i', \qquad \widetilde{p} \equiv P + p', \qquad \widetilde{\rho} \equiv \rho + \rho', \qquad \widetilde{T} \equiv T + T' \tag{1.24a}$$

$$\overline{\widetilde{u}_i} = U_i, \qquad \overline{\widetilde{p}} = P, \qquad \overline{\widetilde{\rho}} = \rho, \qquad \overline{\widetilde{T}} = T \tag{1.24b}$$

$$\overline{u_i'} = 0, \qquad \overline{p'} = 0, \qquad \overline{\rho'} = 0, \qquad \overline{T'} = 0 \tag{1.24c}$$

Here, the tilde symbol ($\widetilde{}$) denotes the complete quantities, the prime symbol ($'$) denotes the fluctuating terms, and the over-line denotes the time-averaged quantities. Substitution of Equations 1.24 into the instantaneous NS Equations (1.1) yields the RANS equations. As an example, compare the momentum equations (NS versus RANS) for turbulent flow of an incompressible fluid with an EOS such that the density fluctuations depend only on temperature fluctuations, and the only external body

force is gravity (oriented along the x_3 direction) [17]:

NS: (1.25)

$$\rho\big(\frac{\partial\widetilde{\boldsymbol{u}}}{\partial t}+\widetilde{\boldsymbol{u}}\cdot\nabla\widetilde{\boldsymbol{u}}\big) \quad + \quad \nabla\widetilde{p} \quad - \quad \widetilde{\rho}\boldsymbol{g} \quad - \quad \nabla\cdot\underline{\boldsymbol{\sigma}} \quad = \quad 0$$

RANS: (1.26)

$$\rho\big(\frac{\partial U_i}{\partial t}+U_j\frac{\partial U_i}{\partial x_j}\big) \quad + \quad \frac{\partial P}{\partial x_j}\delta_{ij} \quad - \quad \rho g_3\, f(\rho,T)\delta_{i3} \quad - \quad \frac{\partial \sigma_{ij}}{\partial x_j} \quad + \quad \rho\overline{u_i'u_j'} \quad = \quad 0$$

where $\sigma_{ij}=\mu\big(\frac{\partial U_i}{\partial x_j}+\frac{\partial U_j}{\partial x_i}\big)$ is the mean viscous stress tensor and $f(\rho,T)$ is an explicit function provided by the EOS, which depends only on mean-flow quantities. The final term on the left-hand-side of the RANS momentum equation (1.26) is the cross-correlation between velocity fluctuations:

$$\overline{u_i'u_j'}=\overline{u_i'(\boldsymbol{x}_1,t_1)u_j'(\boldsymbol{x}_1,t_1)}\equiv\lim_{N\to\infty}\frac{1}{N}\sum_{n=1}^{N}u_i'(\boldsymbol{x}_1,t_1:n)\,u_j'(\boldsymbol{x}_1,t_1:n)$$

where u_i', u_j' are measured at the same position $\boldsymbol{x}_1$ and same moment in time t_1 for each realization n, and the ensemble-average is calculated over a large number of randomly-seeded realizations of the turbulent flow field.

The term $\rho\overline{u_i'u_j'}$ is known as the Reynolds stress tensor, for which there is no counterpart in the instantaneous NS momentum equation. The Reynolds stress tensor describes the average rate of momentum transfer in the mean flow due to turbulent velocity fluctuations. In the RANS energy equation (not shown here), a new term arises which represents the turbulent heat flux: $\rho C_p\overline{u_j'T'}$. The full derivation of these equations is provided in [17]. The main point of this example is to show that in each of the equations of motion, we have introduced an additional turbulent quantity, which is not specified in terms of the mean-flow quantities. Inherently, the RANS equations are not closed and cannot be solved without some sort of model for turbulence.

Vortices transport mass, momentum and energy. The simplest model of turbulence

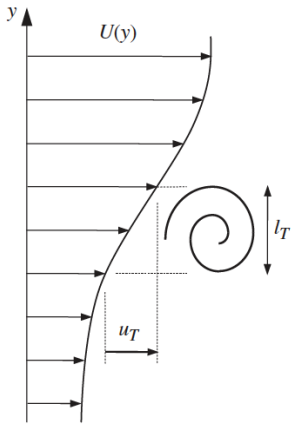

Figure 1.10: Conceptual illustration of the mixing-length model for turbulence (Figure 12.26 from Kundu *et al.* [17]). In this picture, $U(y)$ is the mean flow velocity and an eddy is characterized by a length scale l_T and turbulent velocity u_T.

is based on the eddy mixing-length concept, first introduced by Taylor in 1915 [19]. Illustrated in Figure 1.10, an eddy of size l_T experiences a local shear rate of dU/dy and produces a turbulent velocity fluctuation $u_T \sim l_T(dU/dy)$. The time scale of the velocity fluctuation is the "eddy turnover time," $t_T \sim l_T/u_T$. In this picture, the correspondence between the Reynolds stress tensor and the viscous stress tensor is clear:

$$-\overline{u'_x u'_y} = \nu_T \frac{dU}{dy} \sim l_T u_T \frac{dU}{dy} \sim l_T \Big(l_T \frac{dU}{dy} \Big) \frac{dU}{dy} = l_T^2 \Big(\frac{dU}{dy} \Big)^2 \tag{1.27}$$

where ν_T is the eddy viscosity (or turbulent viscosity).

In analogy to the kinematic transport theory of molecular motion, Prandtl [20] and von Kármán [21] developed an approach to turbulence modeling in which eddies possess the properties of turbulent viscosity ν_T, turbulent thermal conductivity η_{QT}, and turbulent mass diffusivity η_m. These properties are defined by constitutive relations similar to Newton's law of viscosity, Fourier's law of heat transport via a temperature gradient, and Fick's law of mass diffusion. These relations express the turbulent quantities in terms of the mean-flow quantities and provide closure to the RANS equations.

Large Eddy Simulations (LES) solve the RANS equations. Smagorinsky proposed the first formula for eddy viscosity in terms of numerical simulation quantities [22]:

$$\nu_T = \Delta_x \Delta_y \sqrt{\left(\frac{\partial u_x}{\partial x}\right)^2 + \left(\frac{\partial u_y}{\partial y}\right)^2 + \frac{1}{2}\left(\frac{\partial u_x}{\partial y} + \frac{\partial u_y}{\partial x}\right)^2} \tag{1.28}$$

Here, Δ_x, Δ_y are the local grid sizes and the other quantities in the Equation 1.28 are the local derivatives of the velocity field. Different LES codes may use different models of turbulence or different numerical methods. However, all LES codes implement some sort of non-physical model for turbulence. These simulations predict the approximate behavior of turbulent flows, but they do not calculate the exact solution to the NS equations. If the models do not accurately capture all the relevant physical processes in a flow, the simulations may yield misleading results.

1.5 Hydrodynamic Instabilities

Many HED systems evolve from initially stratified fluid-like layers. If the interface between two layers is energetically unstable, the fluids interpenetrate and mix. Several different types of hydrodynamic instabilities exist (where different physical interactions drive the mixing). The focus of this thesis is the Rayleigh-Taylor instability (RTI). In this section, I will introduce RTI and examples of where it occurs in HED systems. Chapter II provides a detailed mathematical description of RTI. In blast-wave-driven experiments of RTI, two other hydrodynamic instabilities occur: Richtmyer-Meshkov instability (RMI) and Kelvin-Helmholtz instability (KHI). A detailed explanation of RMI and KHI is beyond the scope of this work. Here, I provide only a brief description of these other instabilities and their linear-stage growth rates, so that they can be understood in the context of subsequent chapters.

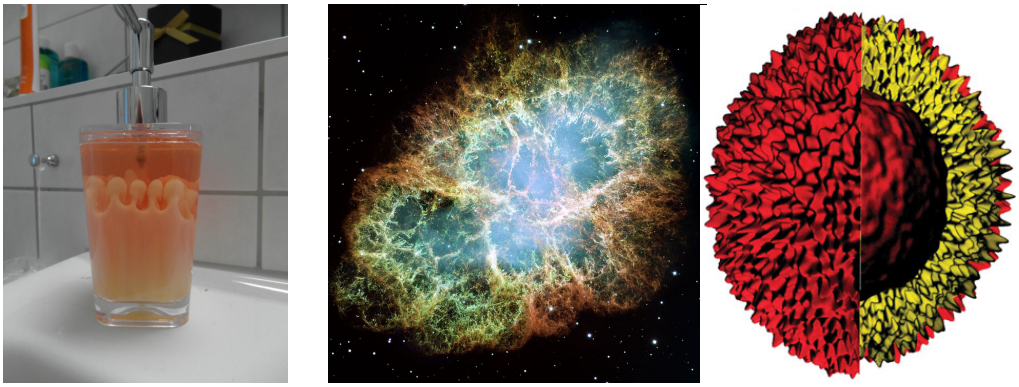

Figure 1.11: Examples of RTI in every-day life and in HED systems. Left: A liquid-soap dispenser filled with two layers of different densities demonstrates the formation of quintessential RTI "bubbles and spikes" [23]. Center: Crab nebula supernova remnant shows features characteristic of RTI [24]. Right: Simulation of ICF capsule implosion, where perturbations on the outer surface seed RTI growth [25].

1.5.1 The Rayleigh-Taylor Instability

Most people are familiar with the Rayleigh-Taylor instability, although they might not know it by that name. This phenomenon occurs when a heavier fluid is suspended on top of a lighter fluid, and the two layers begin to interact under the force of gravity. Consider a container filled half-way up with water, then topped off with oil. Since oil is lighter than water, the two fluids will remain in this stable state. On the other hand, if the container is filled in opposite order, so that the water is on top of the oil, the configuration is unstable. A tiny disturbance will seed a run-away process: oil bubbles begin to form and rise upward, as equal volumes of water fall downward. The two fluids continue to interpenetrate and mix, lowering the potential energy of the system until a steady state is achieved. This phenomenon was first studied by Lord Rayleigh (J.W. Strutt) in 1883 [26]. In more general terms, this hydrodynamic instability occurs wherever two fluids of different densities are separated at an interface and there exists a pressure gradient in opposition to the density gradient. The force applying the pressure need not be the Earth's gravity. In 1950, G.I. Taylor recognized that the same behavior occurs at an accelerating interface [27]. In honor of their

contributions, this hydrodynamic instability is now called Rayleigh-Taylor.

Hydrodynamic instabilities, including RTI, play a major role in many HED systems of interest. Extensive research efforts (laboratory experiments and numerical simulations) have investigated how mixing due to RTI may affect the evolution of core-collapse supernovae and ICF capsule explosions. In a star, atomic elements are stratified in concentric layers, increasing in density towards the core. When the star becomes sufficiently massive, it collapses under its own gravity and explodes, launching a blast wave that expels the stellar matter out into space. The interfaces between interior layers, as well as the outer-most interface between the stellar ejecta and the less-dense circumstellar matter, are Rayleigh-Taylor unstable. Far away on Earth, we observe light from the supernova explosion. Each atomic element emits EM radiation at characteristic frequencies. The arrival times and Doppler broadening of these EM signatures inform our understanding of the physical processes which occurred during the supernova explosion and test explosion models (relevant to national security applications, in addition to astrophysics).

In 1987, observations of a core-collapse supernova (SN 1987A) indicated that denser material had penetrated farther into the outer layers and traveled at a higher velocity than predicted by spherically-symmetric explosion models [28]. This suggests that significant material mixing due to hydrodynamic instabilities may have occurred, creating complex three-dimensional (3D) structures which one-dimensional (1D) and two-dimensional (2D) models do not accurately describe.

In ICF, increased material mixing due to RTI can thwart ignition at two stages of the implosion process. First, target imperfections on the outer surface of the shell and non-uniform irradiation create perturbations which grow due to RTI during the ablative acceleration stage. These perturbations can then "feed through" to the ablator-fuel interface, which becomes RT-unstable when this interface decelerates during the stagnation phase [29]. Additional imperfections may also exist in the target

interior and provide the seed for RTI growth during this second stage. Thus we seek to understand RTI, how to predict the extent of material mixing, and how to suppress it by engineering design.

1.5.2 The Richtmyer-Meshkov Instability

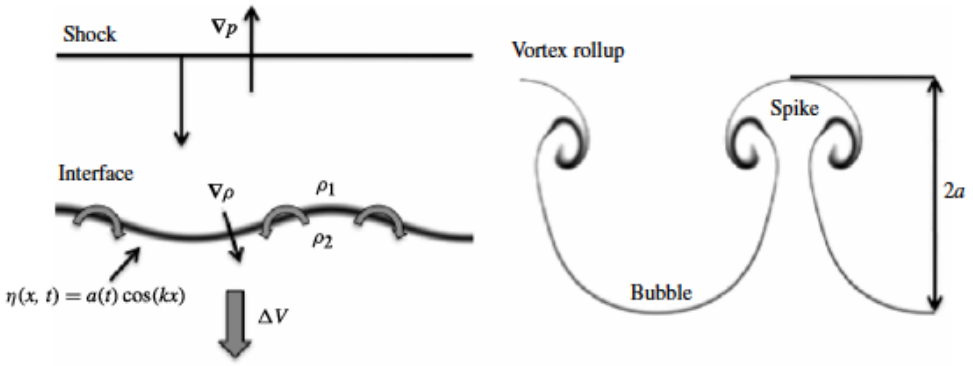

FIGURE 1. Explanation of the deposition of baroclinic vorticity on the interface. (*a*) The shock wave travels downward toward the interface and applies a pressure gradient across the density gradient which generates baroclinic vorticity on the interface. (*b*) This baroclinic vorticity rolls up into spikes of heavy fluid separating bubbles of light fluid as the interface travels down the shock tube with the mean post-shock flow.

Figure 1.12: Conceptual illustration of the Richtmyer-Meshkov instability. Figure from Morgan *et al.* [30]

The Richtmyer-Meshkov instability arises from the deposition of baroclinic vorticity [30]:

$$\rho \frac{D}{Dt}\left(\frac{\boldsymbol{\omega}}{\rho}\right) = \frac{1}{\rho^2}\nabla\rho \times \nabla p \tag{1.29}$$

This situation occurs when a perturbed interface between two fluids of different densities is impulsively accelerated. In HED systems, such an impulsive acceleration is caused by a shock wave. From this perspective, RMI closely resembles the Rayleigh-Taylor instability (which occurs under continuous acceleration). However, RTI only occurs when the lighter fluid is pushing the heavier fluid ($\nabla p \cdot \nabla \rho < 0$). In the case of RMI, the perturbation amplitude $h(t)$ grows for both light-to-heavy ($\nabla p \cdot \nabla \rho < 0$) and heavy-to-light ($\nabla p \cdot \nabla \rho > 0$) cases.

For incompressible fluids, the linear RMI growth rate can be derived in a similar fashion to RTI (Chapter II, Section 2.1.1) by inserting an $g = (du)\,\delta(t)$ into Equation 2.15. Here, (du) is the velocity induced at the interface and $\delta(t)$ is the Dirac delta function. The result of this is:

$$\frac{\partial^2 h(t)}{\partial t^2} = Ak\,(du)\,\delta(t)\,a \tag{1.30a}$$

$$\frac{\partial h(t)}{\partial t} = u_{_{RM}} = Ak\,(du)\,a \tag{1.30b}$$

$$h(t) = u_{_{RM}} t + a \tag{1.30c}$$

where a and k are the initial amplitude and wavenumber of seed perturbation. A is the Atwood number, as defined in Equation 2.12. This linear growth rate applies in the small-amplitude regime, where $(hk \ll 1)$.

When the impulsive acceleration is caused by a shock wave crossing the interface, one must consider the pre- and post-shock fluid states. I will use the asterisk symbol (*) to denote post-shock quantities. In 1960, R.D. Richtmyer first studied the interaction of a shock wave crossing a light-to-heavy interface $(\nabla p \cdot \nabla \rho < 0)$ [31] and modified Equation 1.30b to:

$$u_{_{RM}} = A^*\,k\,(du)\,a^* \tag{1.31}$$

In 1969, E.E. Meshkov performed experiments with the shock wave traveling from heavy-to-light fluid regions $(\nabla p \cdot \nabla \rho > 0)$ [32]. In this case, the initial perturbation amplitude a is compressed and inverted (phase reversal) to post-shock amplitude a^*, and then increases. Meyer and Blewett performed 2D simulations of Meshkov's experiments and found better agreement with their simulation data and the following formula for the instability growth (as opposed to the formula of Richtmyer, Equation

1.31) [33]:

$$u_{_{RM}} = A^* \, k \, (du) \big(\frac{a^* + a}{2} \big) \tag{1.32}$$

The Meyer-Blewett formula is most commonly used for the linear growth rate.

1.5.3 The Kelvin-Helmholtz Instability

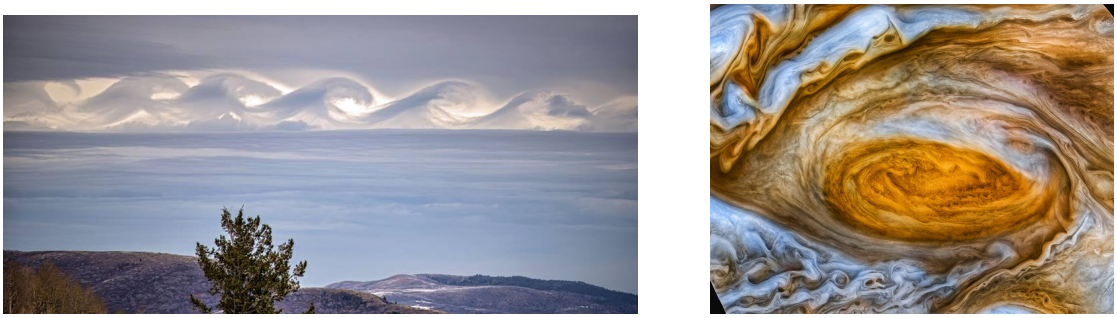

(a) (b)

Figure 1.13: The Kelvin Helmholtz instability can create visually-stunning spiral patterns in stratified planetary atmospheres. (a) In the Earth's atmosphere, optically opaque clouds in the denser, slower-moving layer make the interface structure visible in this photo [34]; (b) In Jupiter's atmosphere, complex vortical flows, including the giant storm known as "the Great Red Spot," result from KHI. This image is from NASA's Voyager 1 space probe [35].

This hydrodynamic instability is named after Lord Kelvin (William Thomson) [36] and Hermann von Helmholtz [37]. Velocity shear in a stratified fluid (or a velocity difference across the interface between two fluids) generates vorticity, causing the interface to roll up, forming a mixing layer. KHI can create visually-stunning spiral patterns in stratified planetary atmospheres, including the Earth's and Jupiter's, shown in Figure 1.13.

Figure 1.14 illustrates the case where KHI is seeded by a single-mode sinusoidal perturbation with wavelength $\lambda_{_{KH}}$ at the interface between two fluids moving at different velocities, u_1 and u_2. For subsonic, incompressible flows, the linear growth rate for KHI at an interface where there is a density jump in addition to a velocity

jump is given by [38]:

$$\gamma_{KH} = \frac{\pi|u_2 - u_1|}{\lambda_{KH}} \frac{\sqrt{\rho_1 \rho_2}}{\rho_1 + \rho_2} = \frac{\pi|u_2 - u_1|}{\lambda_{KH}} \sqrt{1 - A^2} \tag{1.33}$$

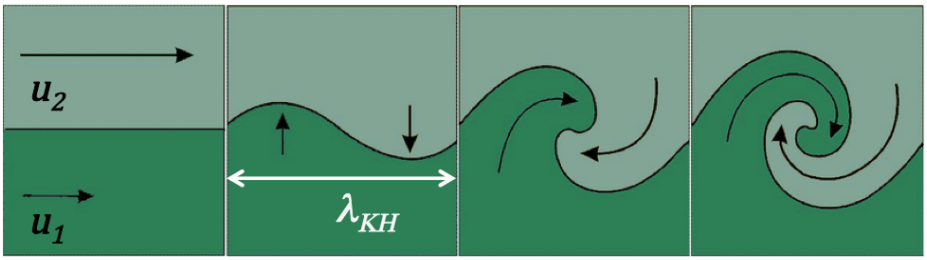

Figure 1.14: Conceptual illustration (modified from figure by [39]) of the linear growth stage of the Kelvin-Helmholtz instability seeded by a single-mode sinusoidal perturbation. Velocity shear generates vorticity, causing the interface to roll up.

In the linear growth stage, individual vortices increase in size. When they become large enough to interact with each other, adjacent vortices couple into vortex-pairs, which then merge and form a larger vortex structure with wavelength $2\lambda_{KH}$. Figure 1.15 illustrates the processes of vortex pairing and merger.

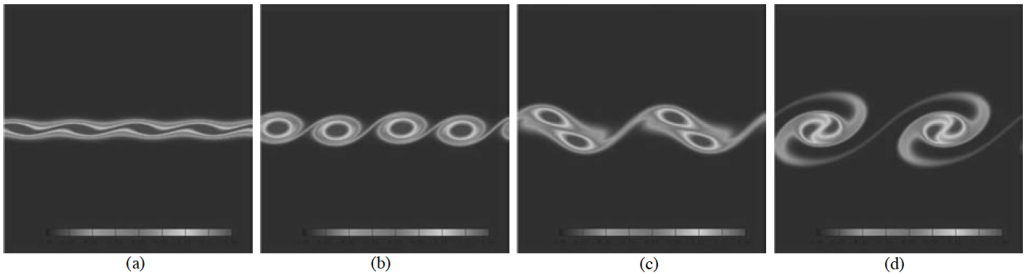

Figure 1.15: Plots of the spanwise vorticity field from 3D simulations by Martinez *et al.* [40] illustrate the temporal evolution of single-mode KHI growth and the processes of vortex pairing and merger. Non-dimensional times: (a) 9.52; (b) 19.03; (c) 28.55; (d) 38.07.

1.6 Summary of Chapters

Chapter II provides an overview of theoretical models of RTI and metrics for quantifying the different growth stages. Chapter III summarizes the results of published simulation studies of single-mode RTI at low-Atwood-number, which specifically motivated this work. Chapter IV reviews prior work in classical fluids and HED experiments. Chapter V describes the experimental implementation of the target and diagnostics. Chapter VI discusses the experimental results, including sources of error and uncertainty, and compares the experimental data with CRASH simulations and buoyancy-drag models. Chapter VII concludes with remarks on the outlook for extending these experiments to the NIF. The appendices provide detailed information on image post-processing methods using Matlab, target metrology, and a log of all shot days and the data obtained.

1.7 Collaborators and Individual Contributions

In 2015, Professor Carolyn Kuranz at the University of Michigan and Dr. Guy Malamud at Nuclear Research Center, Negev, Isael proposed Omega-60 experiments of the late-nonlinear growth stage of single-mode Rayleigh-Taylor instability. The project was funded by Lawrence Livermore National Laboratory (LLNL) under a grant from the U.S. Department of Energy, National Nuclear Security Administration. At LLNL, Dr. Channing Huntington was the principal collaborator. In addition to Carolyn and myself, the team at the University of Michigan included Dr. Timothy Handy, Dr. Rachel Young, Matt Trantham, and Sallee Klein. The experimental campaign at Omega-60 consisted of four shot days over the course of three years: October 6, 2016, April 6, 2017, April 19 2018, and July 18, 2018. Sallee was the target fabrication engineer, whose contributions included mechanical drawings of individual target components and the complete target packages, parts procurement, and manual

assembly of all the targets. Sallee and Carolyn also provided logistical support during all shot days.

Throughout this dissertation, I will reference two different types of radiation-hydrodynamics simulations: Hyades (1D) and CRASH (1D and 2D). Hyades is a Lagrangian code which implements simplistic physics models and requires minimal computational resources [41]. A Hyades simulation takes about an hour to run on my laptop. For the Hyades simulations, I personally configured the input decks, executed the simulations, and wrote Matlab code to parse the output files for the desired variables at the desired times, and then plot and display the data. This enabled me to rapidly assess the impact of various design changes, such as the material composition and thickness of the target components. These simulations provided qualitative insights and rough estimates of physical variables, but not quantitatively accurate predictions for the real physical system. After the preliminary design phase with Hyades, I communicated the detailed target design and laser drive parameters to the computational specialists on our team (Tim, Matt, and Rachel), who performed the CRASH simulations.

CRASH is an Eulerian code which features adaptive mesh refinement, self-consistent equations-of-state and opacities, multi-group diffusive radiation transport, electron physics and flux-limited electron heat conduction, and a laser package with 2D ray-tracing capabilities [8]. A 2D CRASH simulation with moderate spatial resolution takes approximately one week to run on a parallel computing cluster with 60 cores and generates over 50 GB of binary data output files, which must then be converted to a user-friendly format. During a post-doctoral appointment spanning 2015-2017, Tim created the original input deck for the CRASH simulations, including specification of the physics models and numerical methods implemented in the simulations. Following Tim's departure, Guy completed the analysis of Tim's work and published these results [42]. This preliminary design is discussed in Chapter V. After completion

of the experiments, Rachel and Matt performed simulations of the final design and provided the simulation data for my analysis, presented in Chapter VI.

My role in the project was to lead the experiments and interpret the results. This work included:

- Design of the main target and backlighter targets, in consideration of the theoretical physics and experimental goals, facility limitations and requirements, target fabrication and metrology capabilities, and project schedule and budget
- Design of the experimental configuration at Omega-60, including specification of laser beam parameters, target positioning and alignment, and diagnostic configuration
- Development of metrology procedures for pre-shot characterization of the targets, performing the metrology, and analyzing the results
- Serving as Principal Investigator for the experiments, which included direct communication with the staff at Omega-60, planning and supervising execution of the shot days, and real-time trouble-shooting of issues that arose during shot days
- Processing the raw image data. This involved writing Matlab code to read the data files and apply image-processing algorithms for noise filtering and contrast enhancement, including determination of the actual spatial resolution
- Analysis of the experimental data and comparison with theory and simulations
- Interpretation of the experimental outcome and relevance to the broader scientific community and recommendations for future work

CHAPTER II

Mathematical Description of the Rayleigh-Taylor Instability

This chapter provides the mathematical description of RTI, introduces metrics for quantifying the different growth stages, and reviews analytical models for single-mode, multi-mode, and turbulent cases.

2.1 Single-Mode RTI

Analytical models of single-mode RTI predict the growth rate of the mixed-fluid layer in two stages of its evolution. The first stage is described by linear stability theory; the second ("nonlinear") stage is described by potential-flow models. Figure 2.1 illustrates how the shape of the interface changes from the linear stage to the nonlinear stage.

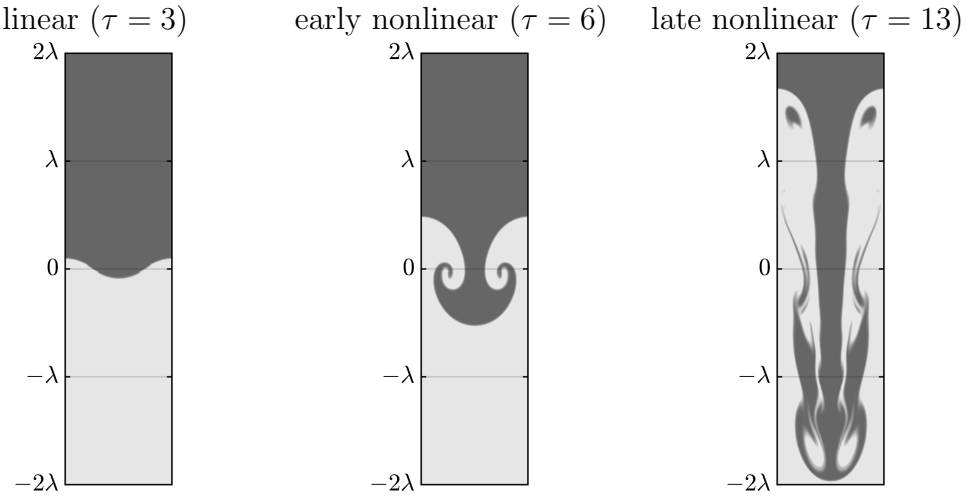

Figure 2.1: Density plots of the interface show the evolution of the spike (dark gray) and the bubble (light gray) in the linear ($\tau = 3$), early nonlinear ($\tau = 6$), and late-nonlinear ($\tau = 13$) growth stages. These plots are from a 2D CRASH simulation by Tim Handy of single-mode RTI with constant acceleration and classical, incompressible, immiscible fluids at low-Atwood-number ($A = 0.15$). The horizontal domain of the simulation spans one wavelength with periodic boundary conditions.

2.1.1 Early Growth Stage: Linear Stability Theory

The initial problem setup is illustrated in Figure 2.2. The Rayleigh-Taylor unstable system consists of two semi-infinite, homogeneous fluids of different densities, meeting at a contact surface (the interface). The heavier fluid is on top (ρ_1, $z > 0$), the lighter fluid is on bottom (ρ_2, $z < 0$), and the acceleration force g is downward (negative z-direction). This creates a pressure gradient in opposition to the density gradient across the interface: $\nabla p \cdot \nabla \rho < 0$.

For simplicity, I will derive the linear Rayleigh-Taylor growth rate for a 2D system, assuming the fluids to be inviscid, incompressible, and irrotational. Mathematically, the system is described in the reference frame where the interface is at rest. On either side of the interface, each fluid obeys Laplace's Equation (2.1a), Bernoulli's Equation (2.1b), and a kinematic boundary condition stating that the interface moves with the

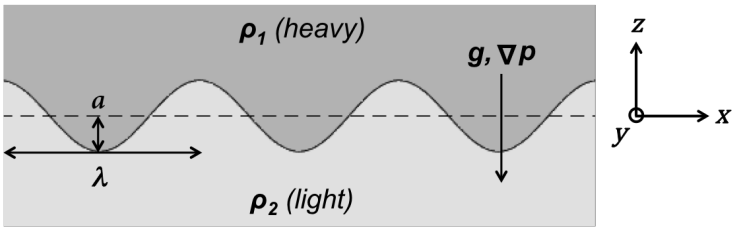

Figure 2.2: Illustration of initial problem set-up for single-mode RTI. The denser fluid is on top (dark gray), the lighter fluid is on bottom (light gray), and acceleration g is downward. For readability, the initial perturbation amplitude a is greatly exaggerated with respect to the wavelength λ. In actuality, $a/\lambda \ll 1$.

fluids on either side (2.1c):

$$\nabla^2 \phi = 0 \tag{2.1a}$$

$$\frac{\partial \phi}{\partial t} + \frac{1}{2}u^2 + gz + \frac{p}{\rho} = \text{const.} \tag{2.1b}$$

$$\frac{\partial \phi}{\partial z} - \frac{\partial \phi}{\partial x}\frac{\partial \zeta(x,t)}{\partial x} = \frac{\partial \zeta(x,t)}{\partial t} \tag{2.1c}$$

where ϕ is the velocity potential ($u = \nabla\phi$). At time $t = 0$, there exists a seed perturbation at the interface of the form $\zeta(x, t = 0) = a\cos(kx)$, where the initial amplitude is very small with respect to the wavelength ($a/\lambda \ll 1$). We seek to predict the temporal evolution of this perturbation, i.e., to solve for the amplitude $h(t)$, where:

$$\zeta(x,t) = h(t)\cos(kx) \tag{2.2}$$

Equations 2.1 can be solved using a perturbation-theory expansion, where each physical quantity $q = q_0 + \epsilon^1 q + \epsilon^2 q^2 + ...$ (Here ϵ represents the expansion coefficient, not the specific internal energy.) In the linear stage, we keep only first-order terms

and Equation 2.1b simplifies to:

$$\begin{aligned} \frac{\partial \phi_1}{\partial t} + gz + \frac{p_1}{\rho_1} &= c_1 \\ \frac{\partial \phi_2}{\partial t} + gz + \frac{p_2}{\rho_2} &= c_2, \end{aligned} \tag{2.3}$$

where $c_1,\ c_2$ are arbitrary constants. Multiplying Equation 2.3 by the fluid density gives:

$$\begin{aligned} \rho_1\ (\frac{\partial \phi_1}{\partial t} + gz) &= \rho_1 c_1 - p_1 \\ \rho_2\ (\frac{\partial \phi_2}{\partial t} + gz) &= \rho_2 c_2 - p_2 \end{aligned} \tag{2.4}$$

Constants are chosen so that $(\rho_1 c_1 - p_1) = (\rho_2 c_2 - p_2)$ and therefore:

$$\rho_1\ (\frac{\partial \phi_1}{\partial t} + gz) = \rho_2\ (\frac{\partial \phi_2}{\partial t} + gz) \tag{2.5}$$

The velocity potentials that satisfy the Bernoulli Equation (2.3) are:

$$\begin{aligned} \phi_1(x, z, t) &= B_1(t)\, e^{kz} \cos(kx),\ \ z \geq 0 \\ \phi_2(x, z, t) &= B_2(t)\, e^{-kz} \cos(kx),\ \ z \leq 0 \end{aligned} \tag{2.6}$$

where $B_1(t)$ and $B_2(t)$ are some yet-to-be-determined coefficients. Differentiating these velocity potentials with respect to time, evaluating at $z = 0$, and substituting the results into Equation 2.5 yields:

$$\rho_1\ \Big(\frac{\partial B_1}{\partial t} + g\ h(t)\Big) \cos(kx) = \rho_2\ \Big(\frac{\partial B_2}{\partial t} + g\ h(t)\Big) \cos(kx) \tag{2.7}$$

From the kinematic boundary condition (2.1c), the interface velocity must equal the flow velocity in the vertical direction:

$$\frac{\partial \zeta}{\partial t} = u_z = \frac{\partial \phi}{\partial z} \tag{2.8}$$

On the right-hand-side of Equation 2.8, substitution of the velocity potentials (2.6), differentiated with respect to z and evaluated at $z = 0$, gives:

$$\begin{aligned} \frac{\partial \phi_1}{\partial z} &= k\ B_1(t) \cos(kx) \\ \frac{\partial \phi_2}{\partial z} &= -k\ B_2(t) \cos(kx) \end{aligned} \tag{2.9}$$

Therefore, the coefficients simplify to $B(t) = B_1(t) = -B_2(t)$ and Equation 2.9 becomes:

$$\frac{\partial \phi}{\partial z} = k\ B(t) \cos(kx) \tag{2.10}$$

Substituting Equation 2.10 into Equation 2.5, evaluated at $z = 0$, provides:

$$\frac{\partial B}{\partial t} = Ag\, h(t) \tag{2.11}$$

where the Atwood number, A, quantifies the density contrast of the two fluids:

$$A \equiv \frac{\rho_1 - \rho_2}{\rho_1 + \rho_2} \tag{2.12}$$

Low-Atwood-number ($A \to 0$) corresponds to the interface between two fluids with nearly equal densities ($\rho_1 \simeq \rho_2$), whereas the high-Atwood-number limit ($A = 1$) corresponds to the interface between a finite-density fluid ($\rho_1 > 0$) and vacuum ($\rho_2 = 0$).

Returning to Equation 2.8, the left-hand-side is solved by taking the time derivative of the interface Equation (2.2):

$$\frac{\partial \zeta}{\partial t} = \frac{\partial h(t)}{\partial t} \cos(kx). \tag{2.13}$$

Combining Equations 2.8, 2.10, and 2.13 provides:

$$B(t) = \frac{1}{k}\frac{\partial h}{\partial t} \tag{2.14}$$

Finally, by differentiating Equation 2.14 with respect to time and equating the result with Equation 2.11, one obtains:

$$\frac{\partial^2 h(t)}{\partial t^2} = Akg\, h(t) \tag{2.15}$$

The solution to this second-order differential equation is:

$$\begin{aligned} &h(t) = a\exp(\gamma_{_{RT}} t), \text{ where} \\ &\gamma_{\text{RT}} = \sqrt{Akg} \end{aligned} \tag{2.16}$$

The math follows similarly in three dimensions. The main take-away is that, in the linear stage where $h/\lambda \ll 1$, the perturbation grows exponentially, with symmetric growth in the heavy- and light-fluid regions:

$$\begin{aligned} &\text{2D: } \zeta(x,t) = h(t)\cos(kx) \\ &\text{3D: } \zeta(x,y,t) = h(t)\cos(kx)\cos(ky) \\ &h(t) = a\exp(\gamma_{\text{RT}} t) \end{aligned}$$

Dimensionless length and time scales quantify the different stages of RTI growth (shown in Figure 2.1). In the spatial domain, the logical choice is the ratio of vertical to horizontal length scales, h/λ. In the temporal domain, we use the number of e-foldings for linear RTI growth, generalized for time-varying densities and acceleration:

$$\tau = \int_0^t \gamma_{\text{RT}}\, dt' = \int_0^t \sqrt{\frac{2\pi}{\lambda} A(t')g(t')}\, dt'. \tag{2.17}$$

2.1.2 Nonlinear Growth Stage: Potential-Flow Theory and Buoyancy-Drag Models

The nonlinear growth stage begins when $h/\lambda \simeq 0.1$. Expanding the 2D perturbation theory solution to second and third order yields [43]:

$$\begin{aligned}\zeta(x,t) = {} & h_1(t)\cos(kx) \\ & - \frac{1}{2}Ak\, h_1(t)^2\cos(2kx) \\ & + A^2k^2\, h_1(t)^3\Big[\frac{1}{8}(4A^2-1)\cos(3kx) - \frac{1}{16}(1+3A^2)\cos(kx)\Big] \\ \text{where } & h_1(t) = a\exp(\gamma_{\text{RT}}t)\end{aligned} \tag{2.18}$$

Higher-order harmonic modes emerge and break the symmetry across the interface. The regions of light fluid rising upward are centered about peaks located at $kx = (2m)\pi$, and the regions of heavy fluid falling downward have peaks at $kx = (2m+1)\pi$, where m is an integer. In the light-fluid regions, the higher-order harmonic modes are out-of-phase with the fundamental. As these higher-order terms increase in magnitude, the light-fluid peaks broaden and decelerate, forming shapes described as "bubbles." In the heavy-fluid regions, the higher-order terms remain in-phase with the fundamental, thereby narrowing and accelerating the growth of features called "spikes." KHI arises due to the velocity shear between bubbles and spikes, which causes the interface to roll up and form the characteristic "mushroom cap" shapes. Initially, a coherent array of vortices forms along the interface where it intersects the $z = 0$ plane; the size of the vortices increases with time. (In 3D, this corresponds to an array of vortex rings.) At this point, analytic solutions for the shape of the interface and its detailed structure become intractable. Without solving for the internal dynamics of the mixed-fluid layer, potential-flow-theory models predict the height of the bubble (or spike) at its vertex, by assuming that the flow there is irrotational and can be described by a velocity potential: $u_B = \nabla\phi$, where u_B is the velocity at the tip of the bubble and ϕ is a scalar

function. As long as the vortices remain localized near $z = 0$, the flow near the tip of the bubble is unaffected. Various potential-flow-theory models exist, which assume different forms of the velocity potential. For classical, incompressible fluids, these models predict that bubbles and spikes asymptotically approach terminal velocities (with slightly different values, depending on the choice of velocity potential).

In 1955, Layzer developed the first potential-flow-theory model for nonlinear 2D bubble growth for the $A = 1$, constant acceleration, incompressible fluid case [44]. This work was later extended to arbitrary Atwood number ($0 < A \leq 1$) and 3D geometries by Goncharov in 2002 [45], and time-varying acceleration by Srebro *et al.* in 2003 [46]. Summarizing these results:

Bubble:

$$\Big(\big[C_1 E_B(t) + 1\big]\rho_2 + \big[C_1 + E_B(t)\big]\rho_1\Big)\dot{u}_B = \big[1 - E_B(t)\big]\big(\rho_1 - \rho_2\big)g(t) - C_2 k \rho_1 u_B^2$$

Spike:

$$\Big(\big[C_1 E_S(t) + 1\big]\rho_1 + \big[C_1 + E_S(t)\big]\rho_2\Big)\dot{u}_S = \big[1 - E_S(t)\big]\big(\rho_1 - \rho_2\big)g(t) - C_2 k \rho_2 u_S^2$$

where $E_{B,S}(t) = \exp[-C_3 k\, h_{B,S}(t)]$, $u_{B,S} = \dot{h}_{B,S}$ (for either bubble or spike)

$$\text{and constants } [C_1, C_2, C_3] = \begin{cases} [2, 3, 3] \text{ for 2D} \\ [1, 1, 2] \text{ for 3D} \end{cases} \tag{2.19}$$

The notation $\dot{h}$ denotes the temporal derivative $\partial h/\partial t$. The bubble height, $h_B(t)$, is defined as the distance between the tip of the bubble and the $z = 0$ plane (and similarly for spikes). The total mixed-layer width is $h(t) = h_B(t) + h_S(t)$. In the late-nonlinear stage ($h/\lambda \gg 1,\ E \to 0$), Equation 2.19 can be expressed as a force-balance

equation [47] [48]:

$$\begin{array}{lrcl} & \textit{inertia + added mass} & = & \textit{buoyancy - drag} \\ \text{Bubble:} & (\rho_2 + C_1\rho_1)\,\dot{u}_B & = & (\rho_1 - \rho_2)\,g(t) - C_2 k \rho_1 u_B^2 \\ \text{Spike:} & (\rho_1 + C_1\rho_2)\,\dot{u}_S & = & (\rho_1 - \rho_2)\,g(t) - C_2 k \rho_2 u_S^2 \end{array} \tag{2.20}$$

We expect more rapid growth in a 3D flow. The dimensional dependence reflects the geometrical shape of the bubble, which experiences less drag in 3D.

In traditional fluid mechanics, the Froude number characterizes the relative strength of the inertial and gravity forces: $Fr = {}^{U}/_{\sqrt{gL}}$, where U, L are the velocity and length scale of the flow. Ramaprabhu *et al.* defined an RT Froude number [49]:

$$Fr_{B,S} \equiv \frac{u_{B,S}}{\sqrt{\frac{Ag\lambda}{1+A}}} \tag{2.21}$$

The RT Froude number is commonly used as a non-dimensional velocity, which compares instantaneous velocity at the bubble or spike tip to the steady-state solution predicted by buoyancy-drag models. In the asymptotic limit ($t \to \infty$), buoyancy equals drag, so that the right-hand-side of Equation 2.20 is zero. Therefore, bubbles and spikes approach terminal velocities and constant Froude numbers:

$$\begin{array}{l} \text{Bubble: } u_B = \sqrt{\dfrac{Ag\lambda}{C\pi(1+A)}},\; Fr_B = \sqrt{\dfrac{1}{C\pi}} \\ \text{Spike: } u_S = \sqrt{\dfrac{Ag\lambda}{C\pi(1-A)}},\; Fr_S = \sqrt{\dfrac{1}{C\pi}\dfrac{A+1}{A-1}} \\ \text{where C=[3, 1] for [2D, 3D] flows.} \end{array} \tag{2.22}$$

This buoyancy-drag model converges to the linear and early nonlinear perturbation-theory solution (Equation 2.18). In the late-nonlinear stage, Equations 2.22 predict the correct qualitative trend: for all Atwood number, spikes grow more rapidly

than bubbles, and this asymmetry increases with Atwood number. However, as the density contrast of the two fluids increases, the terminal velocity predicted for spikes fails. In the zero-drag limit ($A = 1$, $\rho_2 = 0$), spikes should exhibit free-fall behavior ($h_S = \frac{1}{2}gt^2$, $u_S = gt$). Numerous other potential-flow models (e.g. Sohn [50], Abarzhi *et al.* [51]) and heuristic/interpolation models (e.g. Mikaelian [52]) have been developed, which work more or less well for particular cases. For a comprehensive review, the reader is referred to Zhou's 2017 publications [53] [54].

2.2 Multi-Mode RTI

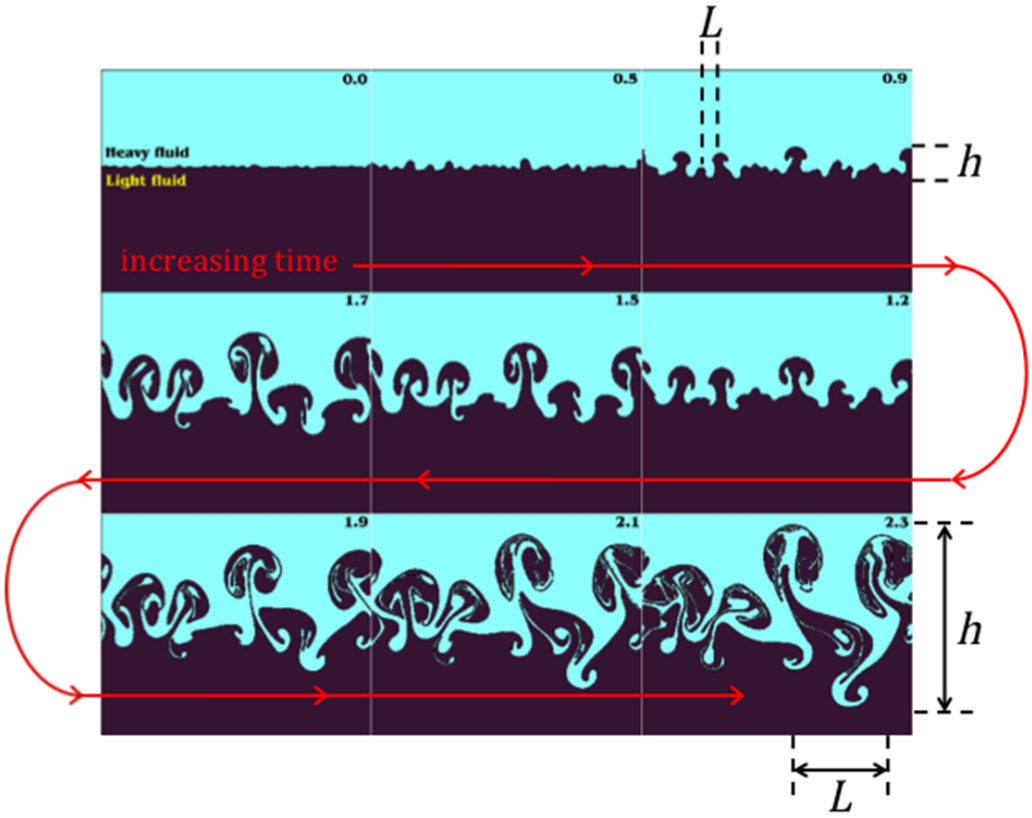

Figure 2.3: 2D simulation of multi-mode RTI, showing self-similar evolution of the mixed-fluid region. The horizontal length scale L grows in proportion to the vertical length scale h. Figure modified from Nourgaliev and Theofanous [55].

Now consider the case where RTI growth is initially seeded with a multi-mode

perturbation spectrum. Early in time, each mode evolves independently, first growing exponentially and then reaching a nonlinear saturation amplitude, after which it grows at a constant velocity [56]. In the linear stage, short-wavelength modes grow fastest (Equation 2.16), but saturate sooner, as compared to longer-wavelength modes. This leads to a peak the velocity spectrum, where mid-wavelength modes have the largest growth factor. However, in the nonlinear growth stage, modes interact with each other. Statistical models of bubble competition and merger describe the collective behavior of a coherent ensemble of bubbles with a time-dependent size distribution [57] [58] [59] [60] [61] [62]. Larger bubbles experience less drag per unit volume, as compared to their smaller neighbors. Therefore, successively larger horizontal scales are generated as larger bubbles overtake and assimilate their smaller neighbors, then expand laterally to fill the space. Bubble competition and merger processes drive the system to a longer-wavelength dominate mode $\langle\lambda\rangle$ and characteristic horizontal length scale $L = \langle\lambda\rangle$. This leads to a coherent array of bubbles, or "bubble front," which grows self-similarly, where $h_B(t) \propto L(t)$:

$$h_B(t) = \alpha_B A g t^2 \propto L(t) \tag{2.23}$$

where $\alpha_B > 0$ is a constant whose value depends on the definition of the bubble height (or mixed-layer width).

For multi-mode RTI, several definitions exist for bubble and spike height and total mixed-layer-width [63]. As one example, Youngs defines bubble and spike heights in terms of volume fractions [64]. For each fluid ($_{j\,=\,1,\,2}$), the volume-fraction f_{v_j} is calculated from the mass-fraction f_{m_j} as follows:

$$f_{\mathrm{v}_j} = \Big(\frac{f_{m_j}}{\rho_j}\Big)\frac{1}{f_{m_1}/\rho_1 + f_{m_2}/\rho_2} \tag{2.24}$$

The average value over the xy-plane is $\langle f_{\mathrm{v}_j}\rangle$. Bubble and spike heights are defined as

the z-distance where:

$$\begin{aligned} h_B &: \langle f_{\mathrm{v}_1} \rangle = 0.99 \\ h_S &: \langle f_{\mathrm{v}_1} \rangle = 0.01 \end{aligned} \tag{2.25}$$

Careful consideration should be given to the equivalence between the mixed-layer width computed from numerical simulations and what is measured experimentally. A more fundamental issue is that measurements of spike- and bubble-front position (or velocity and acceleration at the front) are insufficient to distinguish between the late-stage growth of broad-spectrum, multi-mode RTI and turbulent RTI, discussed next in Section 2.3. In both cases, the mixed-fluid layer grows self-similarly. Young's molecular-mix parameter[1] characterizes the total degree of mixing:

$$\Theta = \int_{-h_S}^{h_B} \frac{\langle f_{\mathrm{v}_1} f_{\mathrm{v}_2} \rangle}{\langle f_{\mathrm{v}_1} \rangle \langle f_{\mathrm{v}_2} \rangle} dz \tag{2.26}$$

where $\Theta = 0$ for two regions of pure, unmixed fluids and $\Theta = 1$ for a homogeneous mixture of the two fluids. In the case of multi-mode RTI, the mixing predominately occurs at larger scales (illustrated in Figure 2.3); whereas turbulent RTI is characterized by a high degree of fine-scale mixing (illustrated in Figure 2.4). In addition to the degree of mixing, the kinetic energy spectrum can also distinguish between single-mode, multi-mode and turbulent mixing.

2.3 Turbulent RTI

The generally accepted belief is that a high-Reynolds-number, RT-unstable flow with sufficiently strong, sustained acceleration will lose memory of its initial seed spectrum and evolve to a fully-turbulent state, characterized by a broad kinetic energy

[1] More generally, the mix parameter characterizes mixing at the finest scale: molecular mixing for classical fluids or atomic mixing for HED plasmas.

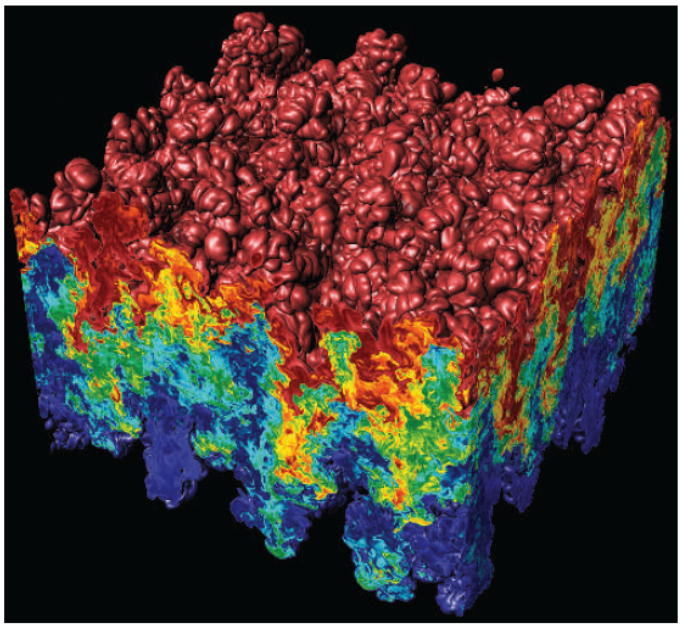

Figure 2.4: 3D simulations of turbulent RTI by Cabot and Cook [65]. Gravity is directed downward. In this color-map, red is the heavy fluid, blue is the light fluid, and other colors represent mixed-fluid regions of various compositions. For illustrative purposes, the pure-fluid regions on the top and bottom are not shown.

spectrum, high degree of molecular mixing (Θ), and self-similar growth:

$$h(t) = \alpha A g t^2 + 2\sqrt{\alpha A g h_0}\, t + h_0 \tag{2.27}$$

Here, h_0 is a virtual origin, corresponding to the mixed-layer width at the time when the growth becomes self-similar [66] [67]. Numerous experiments and numerical simulations seeded with multi-mode perturbations or random noise have observed quasi-self-similar turbulent growth, but with differences in the measured growth parameter α [68]. Much work has been devoted to understanding discrepancies between the values of α predicted by theoretical models, numerical simulations, and experiments. The development of turbulence depends, in some complicated way, on the acceleration history, Atwood number, and seed perturbation spectrum. Recent research also explores the effect of miscibility, which may lead to a lower effective

Atwood number [69].

For various types of stationary flows (shear layers, jets, and other flows), Dimotakis demonstrated that there exists a universal critical Reynolds number, $Re \simeq 2\text{x}10^4$, at which the flow abruptly transitions from laminar to turbulent [70]. The Reynolds number is a dimensionless quantity which relates the strength of the inertial forces to the viscous forces within a flow:

$$Re = \frac{\rho U L}{\mu} = \frac{LU}{\nu} \tag{2.28}$$

Here, L is the outer scale length (representing the driving scale or size of the flow), U is the flow velocity, μ is the dynamic viscosity [mass/(distance·time)], and ν is the kinematic viscosity [area/time]. Laminar flow occurs at low Reynolds number, when viscous forces dominate. At high Reynolds number, inertial forces dominate.

Turbulent mixing requires a broad inertial range in the kinetic energy spectrum, preventing direct coupling between modes in the driven range and modes in the dissipative range. The smallest physical length scale is the Kolmogorov microscale, λ_K, where kinetic energy is converted to heat by viscous dissipation. The Taylor microscale, λ_T, represents the largest length scale (eddy size) at which turbulent kinetic energy is dissipated. The Kolmogorov and Taylor microscales are related to the Reynolds number by [71]:

$$\begin{aligned} \lambda_K &= (\nu^3/\varepsilon_T)^{1/4} = LRe^{-3/4} \\ \lambda_T &= LRe^{-1/2} \end{aligned} \tag{2.29}$$

where ε_T is the turbulent kinetic energy dissipation rate (with units of [area/time]).

Dimotakis defines two additional turbulent length scales:

$$\begin{aligned} &\text{Liepmann-Taylor scale:} \quad \lambda_{LT} \equiv 5\lambda_T \\ &\text{Inner-viscous scale:} \quad \lambda_\nu \equiv 50\lambda_K \end{aligned} \tag{2.30}$$

The Liepmann-Taylor scale represents the longest-wavelength mode which is decoupled from the driven modes. The inner-viscous scale represents the shortest-wavelength mode which is unaffected by viscous dissipation. The transition to turbulence corresponds to the appearance of an inertial range bounded from above by the Liepmann-Taylor scale and from below by the inner-viscous scale:

$$\lambda_\nu \leq \lambda_{inertial} \leq \lambda_{LT} \tag{2.31}$$

Zhou *et al.* provide an excellent plot (Figure 2.5) of the various turbulent length scales and a conceptual illustration of the energy cascade that drives the transition to turbulence (Figure 2.6).

In the case of RTI, the flow is not stationary and the turbulent length scales are time-dependent. Furthermore, for a system initially seeded with a single-mode perturbation, the transition to turbulence requires time for nonlinear interactions to generate higher-order harmonics and a broad inertial range. Zhou *et al.* modified the steady-state mixing transition criteria of Dimotakis to include the temporal evolution of the inertial range [72]. Along the sides of the bubble/spike, a laminar boundary layer forms, whose thickness, λ_D, corresponds to the upper bound of the viscous length scale:

$$\lambda_D = 5(\nu t)^{1/2} \tag{2.32}$$

The time-dependent Kolmogorov and Taylor microscales (and thus λ_{LT} and λ_ν) are calculated from the outer-scale Reynolds number (Equation 2.28), using the total

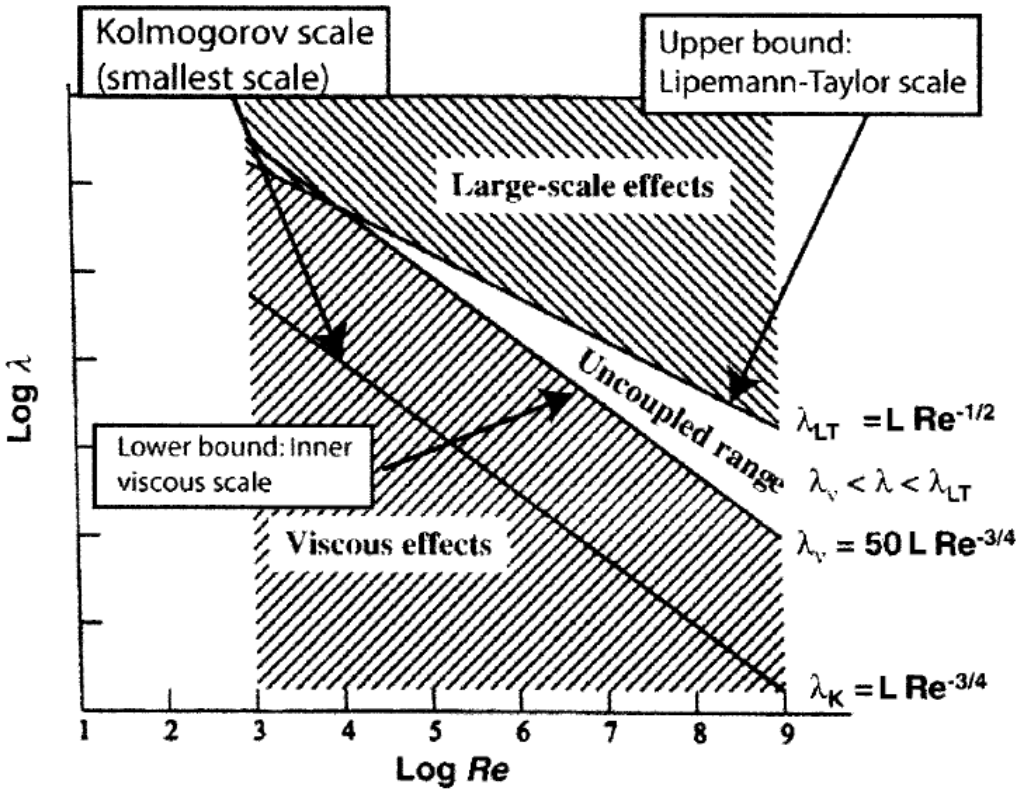

Figure 2.5: Plot of turbulent length scales versus Reynolds number, modified from Zhou *et al.* [72]. Text labels describe the dominate physical processes in the shaded regions bounded by the various length scales. At sufficiently large Reynolds number, an inertial range develops (unshaded region), which corresponds to the onset of turbulence.

mixed-layer height $L = h(t)$ and velocity $U = \dot{h}$. A mixing transition occurs when:

$$\lambda_{min}(t) > \lambda_\nu(t), \text{ where } \lambda_{min} = \min\{\lambda_D, \lambda_{LT}\} \tag{2.33}$$

Unlike the stationary flows studied by Dimotakis, the onset of RTI turbulence is not an abrupt phase transition. The system requires further time to generate the full kinetic energy spectrum and mixing dynamics relevant to extremely high Reynolds-number astrophysical flows. For this, Zhou proposes the concept of a "minimum state" and a critical Reynolds number, $Re = 1.6\text{x}10^5$, which corresponds to [73]:

$$\lambda^*_{min} = \min\{\lambda_D, \lambda_{LT}\} \geq 2\lambda_\nu \tag{2.34}$$

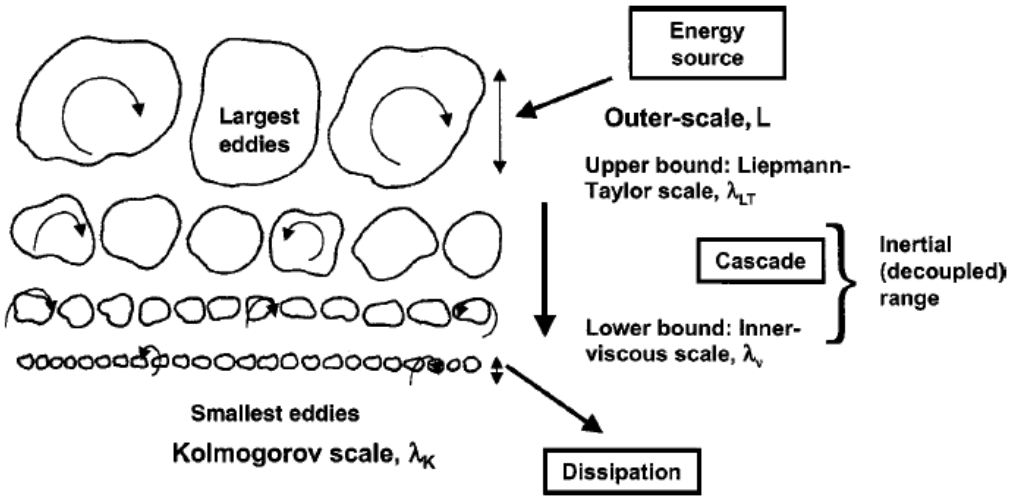

Figure 2.6: Conceptual illustration of the energy cascade that drives the transition to turbulence, showing the correspondence between eddy size distribution and turbulent length scales. Figure from Zhou *et al.* [72].

However, this method of predicting the onset of turbulence and minimum state requires knowledge of spike and bubble velocities from early to late times. Lacking accurate analytical models for the late-nonlinear stage, we rely on numerical simulations.

CHAPTER III

Simulation Studies of Single-Mode RTI at Low Atwood Number

Even with state-of-the-art (2019) supercomputers, it is typically infeasible to run 3D simulations which resolve all physical scales in high-Reynolds-number RTI flows, from the driven scale down to the dissipative scale, for long enough times to observe all stages of RTI, from single-mode linear growth to fully turbulent mixing. The transient nature of turbulence and rapid velocity fluctuations further increase the computational burden. Considerable debate surrounds the choice of numerical methods and their validity for solving particular problems [74]. Different hydrodynamics codes can yield different results for the same physical problem. Two main types of simulations exist for modeling turbulent flows: direct numerical simulations (DNS) and large eddy simulations (LES). DNS are so-named because they "directly" solve the Navier-Stokes equations, including the effects of physical viscosity and diffusion. This requires grid size at the Kolmogorov microscale (Equation 2.29). LES solve the RANS equations using comparatively large grid size and implement either an explicit or implicit model for turbulence and sub-grid-scale dissipation. Additionally, finite grid size creates

numerical viscosity and lower effective Reynolds number [49]:

$$\begin{aligned} &\nu_{\text{num}} \propto \sqrt{Ag\Delta^3} > \nu, \text{ where } \Delta \text{ is the grid size} \\ &Re = \frac{LU}{\nu_{\text{num}}} \end{aligned} \tag{3.1}$$

Previous simulation studies have shown that LES and less-than-fully-resolved DNS adequately model the evolution of RTI in two regimes: a) single-mode RTI through the early-nonlinear and asymptoptic growth stages, and b) fully-turbulent RTI [74]. However, these simulations may not accurately capture the physical processes which strongly influence the transitional behavior between single-mode and turbulent mixing at very high Reynolds number.

Another common approach to reduce computational time while resolving fine scales is to run a 2D simulation, rather than the full-scale 3D system. However, the physical nature of turbulence is fundamentally different in 2D versus 3D. Classical turbulence is inherently a 3D phenomenon, charactered by a forward energy cascade via the mechanism of vortex-ring stretching [71]. In 2D, vortex pairing and merger processes drive a forward enstrophy cascade and an inverse energy cascade [75]. Recent classical fluids experiments by Morgan *et al.* (discussed in Chapter IV) showed that systems initialized with 2D perturbations developed 3D secondary instabilities prior to turbulent mixing [76]. Therefore, 2D simulations are of limited utility for predicting the evolution of 3D physical systems.

3.1 3D LES by Ramaprabhu *et al.*

In 2012, Ramaprabhu *et al.* performed a 3D simulation study of single-mode RTI in the nonlinear stage and dependence on Atwood number [49]. They compared the results of two different LES codes (RTI 3D and PPM), simulating an RT-unstable system consisting of classical, incompressible fluids, initial perturbation

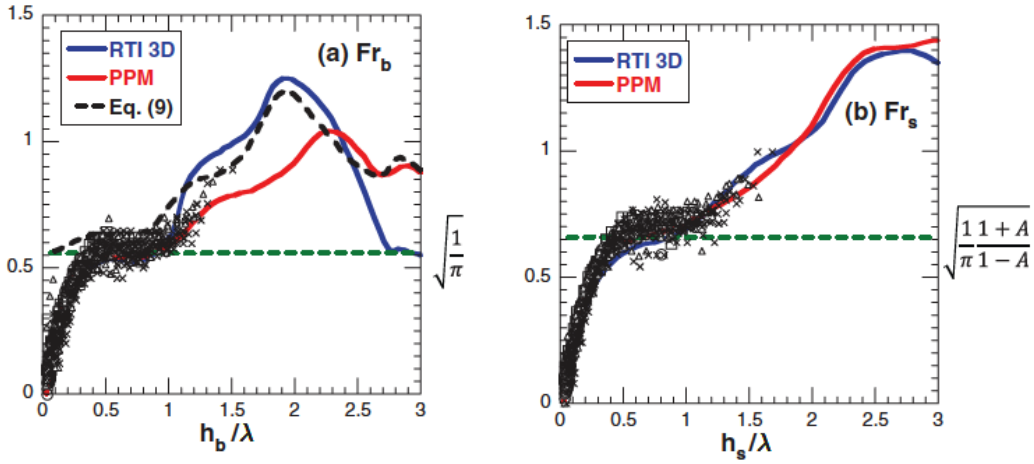

Figure 3.1: $A = 0.15$ simulations by Ramaprabhu *et al.* with experimental data from experiments by Wilkinson and Jacobs. The figures shown here are from Ramaprabhu *et al.* [49]. Froude numbers for bubble (a) and spike (b) are plotted versus the normalized feature height, h/λ. The horizontal green-dashed lines indicate the terminal limits predicted by the potential flow model of Goncharov. In each figure, the blue and red curves are measured from simulation data from two different codes, RTI 3D (blue) and PPM (red). These plots also include data (black markers) from classical fluids experiments by Wilkinson and Jacobs. In the left figure (bubble), the black-dashed curve labeled "Eq. (9)" is calculated from the simulation data and the modified potential flow model (Equation 3.4b in this dissertation).

$h(x, y) = h_0\big(\cos(kx) + \cos(ky)\big)$, constant scaled acceleration, Ag, and scaled viscosity, $\nu_{SCL} \sim \nu/\sqrt{Ag\lambda^3} \approx 10^{-4}$, for numerous Atwood numbers, ranging from $A = 0.005 - 0.9$. Detailed analysis focused on two representative cases: $A = 0.9$ and $A = 0.15$ (similar to the experiments of Wilkinson and Jacobs [77], discussed in Chapter IV). Although the two codes generated slightly different results (in terms of the spike and bubble velocities, interface shape, and small-scale mixing), they predicted the same qualitative behavior. Spikes do not reach a terminal velocity at any Atwood number, and in the high-A limit, spikes approach free-fall. At high-Atwood-number, bubbles do reach a terminal velocity and constant Froude number, consistent with the potential-flow model of Goncharov [45]. The behavior is very different for low-Atwood-number bubbles, which evolve through four distinct stages:

I. Exponential growth (described by linear stability theory)

II. Saturation to terminal velocity (described by potential-flow theory)

III. Reacceleration to a higher Froude number (after plateauing at the terminal velocity of stage II)

IV. Chaotic mixing

The $A = 0.15$ simulations showed excellent agreement with the experiments of Wilkinson and Jacobs, in terms of bubble and spike Froude numbers, shown in Figure 3.1. However, Wilkinson and Jacobs experiments did not drive RTI growth beyond $h_B/\lambda \simeq 1.5$ (corresponding to $\tau \simeq 9$), which is just at the onset of the reacceleration stage ($9 < \tau < 12$). The authors attribute the reacceleration to the emergence of secondary KHI, which manifests as a vortex ring traveling towards the bubble tip. This reacceleration only occurs at low-Atwood-number. At high-Atwood-number, KHI is inertially suppressed (Equation 1.33).

To describe the bubble reacceleration, Ramaprabhu *et al.* adopt a potential-flow model modified with a vorticity term:

$$(\rho_1 - \rho_2)\, g + \rho_2 \frac{\omega_0^2 r}{4} = k \rho_1 u_B^2 \tag{3.2}$$

where $r = \lambda/2$ is the bubble radius. This is based on the Layzer potential-flow model (Equation 2.20) with the drag coefficient $C_2 = 1$ (for the 3D case) and $\dot{u}_B = 0$ (the terminal velocity limit), plus a rigid-body rotator model (Equation 1.17) for the KHI vortex ring. This model was originally developed by Betti and Sanz [78] for the case of ablative RTI (discussed in Chapter IV). Figure 4.3 provides a conceptual illustration of the rigid rotator model, showing accumulation of vorticity in the bubble and how the direction of rotation induces a net velocity in the positive z-direction at the tip of the bubble. In this picture, the angular velocity of the rigid-rotator is $\omega_0/2$ and the

centrifugal force per unit volume is:

$$\frac{\rho_2 u_\theta^2}{r} = \frac{\rho_2}{r}\left(\frac{\omega_0}{2}r\right)^2 = \rho_2\frac{\omega_0^2 r}{4} \tag{3.3}$$

Equation 3.2 predicts higher values for the terminal velocity and Froude, as compared to the classical potential flow model of Goncharov (Equation 2.22):

$$u_B = \sqrt{\frac{2Ag\lambda}{(1+A)k} + \frac{\rho_2}{\rho_1}\frac{\omega_0^2}{4k^2}} \tag{3.4a}$$

$$Fr_B = \sqrt{\frac{1}{\pi} + \frac{\rho_2/\rho_1}{1-\rho_2/\rho_1} + \frac{\omega_0^2}{4\pi kg}} \tag{3.4b}$$

However, Ramaprabhu *et al.* do not assume a constant value of ω_0. Instead, they calculate the quantity $\omega_0(t)$ at each time step in the numerical simulation by spatially averaging the vorticity field over a region inside the bubble tip. This region is bounded by the horizontal half-plane of the bubble (bisected through the vertex) and vertical extent of the KH vortex ring, λ_{KH}.

In the simulation, the reacceleration stage ends at $\tau \simeq 12$, when single-mode structure breaks down, symmetry is lost, and the chaotic mixing stage begins. Ramaprabhu *et al.* characterize "chaotic mixing" in a manner which resembles turbulence: increase in atomic mixing Θ due to small-scale, incoherent structures inside the bubble and corresponding decrease in Froude number associated with the fundamental mode. At the latest simulation time (corresponding to $\tau = 16$), the long-term trend for bubble growth is unclear.

Ramaprabhu *et al.* also performed a resolution study with $\lambda/\Delta = \{8, 16, 32, 64, 128\}$. The authors conclude that $\lambda/\Delta = 64$ is sufficient to predict the overall dynamics in stages I-III, where large-scale coherent features dominate. In the chaotic mixing stage, significant variability was observed at higher resolutions, corresponding to velocity

fluctuations caused by small-scale features. To quantify the uncertainty related to grid-size effects, they performed an ensemble of $10 - 25$ simulations (at each of the highest resolutions, $\lambda/\Delta = 64, 128$) with the ensemble generated by small perturbations in the scaled viscosity (around the nominal value of 10^{-4}). As a metric, they plotted single-mode spike- and bubble-Froude number versus τ for the ensemble-average with error bars indicating the standard deviation. In the early growth stages the error was small, but the later growth stages exhibited large stochastic fluctuations.

3.2 2D DNS by Wei and Livescu

Later in 2012, Wei and Livescu published the results of 2D, high-resolution DNS of single-mode RTI at low-Atwood-number, $A = 0.04$ [79]. (The authors also ran one simulation at $A = 0.15$ and found good agreement with the 2D experiments of Waddell *et al.* [80], discussed in Chapter IV. However, in those experiments, RTI was not driven beyond the potential-flow stage.) The $A = 0.04$ simulations investigated dependence on resolution, Reynolds number, and initial perturbation shape (wavelength, amplitude and thickness of the initial diffusion layer). The interface was initialized with the density profile: $\rho(x, z) = \frac{1}{2}\{1 + \text{erf}[Yz + h(x)]\}(\rho_1 - \rho_2) + \rho_2$, where $h(x) = a\sin(kx)$ and Y is a slope coefficient. (The initial perturbation amplitude of the density profile is a/Y.) Simulation parameters included constant acceleration, unity Schmidt number ($Sc = \nu/D$, where D is the mass diffusion coefficient), horizontal resolution $\lambda/\Delta_x =$ 256-2048 and vertical resolution $\Delta_z = 0.8\Delta_x$.

For bubbles, they identify five growth stages:

I. Diffusive growth (described by the solution to the heat equation)

II. Exponential growth (described by linear stability theory)

III. Potential flow growth

IV. Reacceleration

V. Chaotic development

Evolution through these stages is determined by the perturbation Reynolds number, which they define as:

$$Re_p \equiv \frac{\lambda}{\nu}\sqrt{\frac{Ag\lambda}{1+A}} \tag{3.5}$$

where $U = \sqrt{\frac{Ag\lambda}{1+A}}$ reflects the asymptotic terminal velocity of potential-flow models. At low perturbation Reynolds number ($Re_p \lesssim 200$), the system does not evolve beyond the potential-flow stage. At higher Reynolds number ($Re_p \gtrsim 300$), a transition between potential-flow and reaccleration stages occurs. Chaotic development begins at $Re_p \approx 2,000$, but fully chaotic growth only occurs above a critical perturbation Reynolds number, $Re_p \approx 10^4$.

At sufficiently high Re_p, bubbles reaccelerate beyond the velocity plateau predicted by potential-flow theory. This reacceleration is driven by secondary KHI, which begins when vortices (formed in the early nonlinear growth stage) become large enough to interact with their neighbors. The initial vortices split and form coherent pairs of counter-rotating vortices (with one vortex on either side of the bubble/spike). Along the interface, secondary KHI continues to generate complex, small-scale vortical interactions. The first generation of vortex-pairs self-propels towards the spike and bubble tips, inducing a net-increase in velocity along the vertical direction. This acceleration must end when the vortices reach the spike and bubble tips, as the velocity can no longer increase. The reacceleration stages of Ramaprabhu *et al.* and Wei and Livescu arise from analogous physical processes in two- and three-dimensions. In 3D, reacceleration is caused by the formation of a secondary set of vortex rings which travel towards the spike/bubble tip, producing an effect similar to the counter-rotating vortex-pairs in 2D.

However, the mixing dynamics are very different in the "chaotic development"

stage of Wei and Livescu and the "chaotic mixing" stage of Ramaprabhu *et al.* In the simulations of Wei and Livescu, symmetry is preserved at all times[1] and the flow structures are coherent. The flow never evolves to turbulent mixing. "Chaotic" refers to seemingly-random velocity fluctuations at the bubble tip caused by complex, small-scale vortical interactions. At very high Reynolds number ($Re_p \gtrsim 10^4$), bubble acceleration eventually becomes "stationary" and the growth is "fully chaotic." In other words: acceleration at the bubble tip fluctuates chaotically about a constant, positive mean-value: $\ddot{h}_B/(2Ag) = \alpha_B$. For bubble height defined at the 1 % density level, $\alpha_B \approx 0.035$. The authors claim that mean-quadratic growth shows "there is no fundamental difference between single-mode and multi-mode RTI."

Wei and Livescu also investigated the role of the initial perturbation amplitude and diffusion-layer thickness, using various combinations of a and Y. These simulations were performed at the highest resolution ($Re_p = 20,000$) to ensure that the flow would evolve through all five growth stages. Their results showed a strong dependence on initial conditions in the early growth stages (I and II) and time-of-transition between growth stages. In the potential-flow stage, the asymptotic velocity was unaffected by the initial conditions. In the later growth stages (especially the chaotic stage), differences in initial conditions seeded secondary instabilities which caused large differences in the instantaneous bubble acceleration, but at sufficiently late times, there was no difference in the mean-acceleration.

[1]The flow preserves mirror symmetry about the vertical axis bisecting the bubble. The interface is not symmetric about the horizontal plane.

CHAPTER IV

Previous Experiments of Single-Mode RTI

4.1 Classical Fluids Experiments

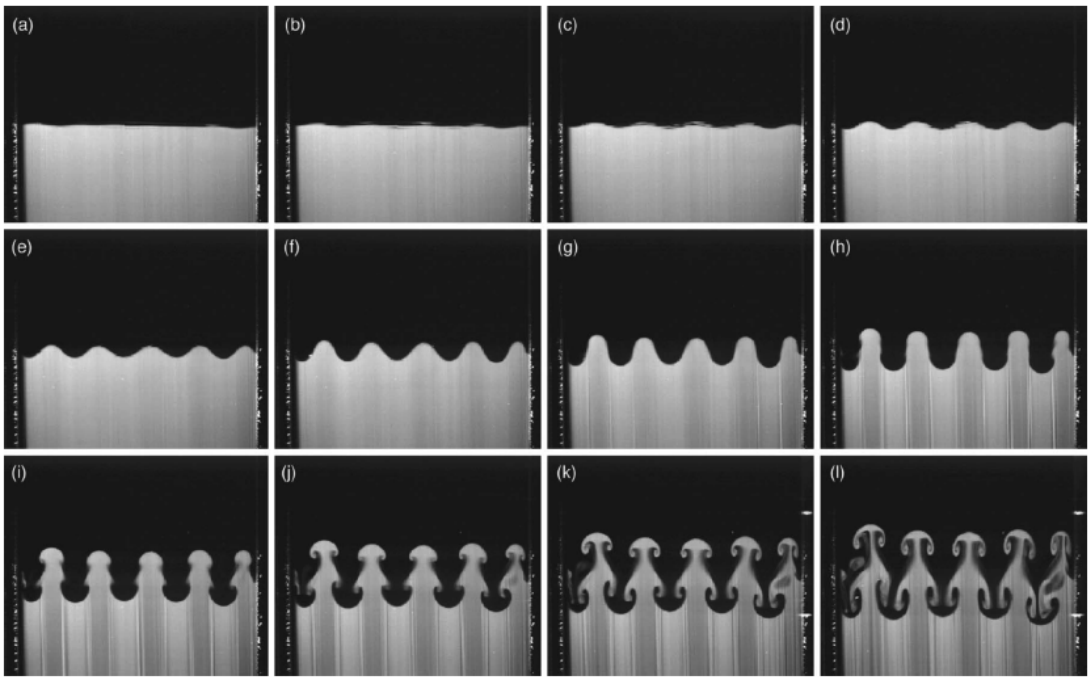

Figure 4.1: Classical fluids experiments of 3D single-mode RTI by Wilkinson and Jacobs [77]. In the laboratory frame of reference, the less-dense fluid is on the top (dark color) and the denser fluid is on the bottom (light color). PLIF imaging captures the detailed structure of the interface throughout the duration of the flow. Times shown: (a) -26.7 ms (seed perturbation); (b) 40 ms; (c) 106.7 ms; (d) 173.3 ms; (e) 240 ms; (f) 306.7 ms; (g) 373.3 ms; (h) 440 ms; (i) 506.7 ms; (j) 573.3 ms; (k) 640 ms; (l) 706.7 ms.

Advantages of classical fluids experiments include diagnostics with high spatial and temporal resolution relative to the size and speed of the flow, and well-known equations-of-state and kinematic viscosities for a wide variety of liquid and gas combinations. Additionally, chemical dopants and nano/micro-scale engineered particles may be added to the fluids to enable measurements of the degree of molecular mixing and kinetic energy spectrum of turbulent velocity fluctuations [81], [82]. Typical flow durations are on the order of hundreds of milliseconds to several seconds for flow sizes ranging from tens to hundreds of millimeters. Optically transparent fluids with mass-densities in the range of $10^{-4} - 1$ g/cm^3 enable the use of sophisticated imaging techniques, such as particle-image velocimetry (PIV), planar laser-induced fluorescence (PLIF) imaging, and Mie scattering. Compatible detectors include CMOS cameras with micron-scale pixels, large array sizes (thousands of pixels in each linear dimension), single-photon sensitivity, and frame rates >10 kHz.

In 2010, Andrews and Dalziel published a review of classical fluids experiments of RTI turbulence at low-Atwood-number, describing advances in experimental apparatus and diagnostic techniques over the previous 20-year period [83]. In all these experiments, turbulent RTI mixing resulted from uncontrolled multi-mode initial conditions. It is much more difficult to drive single-mode RTI deep into the nonlinear growth stage and observe the transition to turbulence. Challenges include creating strong, sustained acceleration, achieving very high Reynolds number ($Re > 10^4$), creating a true single-mode seed perturbation unaffected by surface tension and wall interactions, and resolving the spatial and temporal dynamics. To reach late τ (Equation 2.17), a low-Atwood-number experiment requires more acceleration than a high-Atwood-number experiment of the same wavelength.

4.1.1 Incompressible, Miscible Fluids Experiments at Low Atwood Number

In 2001, Waddell *et al.* performed liquid-phase experiments of 2D single-mode RTI with at low-Atwood-number ($A = 0.15$) [80]. In 2007, Wilkinson and Jacobs extended this platform to create 3D perturbations and published the first experimental study of 3D single-mode RTI growth at low-Atwood-number [77]. The experimental apparatus consisted of a Plexiglass tank accelerated downward on a vertical rail. Inside the tank, the lighter fluid (solution of isopropyl alcohol and water) was suspended on top of the heavier fluid (solution of calcium nitrate and water, doped with a fluorescent dye). Oscillating the tank about its diagonal created a standing-wave initial perturbation of the form $z_0(x, y) = a\sin(kx)\sin(ky)$ with 1.5, 2.5 or 4.5 wavelengths spanning the tank. A weight-and-pulley system accelerated the tank downward for a travel time of 300-500 ms, while accelerometers measured $g(t)$ at a sampling rate of 15 kHz. A planar laser-induced fluorescence imaging system with a video camera recorded the mixed-fluid region at a frame rate of 60 Hz. RTI growth was driven well into the nonlinear stage, but not to turbulence. Spike and bubble growth appeared to saturate at the terminal velocity predicted by Goncharov (Equation 2.22), but then unexpectedly began to reaccelerated at latest measurement times. Wilkinson and Jacobs attribute this late-time re-acceleration to the formation of vortex rings, which impart a net velocity in the z-direction. For each bubble-spike pair, they observed two vortex rings, one propagating towards the bubble tip and the other towards the spike tip. These experiments motivated the 2012 simulation study by Ramaprabhu *et al.* [49].

4.1.2 Compressible, Miscible Fluids Experiments at Moderate-to-High Atwood Number

During 2016-2018, Morgan *et al.* published in two installments the results of rarefaction-driven, gas-phase experiments of 2D and 3D single-mode RTI initiated at a diffuse interface [84] [76]. Different gas-pairings produced a variety of Atwood numbers ($A = 0.49 - 0.94$). The first publication provides a detailed description of the experimental apparatus, measurement techniques, and compares experimental results with a model based on diffuse-interface linear stability theory. The second publication explores the nonlinear regime, comparing experimental results with the variable-density potential-flow model of Mikaelian [85] and numerical simulations with two different codes: Miranda and Ares. Miranda is a compressible LES code with 2D or 3D Cartesian grids. The transverse domain of the Miranda simulations spanned one wavelength with fixed resolution ($\lambda/\Delta_{x,y} = 256$) and periodic boundary conditions. Resolution in the vertical direction depended on the wavelength of the experiment. Ares is an axi-symmetric arbitrary Lagrangian-Eulerian (ALE) code with cylindrical coordinates and constant properties in the azimuthal direction. For the Ares simulations, the transverse domain spanned one-half wavelength with the axis of symmetry through the center of either the spike or bubble and 1D reflecting conditions at the opposite boundary. In the transverse direction, adaptive mesh refinement resulted in $\lambda/\Delta_r = 400 - 500$. Vertical resolution was fixed with 1350 points along the entire length of the rarefaction tube (equivalent to approximately $\lambda/\Delta_z = 150$). Miranda simulations were performed for all Atwood-number cases, whereas Ares simulations were performed only for the $A = 0.63$ case.

For each gas-pairing, the Atwood number remained nearly constant over the duration of the experiment (7 seconds), decreasing slightly over time. Outer-scale Reynolds numbers ranged from $1\text{x}10^5 - 9\text{x}10^5$ and perturbation Reynolds numbers ranged from $9\text{x}10^4 - 6\text{x}10^5$, exceeding the critical values of both Zhou and Wei and Livescu.

Rocking the gas-filled tube side-to-side created 2D standing-wave perturbations of the form $z_0(x) = a\cos(\frac{2\pi}{\lambda}x)$ with 1.5 waves for $A = \{0.49, 0.63, 0.82, 0.94\}$, 2.5 waves for $A = \{0.49, 0.63\}$, or 3.5 waves for $A = 0.49$. 3D perturbations were generated by a different mechanism: a loud speaker vertically oscillated the column of gas, producing perturbations of the form $z_0(x, y) = \frac{a}{2}\left(\cos(\frac{2\pi}{\lambda}x) + \cos(\frac{2\pi}{\lambda}y)\right)$ with only one wavelength spanning the tube. The 3D experiments were performed at two different Atwood numbers, $A = \{0.49, 0.63\}$. Separate 3D experiments were conducted with either the bubble or the spike centered in the tube. A 12 kHz frame rate, high-resolution imaging system based on laser-illuminated Mie scattering recorded a planar projection of the interface shape and enabled measurement of instantaneous velocities at the spike and bubble tips. A separate shadowgraph imaging system captured the three-dimensional structure of the interface.

2D simulations and experiments showed spike and bubble growth approached a velocity plateau in the nonlinear stage. In the linear and early nonlinear growth stages, simulations, experiments, and the Mikaelian model produced similar values for spike and bubble velocities and Froude numbers. However, experimentally measured spike amplitude greatly exceeded the values from simulations (bubble amplitudes were accurately predicted by simulations). In the late-nonlinear stage, significant differences emerged between experiments and simulations, corresponding to the onset of secondary instabilities. In the 2D, 3.5-wave, $A = 0.49$ experiment, spike and bubble growth reaccelerated beyond the velocity plateau, then individual spikes and bubbles broke up, followed by turbulent mixing. Mie scattering clearly showed the development of secondary KHI along the thin arms of the spikes and also at the spike tips. Shadowgraphy revealed that the initially-2D interface developed 3D structure. The simulations generated symmetric, large-scale 2D vortices along the spike arms, but no vorticity at the tips. In the simulations, the interface structure remained symmetric and predominately single-mode.

3D spike experiments showed the development of secondary KHI at the spike tip, in addition to along the arms of the spike. In the 3D bubble experiments, pronounced secondary RTI formed at the bubble tip and rapidly engulfed the entire bubble. 3D Miranda simulations generated larger-scale, symmetry-preserving vortices along the edges of the spike/bubble, but failed to produce the secondary instabilities at the spike and bubble tips. Miranda and axi-symmetric Ares simulations produced similar values for spike amplitude, in good agreement with the experimental data at all measurement times. However, the two types of simulations greatly differed in terms of bubble amplitude, with the Ares simulations closer to the experimental result, but also failing to match experiments in the late-nonlinear stage. In contrast to the Wilkinson and Jacobs experiments, the 3D experiments of Morgan *et al.* produced a single vortex ring, traveling towards the spike tip. Boundary-layer effects at the tube walls (not included in simulations) significantly affected the evolution of the 2D, 1.5-wave and 3D, one-wave experiments.

4.2 High-Energy-Density Experiments of RTI

For the class of high-energy-density experiments considered here, typical flow durations range from 5-50 ns with fluid velocities of $10 - 100$ μm/ns [86] [87] [88] [89] [90] [91] [29] [92] [78] [93] [94]. Diagnostic capabilities for HED experiments are crude in comparison to classical fluids experiments and considerable uncertainty may exist in the EOS and kinematic viscosity. One advantage is that initially-solid materials can be machined (or otherwise fabricated) for precise control of the seed perturbation. It is possible to create 2D and 3D single-mode sinusoidal patterns on a planar surface with many waves (20-50+ λ) spanning the transverse domain. Additionally, a wide variety of interface structures and geometries are possible, enabling experimental studies of multi-mode RTI and bubble-merger processes [62], dependence on spectral content and phase [95] [96] [97] [75], symmetry and pattern formation [98], and RTI growth

at spherical [99] and cylindrical surfaces. Experiments of RTI growth at a planar surface enable more straightforward interpretation of the data and direct comparisons with classical fluids experiments. These capabilities of HED experiments enable progress towards the fundamental understanding of RTI, in addition to studying the interaction of hydrodynamic instabilities with other physical processes unique to HED environments [100], [101], [87]. HED experiments of RTI investigate three different regimes where the instability evolves: 1) at an ablation surface, 2) at a light-to-heavy embedded interface which is shocked and then accelerated, and 3) at a heavy-to-light embedded interface which is shocked and then decelerated by a blast wave.

4.2.1 Ablative RTI

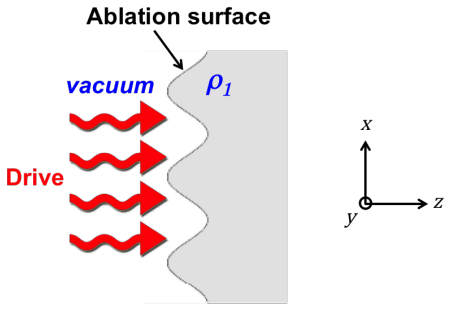

Figure 4.2: Conceptual illustration of RTI at an ablation surface.

Ablative RTI is primarily of interest to the ICF community. In the linear stage, mass ablation suppresses RTI, compared with the classical growth rate γ_{RT}. For ablative RTI, the linear growth rate is [91]:

$$\gamma_{abl} = \alpha\sqrt{\frac{Akg}{1+kL}} - \beta k V_a \tag{4.1}$$

where $L = \rho/\nabla\rho$ is the density gradient length scale (here ρ is the peak density), $V_a = \frac{1}{\rho}\frac{dm_a}{dt}$ is the ablation velocity, m_a is the areal mass density, and α, β are fitting parameters. In the nonlinear stage, Betti and Sanz showed that mass ablation causes vorticity convection [78]. Vorticity accumulates inside the bubble at the tip, increasing

the net velocity in the z-direction. Figure 4.3 provides a conceptual illustration of this model, with the relevant length scales and direction of the flow. In the late-nonlinear stage, the ablative growth rate exceeds the classical asymptotic limit:

$$U_B^{abl} = \sqrt{\frac{2Ag}{k(1+A)} + \frac{\rho_2}{\rho_1}\frac{\omega_0^2}{4k^2}} \tag{4.2}$$

where first term is the terminal velocity from the Layzer-type potential flow model (Equation 2.22) and $\omega_0 \sim kV_a\frac{\rho_1}{\rho_2}$ corresponds to the vorticity convected inside the bubble. Ramaprabhu *et al.* applied this theory to explain the reacceleration observed in their non-ablative, incompressible fluids simulations, although the mechanism for vorticity transport is different [49].

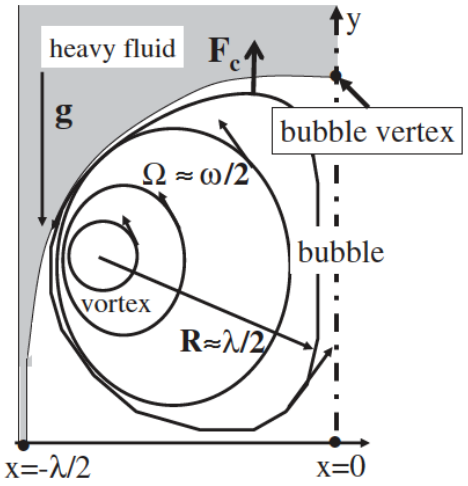

FIG. 1. Sketch of a vortex located inside half of the bubble. The vortex has a radius of about $\lambda/2$ and rigid rotation frequency Ω equal to half the vorticity.

Figure 4.3: Conceptual illustration by Betti and Sanz [78], showing accumulation of vorticity inside the bubble, which resembles a rigid rotator and induces a net velocity in the positive z-direction at the bubble tip.

4.2.2 RTI at an Embedded Interface: Accelerating Thin-Foil Experiments

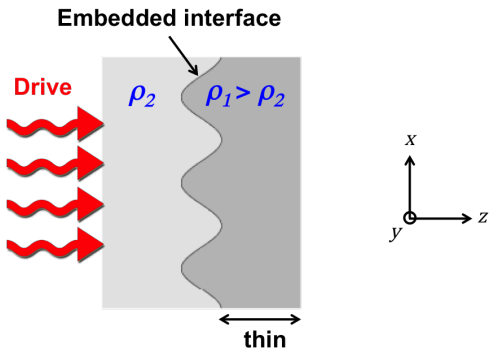

Figure 4.4: Conceptual illustration of RTI at an embedded interface on a thin foil.

In 1996, Budil *et al.* performed the first experiments comparing ablative RTI with classical RTI at an embedded interface [90]. These planar, embedded-interface targets consisted of a Bromine-doped polystyrene ($C_{50}H_{47}Br_3$) ablator pressed against a thin Ti foil with a 2D single-mode sinusoidal perturbation at the material interface. Face-on radiography enabled the use of very short perturbation wavelengths: $\lambda = \{10, 20, 50, 100\ \mu\text{m}\}$ with $a = 0.5\,\mu\text{m}$ for $\lambda = 10\,\mu\text{m}$ and $a = 1\,\mu\text{m}$ for the longer wavelengths. The CHBr ablator had a thickness of 50-60 μm and a density of $\rho_2 = 1.26\,\text{g/cm}^3$. The Ti foil was 15 μm-thick with a density of $\rho_1 = 4.5\,\text{g/cm}^3$. The flat, exterior surface of the ablator was coupled to a hohlraum driven by a 3 ns laser pulse, launching a shock into the target. RTI growth occurs after the drive pulse ends and the shock breaks out at the rear surface of the target.

The Richtmyer-Meshkov instability occurs when a shock wave crosses a rippled interface between two materials of different densities. In the case where the shock travels from a less-dense material into a denser material, the perturbation amplitude immediately begins to grow, increasing linearly with time. If RMI growth is not driven beyond the linear stage, the interface retains a predominately single-mode sinusoidal shape. RTI growth begins when the shock wave breaks out at the rear surface of the

target, creating a rarefaction which accelerates the interface. In the experiments of Budil *et al.*, the shock-wave crossed the embedded interface at t=2.7 ns and broke out at the rear surface of the Ti foil at t=2.9 ns, accelerating the target for approximately 2 ns.

Face-on X-ray radiography with a backlighter source of 6.7 keV photons and a gated detector captured data at a few discrete time steps during the RTI growth phase. In the radiography data, image intensity corresponds to:

$$I(x,y,t) = I_0(x,y)e^{-\kappa\rho_a}, \text{ where } \rho_a(x,y,t) = \int \rho(x,y,t)\, dz \tag{4.3}$$

where I_0 is the backlighter source distribution, κ is the average X-ray opacity, and ρ_a is the areal density. The variation in areal density between bubbles and spikes modulates the image intensity. The RT growth factor is calculated from the Fourier transform of $I(x,y,t)$ and comparing the peak-to-valley contrast of the fundamental mode. Face-on radiography only requires spatial resolution $< \lambda$. The limitation of this diagnostic method is that the perturbation amplitude can only be calculated accurately in the linear growth stage, before the formation of KH roll-ups [87].

4.2.3 RTI at an Embedded Interface: Blast-Wave-Driven Experiments

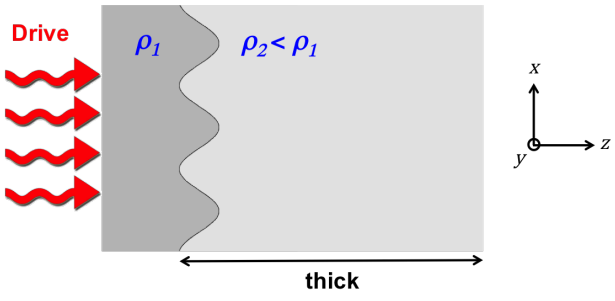

Figure 4.5: Conceptual illustration of blast-wave-driven RTI.

In this case, the ablator is the denser material. When the drive pulse ends, a rarefaction wave forms at the front surface of the ablator. The head of the rarefaction

travels faster than the shock front, forming a blast wave prior to shock break-out at the interface. During the RMI phase (when the shock front crosses the ripped interface), the initial perturbation amplitude is compressed and inverted, then increases. A strong shock travels forward into the lower-density material and a weak shock is reflected back into the ablator. At the interface, the pressure on the side of the lower-density material now exceeds the pressure on the side of the ablator ($\nabla p \cdot \nabla \rho < 0$), the interface decelerates, and the RTI growth phase begins. The blast wave continues to travel in the lower-density material (which is very thick) for tens of nanoseconds, driving RTI growth. The temporal dynamics of the blast wave and time-dependent acceleration/deceleration at the interface are a critical part of the experimental design, discussed in Chapter V.

Side-on radiography measures the peak-to-valley amplitude of the mixed-fluid layer. For radiography through the y-axis:

$$I(x,z,t) = I_0(x,z)e^{-\kappa\rho_a}, \text{ where } \rho_a(x,z,t) = \int \rho(x,y,z,t)\, dy \tag{4.4}$$

To resolve the spikes and bubbles, this radiography configuration requires spatial resolution $\leq \lambda/4$. The target materials and X-ray energy of the backlighter source are chosen for large opacity-contrast between spikes and bubbles.

This blast-wave-driven platform was originally developed by Kane *et al.* as a laboratory testbed for studying the evolution of hydrodynamic instabilities under conditions relevant to supernovae [28] [102]. Early indirect-drive experiments were performed at the Nova laser facility, formerly located at Lawrence Livermore National Laboratory and decommissioned in 1999. The Nova targets consisted of two planar layers: a copper ablator ($\rho_1 = 8.9\,\mathrm{g/cm^3}$, $85\,\mu$m thick) backed by polyethylene plastic (CH_2, $\rho_2 = 0.95\,\mathrm{g/cm^3}$, $500\,\mu$m thick) with a 2D single-mode sinusoidal perturbation at the interface ($\lambda = 200\,\mu$m, $a = 20\,\mu$m).

In 2001, Robey *et al.* extended the supernova platform to direct-drive experiments at the Omega laser facility [103]. Innovations to the design included packaging the target inside a shock tube, which laterally confines the flow and improves planarity, and a plastic ablator with a density-matched tracer strip, which enhances radiography contrast near the central axis of the target. (Chapter V provides a more detailed explanation of the tracer strip.) The lower-density material was carbonized resorcinol-formaldehyde, $C_{1000}O_{48}H_{65}$ (CRF), a type of organic aerogel, commonly referred to simply as "foam" in the HED community. Although many different types of foams exist, CRF is a popular material for HED experiments because of its widely tunable density range ($0.01 - 0.4\,\mathrm{g/cm^3}$), determined by the porosity of the material) and because it is comprised of mostly carbon atoms. CRF has the lowest-atomic-number chemical composition of all porous materials currently available [104]. Applications in ICF seek to eliminate high-atomic-number contaminants. For HED experiments involving X-ray radiography, CRF is highly desirably because it is relatively transparent in its "pure" form, but can be doped with higher-atomic-number elements if desired.

Subsequent experiments based on this supernova platform specifically investigated the nonlinear growth stage of RTI (at later times than is possible with thin-foil targets), including 2D single-mode and multi-mode perturbations [105] [106] and 3D single-mode perturbations [107]. Miles *et al.* investigated the dependence on initial conditions and transition to turbulence with various seed spectra in 2D [95] and 3D [75]. Kuranz *et al.* demonstrated dual, orthogonal side-on radiography [108]. All of these experiments were in the high-Atwood-number regime (ablator density $\rho_1 = 1.4\,\mathrm{g/cm^3}$, foam density $\rho_2 = 0.05 - 0.1\,\mathrm{g/cm^3}$, corresponding to post-shock $A \geq 0.6$). Several of these high-Atwood-number experiments demonstrated anomalous spike morphology and faster spike growth than predicted by buoyancy-drag models and simulations [107] [109] [110] [111]. Possible explanations include the interaction with other physical processes in the HED system, experimental uncertainties, or the failure

of analytical models and numerical simulations to accurately predict the late-nonlinear stage of classical RTI.

For a high-Atwood-number target with a single-mode seed perturbation ($\lambda = 50\,\mu$m), Robey *et al.* estimate the time-dependent kinematic viscosity and Reynolds number [112]. For the kinematic viscosity, they evaluate the formulas of Braginskii and Clérouin *et al.* (Section 1.3.2) with plasma parameters from a 1D Hyades simulation. (However, they do not specify which equations of state were implemented in the simulation or how well the simulation matched the experimental data.) Both models agreed within a factor of two and predicted nearly constant post-shock values of $\nu_1 \sim 0.1$ and $\nu_2 \sim 0.04\,\mathrm{cm}^2/\mathrm{s}$ for the plastic and foam, respectively. The experimental data set was small: mixed-layer width measured at just three moments in time during the nonlinear growth stage. From this, they calculate $L = h(t)$ and $U = \dot{h}$ from a linear fit to the data. Using kinematic viscosity from the Clérouin model, they calculate the Reynolds number and show that it exceeds the critical threshold of Dimotakis ($Re > 2 \times 10^4$); however, calculation of the time-dependent turbulent length scales (Equations 2.30-2.32) show that additonal time is required to achieve the minimum state of Zhou (Equation 2.34). In the experiments, the mixing remained predominately single-mode at the latest measurement time ($\sim$ 15 ns).

CHAPTER V

Experimental Design

The experimental configuration at Omega-60 (shown in Figure 5.1) involves of three targets: the main target and two "backlighter" targets (which generate X-ray sources for radiography). The main target consists of a plastic ablator abutted to a lower-density foam inside a shock-tube. A one-nanosecond laser pulse incident on the outer surface of the ablator creates a blast wave, which drives RTI growth for tens of nanoseconds at the embedded material interface. The blast wave propagates in the z-direction. A sinusoidal ripple pattern is machined on the surface of the ablator in contact with the foam, creating a single-mode seed perturbation. X-ray radiography probes the target along two orthogonal axes, aligned to the x, y axes of the sine-wave pattern. For each target shot, two radiography images (one per axis) are obtained, either at the same moment in time or two different times. To measure the growth rate of the mixed-fluid region from early to late times, we must shoot several identical targets and build a time-series of radiography images. Unless otherwise stated, time is referenced to the start of the laser drive pulse and position is measured relative to the laser-irradiated surface of the ablator.

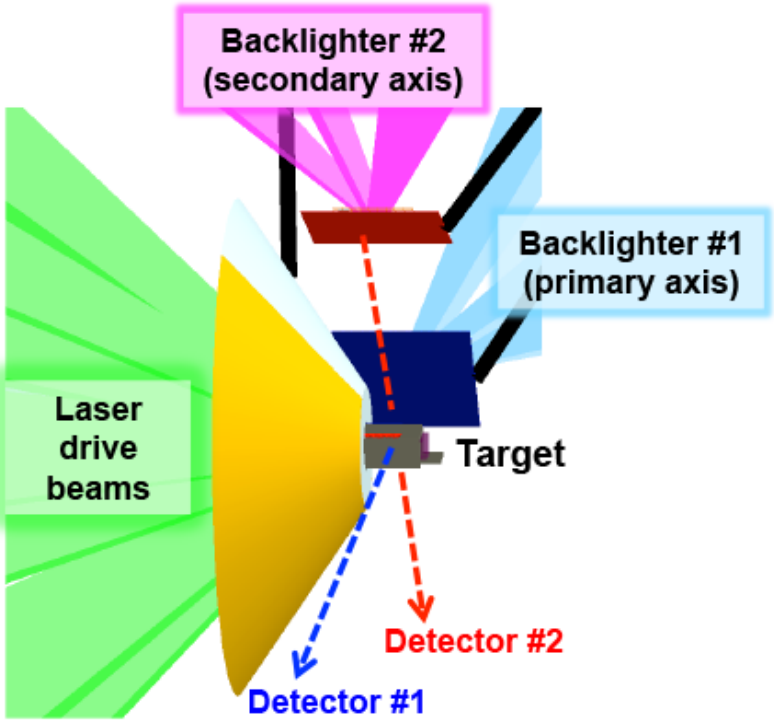

Figure 5.1: Visrad model of experimental configuration with main target and two backlighter targets.

5.1 Experimental Goals

This work represents the first experimental investigation of the late-nonlinear growth stage of single-mode RTI in a low-Atwood-number HED system. Experimental campaigns of this nature often involve several design iterations over the course of many years. The long-term experimental objectives are to: 1) drive single-mode RTI growth to the late-nonlinear stage in a low-Atwood-number system; 2) measure the growth of the mixed-fluid region throughout the nonlinear stage; 3) observe whether the system transitions to turbulent mixing; and 4) compare the evolution of 2D versus 3D single-mode RTI in otherwise identical systems.

Based on the results of the first shot day (October 6, 2016), we calibrated numerical simulations to the experimental data and refined the target design. 2D CRASH simulations of the new design predicted that the Omega-60 platform was unlikely to provide enough deceleration during the RTI growth phase to reach the late-nonlinear

regime of interest. These simulation results were published by Tim Handy and Guy Malamud [42]. However, a higher energy laser facility, such as the National Ignition Facility (NIF), could potentially drive RTI growth to later times. For the Omega-60 experiments presented here, our goals were to: 1) demonstrate a design which achieves post-shock Atwood number $A \simeq 0.2$ utilizing existing target fabrication and diagnostic capabilities; and 2) identify potential issues with the experimental design and/or target fabrication methods which must be addressed in order to extend these experiments to the NIF.

5.2 Evolution of the Target Design

The experimental campaign at Omega-60 consisted of four shot days: October 6, 2016, April 6, 2017, April 19, 2018, and July 18, 2018. In addition to the low-Atwood-number targets, we also designed, built, and shot several high-Atwood-number targets. The low- and high-A targets were identical, except for the density of the CRF foam. (For the high-A targets, the foam density was $\rho_2 = 0.05\,\mathrm{g/cm^3}$.) The purpose of the high-A targets was to provide data for validation of numerical simulations and comparisons with prior experiments. The high-A data is not discussed in this dissertation, but is included in the shot log for reference (Appendix C).

The experimental design is based on the blast-wave-driven platform discussed in Section 4.2.3. Previous high-Atwood-number targets featured low-density ($\rho_2 = 0.05 - 0.1\,\mathrm{g/cm^3}$) CRF foam, a "top hat" shape ablator, and a cylindrical polyimide (PI) shock tube with inner diameter $\sim 900\,\mu$m and $25\,\mu$m wall thickness. The first shot day fielded the cylindrical shock tube design, shown in Figure 5.2. For the low-A targets, the higher pressure inside the shock tube caused the PI walls to breach. This motivated a new shock tube design, which features $200\,\mu$m-thick Beryllium (Be) walls. The increased wall thickness improves lateral confinement of the flow. As compared to PI, Be is much more transparent in the soft-X-ray spectrum of the backlighters.

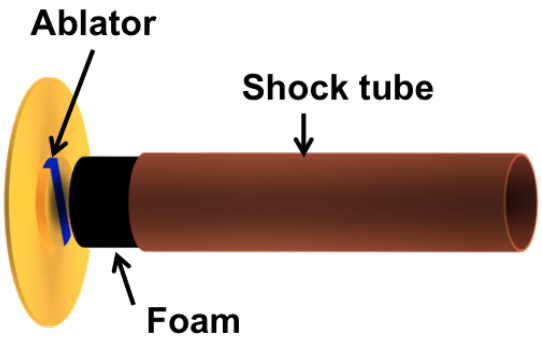

Figure 5.2: CAD model by Sallee Klein of first-generation target design with cylindrical shock tube and "top hat" style ablator.

At 7.8 keV, the net transmission through 200 μm Be is comparable to 25 μm PI. Our collaborators at LLNL also recommended a change to a rectangular shock tube design, similar to targets used at NIF [113].

The simulations shown in this chapter guided the preliminary design, but do not represent a quantitatively accurate model of the final design. 1D Hyades simulations illustrate conceptual aspects of the target design and provide crude, qualitative comparisons (for example, for the purpose of selecting the X-ray energies of the backlighters). In the first-generation CRASH simulations (performed by Tim Handy and published by Malamud *et al.* [42]), the laser energy was scaled to fit shock front position measurements from previous experiments at high-Atwood-number. The physical justification for the this laser-energy scaling is discussed in Section 6.4.1. Additionally, the initial perturbation amplitude in 2D CRASH simulations of the preliminary design ($a = 4\,\mu$m) is a factor of two larger than that of the final target design ($a = 2\,\mu$m). After the ablators delivered for the first two shot days failed to meet specifications, the perturbation amplitude was subsequently reduced in order to improve the fabrication quality, discussed in Section 5.4.3. New CRASH simulations were performed by Rachel Young and Matt Trantham, using the final target design parameters, actual densities (as reported by the manufacturers) for the ablator and foam materials, and the laser-energy tuned to fit the low-Atwood-number experimental

data. The new simulation results are presented in Section 6.4.1.

5.3 Physics-Based Design Considerations

To achieve the experimental goals, the design must:

- Create a blast wave whose acceleration/deceleration profile at the interface $g(t)$ maximizes RTI growth and does not bring the system into a regime where RMI growth dominates. The 1D dynamics of the blast wave formation are discussed in Section 5.3.1.

- Ensure that wall interactions do not affect the mixing dynamics near the central axis of the shock tube throughout the duration of the experiment. This is discussed in Section 5.3.2.

- Provide sufficient X-ray transmission and opacity contrast for radiography of the mixed-fluid region. This is discussed in Section 5.3.3.

- Ensure that preheat does not significantly affect the interface dynamics. Preheat refers to energy deposited in the target in advance of the shock wave, either by X-ray photons (emitted from the ablator when it is heated by the laser) or suprathermal electrons generated by laser-plasma interactions [114]. From CRASH simulations of the experimental design, Tim Handy and Guy Malamud concluded that the effects of preheat are negligible. This analysis is described in a journal publication about the experimental design [42].

5.3.1 Blast-Wave Dynamics

The essential dynamics of the blast-wave-driven system are as follows:

1. Intense UV laser beams ($> 10^{14}$ W/cm^2 in a 1 ns pulse) irradiate the front surface of the plastic ablator, creating a plasma which expands outward. Below

the critical density, laser light is absorbed. Heat transport by electrons then carries energy into a region of higher density. The material ablates outward, and in reaction to the ablation pressure, a shock wave is launched forward. Figure 5.3 (reproduced from [1] by R.P. Drake) shows the electron density profile and the regions where these physical processes occur.

2. When the laser pulse ends, a rarefaction forms at the front surface of the ablator. The head of the rarefaction wave travels faster than the shock front. When the rarefaction wave overtakes the shock wave, a blast wave is formed. The thickness of the ablator must be optimized so that the rarefaction wave catches up to the shock front just prior to breakout at the plastic-foam interface. A 1D Hyades simulation of the experimental design shows the formation of the blast wave in the ablator (Figure 5.4).

3. As the shock front crosses the rippled interface and travels from a denser material into a less-dense material, there is a brief phase of RMI growth, during which the initial perturbation amplitude is compressed, inverted, and then increases. This process is illustrated conceptually in Figure 5.5. In the early growth stage of RMI, the amplitude increases linearly with time (Equation 1.32).

4. The blast wave travels forward in the foam. On the foam-side, mass piles up behind the shock front, which decelerates the flow in the plastic and creates a weak reverse shock. At the interface, the pressure on the foam-side exceeds the pressure on the plastic-side ($\nabla p \cdot \nabla \rho < 0$), establishing the conditions necessary to drive RTI growth. Figure 5.6 shows the density and pressure profiles across the interface at $t = 4$ ns, approximately 1.5 ns after shock breakout.

5. As the blast wave continues to travel in the foam and sweep up mass, the interface continues to slow down (shown in Figure 5.7). When the blast wave has swept up a mass of foam equal to the total mass of the plastic ablator, the deceleration

at the interface, and consequently RTI growth, are negligible. However, the materials continue to decompress and the mixed-layer width increases due to the material expansion.

6. Although the materials decompress, the post-shock Atwood number across the interface remains nearly constant. CRASH simulations implement a more realistic EOS (as compared to Hyades) and more accurately predict the material properties and Atwood number. Preliminary 1D CRASH simulations predicted post-shock Atwood number $A \simeq 0.15$, shown in Figure 5.8.

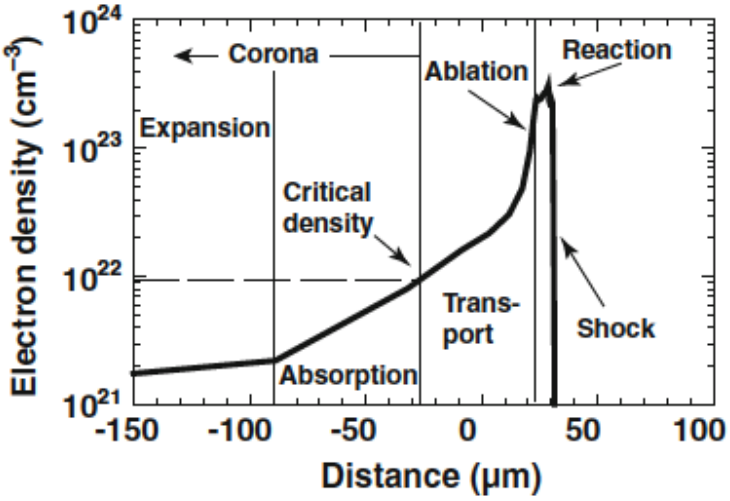

Figure 5.3: This figure by R.P. Drake shows the electron density profile from a computer simulation of a similar system (laser wavelength $\lambda_L = 0.35\,\mu$m and intensity $I_L = 10^{15}$ W/cm^2) and the regions corresponding to expansion, absorption of laser energy, electron heat transport, ablation, and the shock launched forward in reaction to the ablation pressure. (Figure 9.7 from [1])

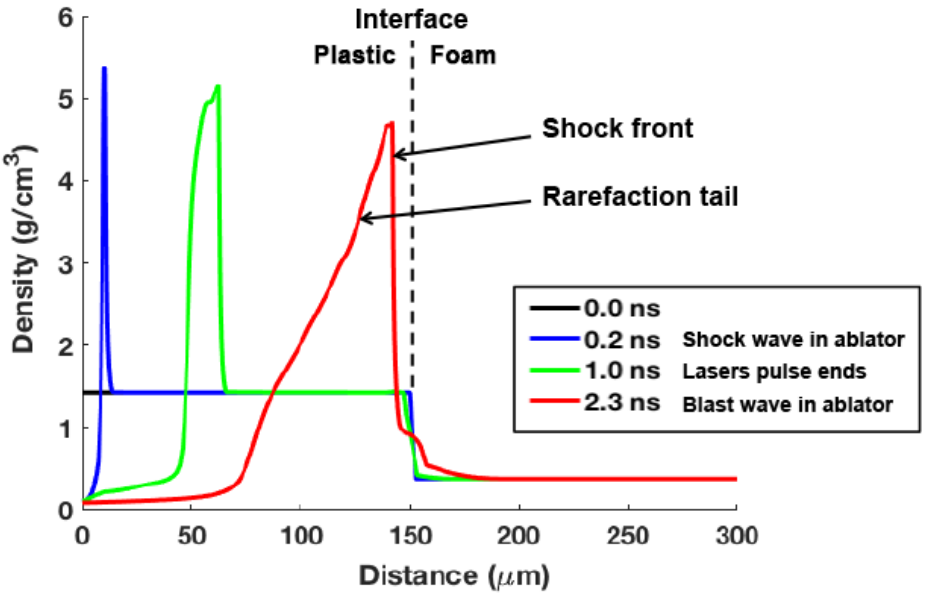

Figure 5.4: 1D dynamics of blast wave formation, illustrated by a time-series of density profiles ($\rho(x)$) from a Hyades simulation. The laser pulse ends at 1 ns and blast wave forms in ablator prior to shock breakout at interface ($t = 2.7$ ns).

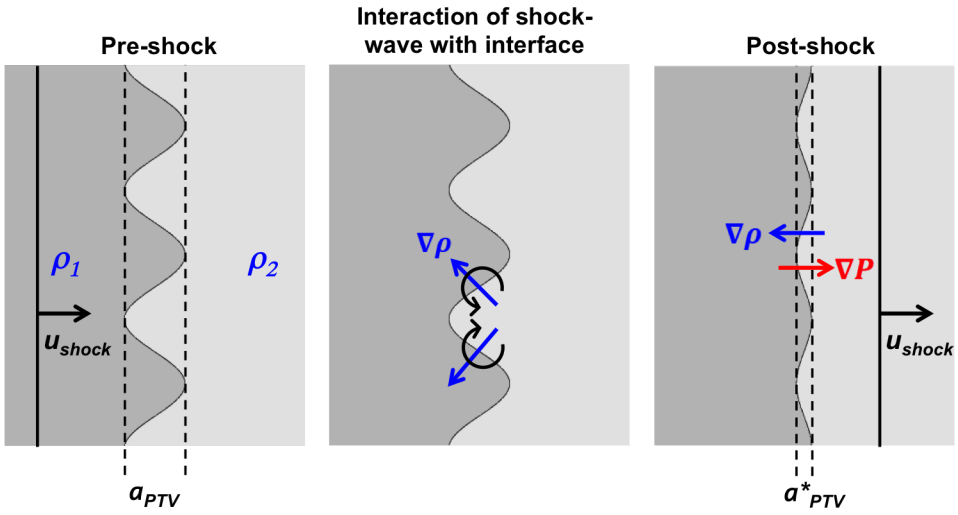

Figure 5.5: Conceptual illustration of the interaction of the shock wave with the rippled interface. When the shock wave travels from a denser material into a less-dense material, the initial perturbation amplitude is compressed and inverted.

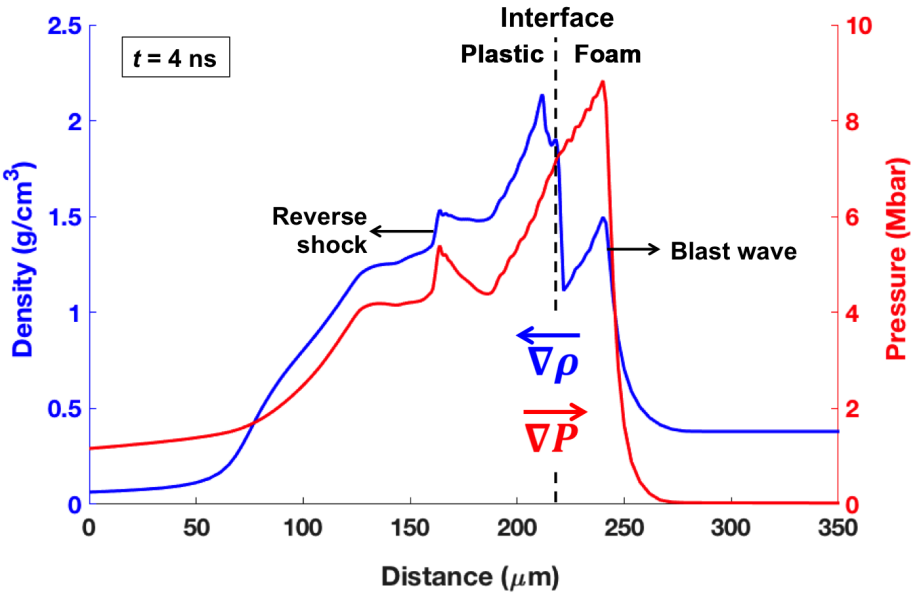

Figure 5.6: Shortly after shock-breakout, the density on the foam-side of the interface exceeds the density on the plastic-side. A weak reverse shock travels backward in the plastic. The interface decelerates and drives RTI growth. Density (blue) and pressure (red) profiles from a 1D Hyades simulation at $t = 4$ ns (approximately 1.5 ns after shock breakout) illustrate this stage of the experiment.

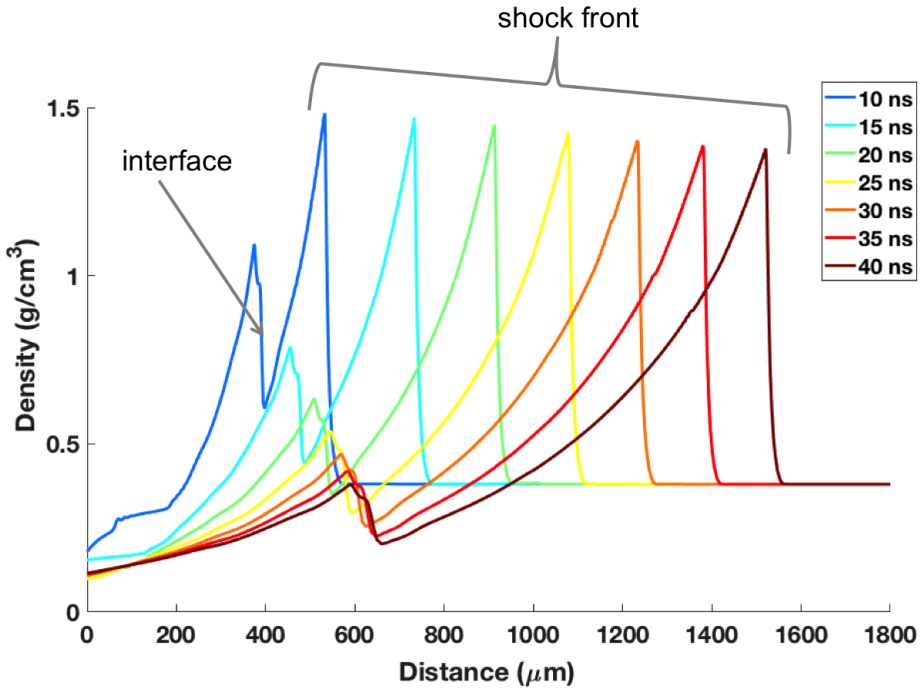

Figure 5.7: As the blast wave continues to travel in the foam, it slows down, illustrated by a time-series of density profiles from a 1D Hyades simulation from early to late times (10-40 ns).

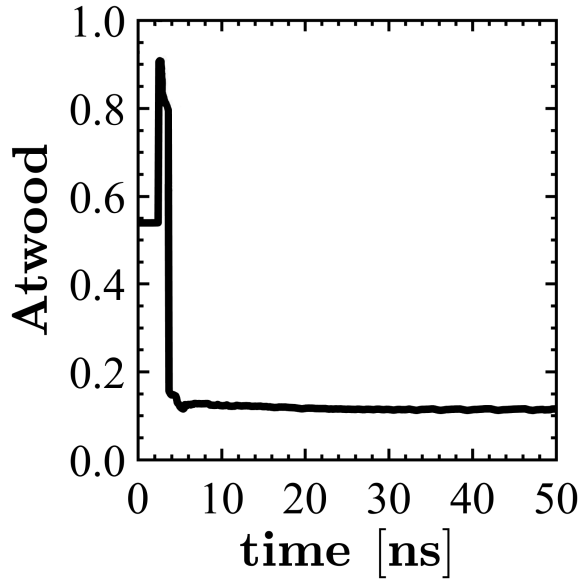

Figure 5.8: The post-shock Atwood number remains almost constant throughout the duration of the experiment. The Atwood number $A(t)$ is evaluated using the peak density in the ablator $\rho_1(t)$ and the minimum density in the shocked foam $\rho_2(t)$. 2D CRASH simulations by Tim Handy predicted post-shock Atwood number $A \approx 0.15$ [42].

5.3.2 Wall Interactions

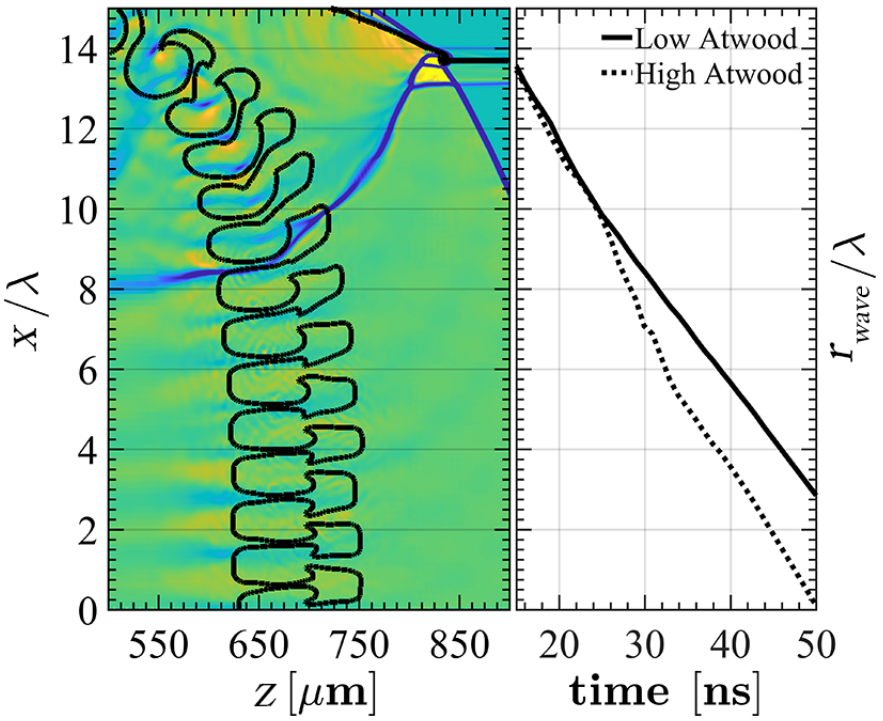

Figure 5.9: 2D CRASH simulations by Tim Handy predicted the interaction of the shock wave with the tube wall [42]. Left: Divergence of the velocity field ($\nabla \cdot \boldsymbol{u}$) for the low-A design at 30 ns, demonstrating transverse waves propagating towards the center of the tube ($x = 0$). The color map denotes compression (orange) and expansion (blue) about zero (green). Black contours identify the RT-unstable interface. Right: Radial position of the transverse wavefront versus time, for both low- and high-A designs. The transverse distance scale is normalized to the perturbation wavelength in both left (x/λ) and right (r/λ) figures.

The interaction of the shock wave with the tube wall creates a triple-point, from which an acoustic wave travels radially inward towards the center of the tube. We must predict the trajectory of this acoustic wave and ensure that it does not affect RTI growth and the mixing dynamics within the central region of the target where the tracer strip is located. Analysis of the preliminary CRASH simulation data indicated that the cross-sectional area of the target needed to be increased (from the original cylidrical tube design) in order to delay the interaction of the transverse waves with

RT spikes and bubbles in the tracer strip region at the latest observation times. The inner diameter of the shock tube was increased from the 900 to 1100 μm in the final design, shown in Section 5.4. The gold base (Figure 5.11) also serves as a "shock blocker" to reduce the strength of the shock in the tube walls.

5.3.3 Radiography Contrast

To select the backlighter source which provides the best opacity contrast, I calculated the net transmission through the target (along each radiography axis) as a function of X-ray energy at axial positions corresponding to the peak density in the ablator (spike front), the minimum density in the post-shocked foam (bubble front), and either side of the shock front in the foam. To estimate the time-varying densities in the ablator and foam, I used density profiles from 1D Hyades simulations from early to late times (10-40 ns), shown in Figure 5.7. Using the known atomic composition and thickness of each material layer (along the radiography axis), I calculated the net X-ray transmission through the target:

$$T_x(E) = \exp\Big(- \sum_j \kappa_j \, \rho_j \, l_j \Big) \tag{5.1}$$

where $\kappa_j(E)$ is the mass-attenuation coefficient at X-ray photon energy E, ρ_j is the mass-density, and l_j is the thickness of each material layer j. Target materials included the Beryllium shock tube, PAI ablator, CHI tracer strip, and CRF foam (Figure 5.11). Mass-attenuation coefficients were obtained from a Matlab script originally published by Jarek Tuszynski, which includes values reported by the National Institute of Standards and Technology (NIST) [115]. Figure 5.10 shows the result of these calculations along the primary and secondary radiography axes at 10 ns and 30 ns. Vertical lines indicate X-ray energies emitted by commonly used backlighter materials (Fe, Ni, Zn). From these plots, I determined that Ni (7.8 keV) provides the best overall

opacity contrast at the spike, bubble, and shock fronts.

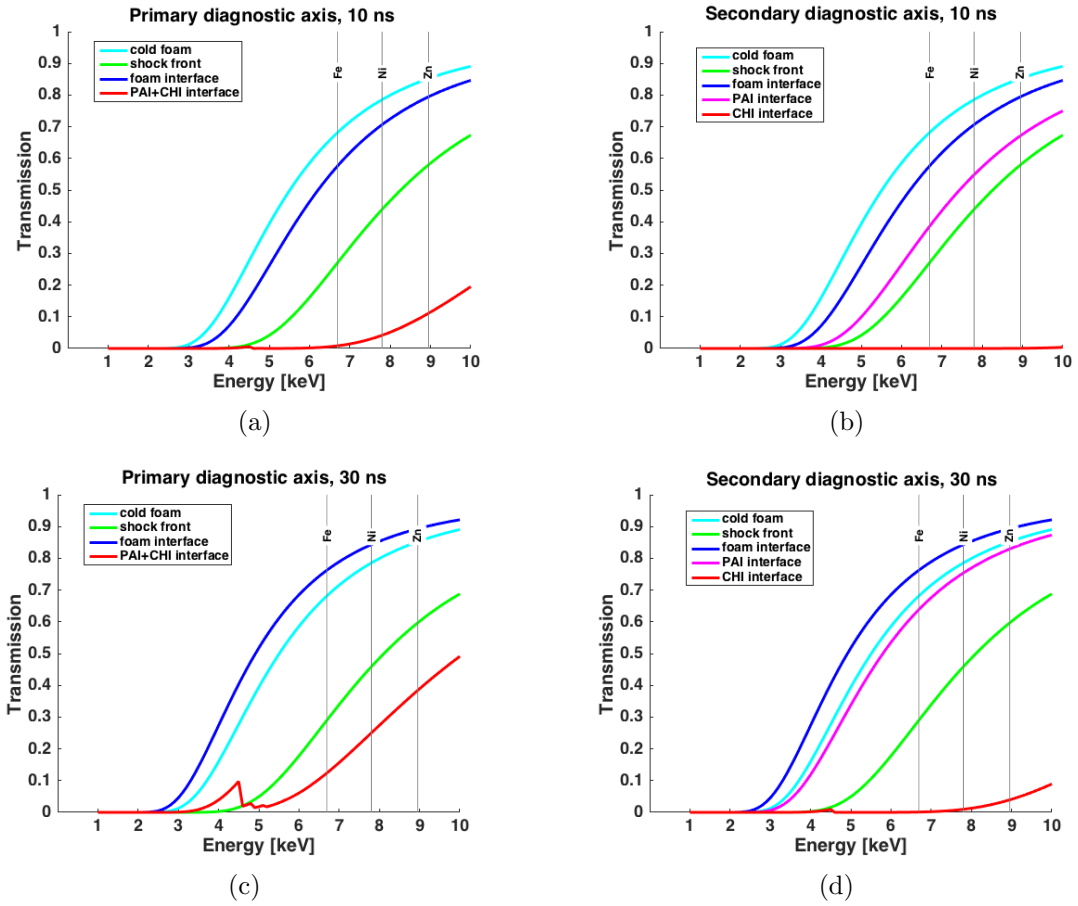

Figure 5.10: Net transmission in different regions of the target as a function of X-ray energy: (a) Primary radiography axis at 10 ns; (b) Secondary radiography axis at 10 ns; (c) Primary radiography axis at 30 ns; (d) Secondary radiography axis at 30 ns. Vertical lines correspond to the energies emitted by three potential backlighter materials (Fe, Ni, Zn).

5.4 Main Target

5.4.1 Physics Package

Critical components (shown in Figure 5.11) include the polyamide-imide, $C_{22}H_{14}N_2O_4$ (PAI) ablator, Iodine-doped polystyrene, $C_{50}H_{47}I_3$ (CHI) tracer strip, carbonized resorcinol-formaldehyde (CRF) foam, Beryllium shock tube, and gold base, which is coated with polyimide, $C_{22}H_{10}N_2O_5$ (PI) on the driven side. The ablator is 150

μm thick with a cross-sectional area of 1100 x 1100 μm^2. The tracer strip enhances radiography contrast of the RT spikes and bubbles near the central axis of the shock-tube, where the drive pressure is uniform and the flow is unaffected by interaction with the walls. The CHI material is density-matched (and assumed to be hydrodynamically equivalent) to the surrounding PAI material, but more opaque in the X-ray spectrum used for radiography. The tracer strip measures 240 μm wide x 1100 μm long x 80 μm thick. The CRF foam (1100 μm $\times$ 1100 μm $\times$ 3000 μm) fills the entire shock-tube, from the ablator interface to the open end of the tube. At the latest observational time, the shock front will have traveled approximately half the length of the tube.

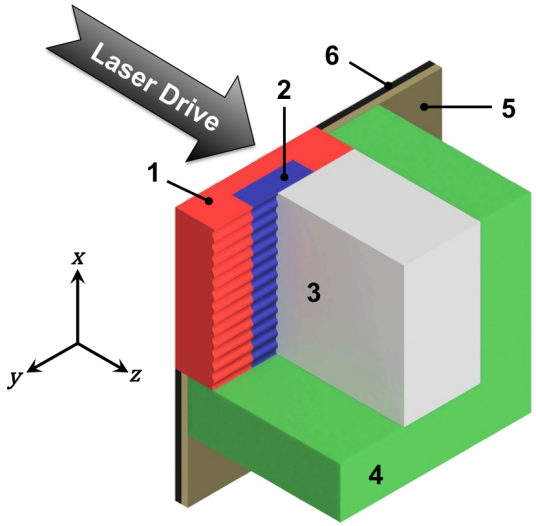

No.	Component	Material	Density (g/cm^3)
1	Ablator	PAI ($C_{22}H_{14}N_2O_4$)	1.43
2	Tracer strip	CHI ($C_{50}H_{47}I_3$)	1.43
3	Foam	CRF ($C_{1000}O_{48}H_{65}$)	0.38
4	Shock-tube	Beryllium (Be)	1.85
5	Base	Gold (Au)	19.3
6	Coating	PI ($C_{22}H_{10}N_2O_5$)	1.4

Figure 5.11: Critical target components and materials (modified from a figure by Tim Handy [42]). For illustrative purposes, the front half of the foam, as well as the front and top sides of the base and shock tube walls, have been clipped to reveal interior features.

5.4.2 Mechanical Design and Shielding

The shock tube consists of four discrete Beryllium walls, each 200 μm thick. The shock tube is mounted on a 25 μm-thick gold base with an additional 25 μm-thick polyimide coating on the laser-irradiated side. A square hole in the center of the base exposes the ablator surface to the laser drive. The entire physics package is mounted inside a large acrylic cone (Figure 5.12). On the outside of the cone, a 50 μm-thick gold foil shields detectors from the laser drive beams and secondary X-ray emission at the drive surface. On the two exterior shock tube walls facing the detectors, fiducial grids (64 μm pitch) provide absolute spatial references for radiography measurements.

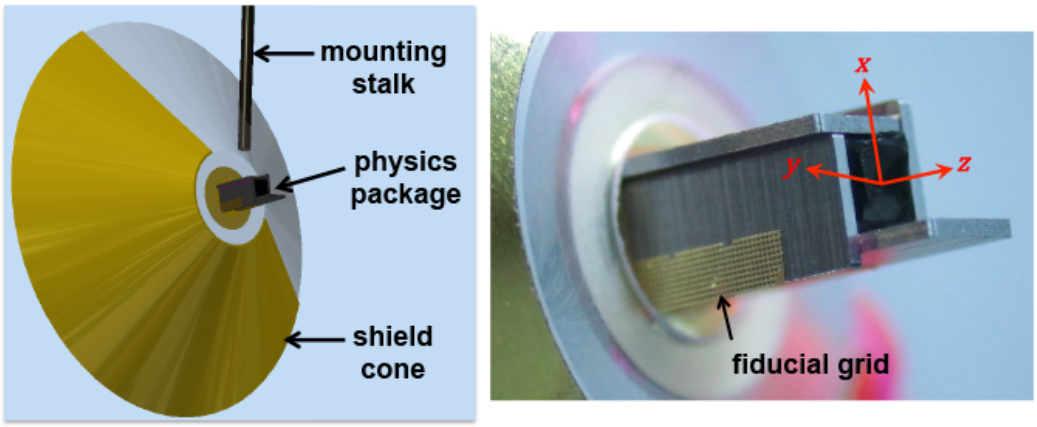

Figure 5.12: Complete target assembly. Left: CAD model by Sallee Klein. Right: metrology photo of an actual target. The longer bottom wall of the shock tube serves as a reticle for positioning and alignment inside the target chamber.

5.4.3 Seed Perturbation Pattern

There are three target variations: perturbed-interface targets with 2D or 3D single-mode sinusoidal ripple patterns (Equation 5.2) and flat-interface targets. Single-mode RTI growth is seeded with perturbation wavelength $\lambda = 40\,\mu$m and amplitude $a = 2\,\mu$m. For the 3D pattern, we use a sum-of-cosines function similar to the

numerical simulations of Ramaprabhu *et al.* [49] and the gas-phase rarefaction-driven experiments of Morgan *et al.* [76]. The peak-to-valley amplitude $a_{\mathrm{PTV}} = 2a = 4\,\mu$m is the same for 2D and 3D perturbation patterns.

$$\begin{aligned} &\text{2D target: } \Delta z(x) = a\cos(\frac{2\pi}{\lambda}x) \\ &\text{3D target: } \Delta z(x,y) = \frac{a}{2}\left(\cos(\frac{2\pi}{\lambda}x) + \cos(\frac{2\pi}{\lambda}y)\right) \end{aligned} \tag{5.2}$$

To reach the nonlinear growth stage as early as possible (in terms of non-dimensional time, τ), we desire a short-wavelength seed perturbation (Equation 2.17). This consideration is balanced with spatial resolution requirements of the imaging system, discussed in Section 5.6. The fabrication methods also influence the choice of wavelength and initial amplitude. The process must write a uniform pattern across the composite surface of the ablator (PAI and CHI materials). Lithography is ill-suited to this application. Best results are achieved with micro-machining by diamond-turning lathe; however, tool-tip clearance limits the aspect ratio to $a/\lambda \leq 0.1$ for an ideal sine-wave. At larger aspect ratios, the pattern shape becomes scalloped or saw-tooth, introducing asymmetry which could affect the evolution of RTI [98]. The ablator fabrication process involves the following steps:

1. The PAI material is machined to size ($1100\,\mu\text{m} \times 1100\,\mu\text{m} \times 150\,\mu\text{m}$ thick)
2. The bottom surface of the PAI is polished flat (this becomes the drive surface)
3. On the top surface of the PAI, a notch is milled out for the tracer strip
4. The CHI material is cut to size ($240\,\mu\text{m} \times 1100\,\mu\text{m} \times 80\,\mu\text{m}$ thick) and inserted into the notch in the PAI. A thin layer ($< 3\,\mu$m) of adhesive bonds the two parts
5. The perturbation pattern is machined on the composite PAI-CHI surface using a diamond-turning lathe. (Or in the case of the flat-interface targets, the surface is polished to $\leq 1\,\mu$m roughness)

6. The 3D topology of the patterned surface is measured using a white-light interferometer (WLI) (Figure 5.13)

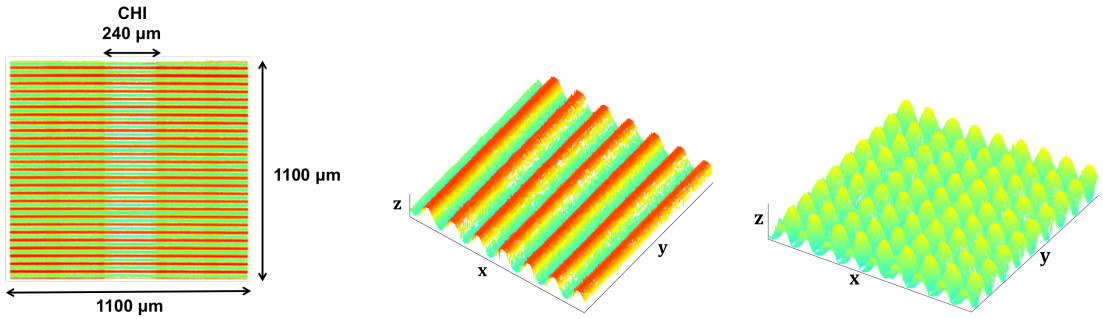

Figure 5.13: Color-map visualization of white-light interferometer scans of ablator surfaces (actual parts). Left: top view of entire part with 2D pattern. Center: close-up, perspective view of 2D pattern. Right: close-up, perspective view of 3D pattern.

The CRF foam is machined to the shape of a rectangular prism with the interior dimensions of the shock tube ($1100\,\mu$m $\times$ $1100\,\mu$m $\times$ $3000\,\mu$m). The surface in contact with the ablator is flat, due to the increased difficulty and expense required to machine the foam to match the ablator. Numerous experiments at high-Atwood-number ($\rho_2 = 0.04 - 0.1\,\mathrm{g/cm^3}$) have claimed equivalence of targets with a rippled ablator abutted to flat foam and targets with the foam match-machined to the ablator ripple pattern [116] [107] [113].

5.5 Laser Drive

At Omega-60, ten laser beams ($\lambda_{laser} = 351$ nm) focus onto the planar surface of the ablator and deliver a total energy of 4.5 kJ in a 1 ns pulse.[1] Each of these beam paths utilizes 2D-SSD (smoothing by spectral dispersion) and eighth-order super-Gaussian phase plates. Visrad is a computer model of the laser target chambers at Omega and NIF, which is used to specify the experimental configuration, including

[1]Due to the arrangement of laser beam ports at Omega-60, only 10 of the 60 beams can be pointed to $\leq 50^o$ from normal incidence of a planar surface.

laser beam parameters (energy, pointing, focus), CAD model of target components and their positions within the chamber, and pointing of diagnostics. The program also simulates laser energy deposition on target surfaces and thermal radiation transfer. For the combined laser irradiance, Visrad predicts a circular laser spot with peak irradiance $I_0 = 700\,\mathrm{TW/cm^2}$ at the center of the ablator with FWHM = $880\,\mu$m and 97% of the total laser power incident on the surface of the ablator (Figure 5.14). In 2D CRASH simulations, the laser spot is modeled as a super-Gaussian function fit to the Visrad laser spot profile: $I(x) = I_0 \exp\left(-(x^2/2r^2)^q\right)$, with $r = 345\,\mu$m, q=2.

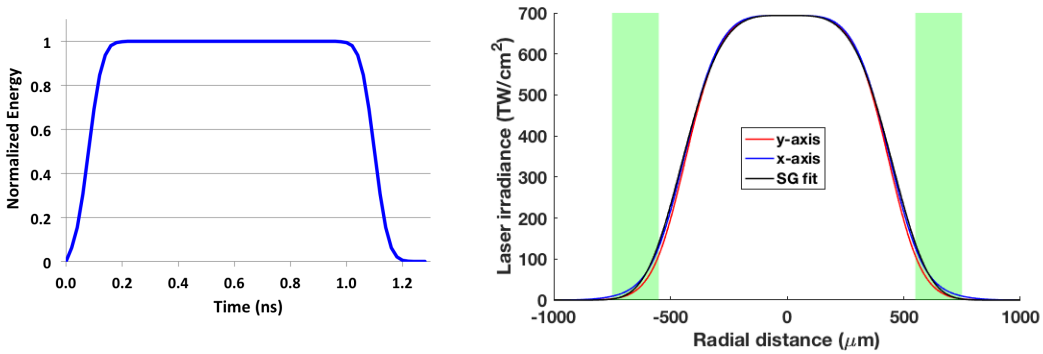

Figure 5.14: Laser Drive. Left: Temporal pulse shape of laser drive. Right: Spatial profile of laser irradiance on target from Visrad model with line-outs along the y-axis (red curve) and x-axis (blue curve) and super-Gaussian fit (black curve). The green-shaded regions indicate the area beneath the shock tube walls.

5.6 Radiography Diagnostics

The primary radiography axis (along the y-direction) integrates across the narrow dimension of the tracer strip, enabling measurement of shock-, spike-, and bubble-front positions near the central axis of the shock tube (Figure 5.15, left). The secondary radiography axis (along the x-direction) integrates across the wide dimension of the tracer strip (Figure 5.15, right). In this view, we can obtain measurements of shock- and spike-front positions, but the fully opaque tracer strip obscures the bubble-front.

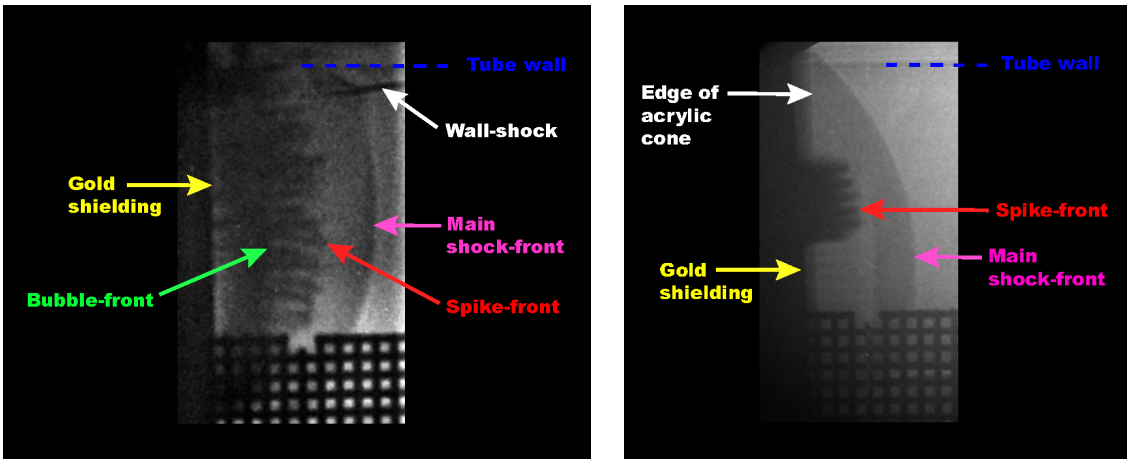

Figure 5.15: Radiography examples in primary and secondary views, both of 3D targets at 20 ns. Left: RID90385 (primary radiography axis). Right: RID90387 (secondary radiography axis). Images have been cropped and filtered to enhance contrast. Fiducial grid pitch is 64 μm/square in each linear dimension.

5.6.1 Point-Projection Pinhole Imager

Along each radiography axis, a point-projection pinhole backlighter provides the X-ray source and imaging system (Figure 5.16). Spatial resolution at the image plane is determined by the pinhole diameter, D. Similar experiments at high-Atwood-number involved longer perturbation wavelengths and less-dense (more transparent) foam materials. This imposed less stringent requirements for spatial resolution and permitted lower-energy backlighter sources ($\sim$ 4-5 keV, emitted by materials such as Ti, Sc, V). For this low-Atwood-number design with perturbation wavelength $\lambda = 40\,\mu$m, we require spatial resolution of $\pm 5\,\mu$m ($D = 10\,\mu$m). Because the X-ray source flux scales in proportion to D^2, a smaller diameter pinhole greatly reduces the signal strength. Additionally, the denser foam necessitates a high-photon-energy source, generated from a higher-atomic-number material, with significantly lower X-ray photon conversion efficiency [117].

Therefore, signal-to-noise ratio (SNR) was a challenge for this experiment. After post-processing the raw radiography data, image contrast was sufficient to measure shock-, spike-, and bubble-front positions. However, the signal dynamic range was too

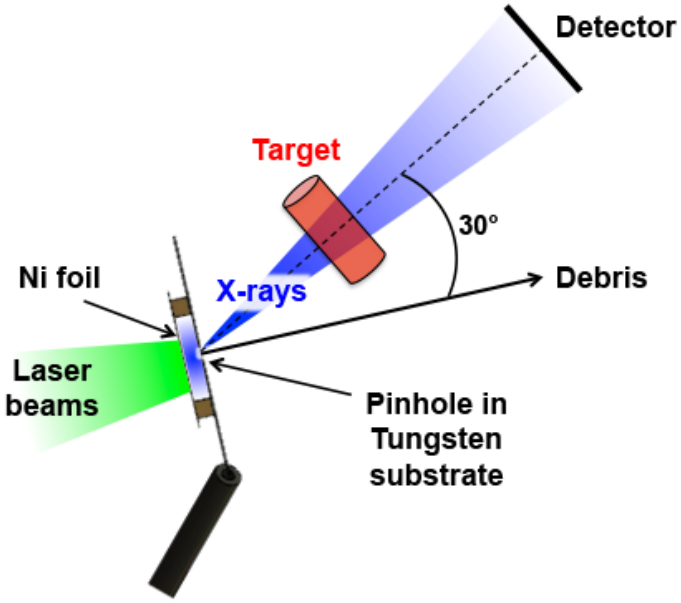

Imaging system properties:	
Source to object distance:	11.5 mm
Object to image distance:	228.6 mm
Magnification at image plane:	21x
Field-of-view (FOV) in object plane:	Ø1.85 mm

Figure 5.16: Conceptual illustration of point-projection pinhole imaging system. Along each radiography axis, the object plane is defined as the normal plane bisecting the target.

low for accurate measurements of densities. Post-shock densities and Atwood-number are calculated from numerical simulations calibrated to the experimental data.

5.6.2 Backlighter Targets

Each backlighter is driven by four Omega-60 laser beams (λ_{laser} = 351 nm, 1 ns pulse, 0.45 J/beam). These beams focus to a circular spot (1/e radius = 360 μm, peak irradiance = 4.5×10^{11} W/cm^2) on the surface of the Ni foil (4x4 mm^2 square, 5 μm thick), centered above the pinhole. The X-ray emission spectrum of Ni is strongly peaked at 7.8 keV, corresponding to Li+He-like K-shell transitions [118]. A point-source is created by a pinhole in a 7x7 mm^2 square, 50 μm-thick Tungsten substrate, positioned 500 μm behind the Ni foil. The foil is suspended above the substrate

with plastic stand-offs at the corners, outside the laser focal spot. The Ni foil emits isotropic X-ray radiation, which ablates the substrate and leads to pinhole closure. Often, backlighters are designed with a plastic tamper between the irradiated foil and pinhole substrate, which can reduce pinhole closure [119]. However, other studies have shown that hot-electron emission from the plastic generates hard-X-ray (> 10 keV) background noise, which cannot be filtered [120]. Since SNR is a primary concern, I elected not to use a plastic tamper. Instead, pinhole closure is mitigated by tapering from a larger entrance-hole diameter (irradiated side) to a smaller exit-hole diameter (target-facing side). I tested two taper designs with entrance-to-exit hole diameters of 50-20 and 20-10 μm. For the 50-20 μm design, I measured spatial resolution $D \approx 10\,\mu$m (which indicates partial pinhole closure). Appendix A explains the method used to measure the spatial resolution. In the experimental data presented in Chapter VI, both pinhole sizes were used. The larger pinhole yielded better results, with adequate spatial resolution and higher SNR (as compared to the smaller pinhole size).

After the pinhole substrate ablates, it begins to break apart, creating high-velocity shrapnel, which can damage the detectors [121]. For debris mitigation, the substrate normal is tilted 30 degrees off-axis from the diagnostic line-of-sight. The pinhole is laser-drilled at a 30 degree angle through the substrate, so that the pinhole axis is aligned with the radiography axis. Figure 5.17 shows the mechanical design of the backlighter target with the tapered pinhole.

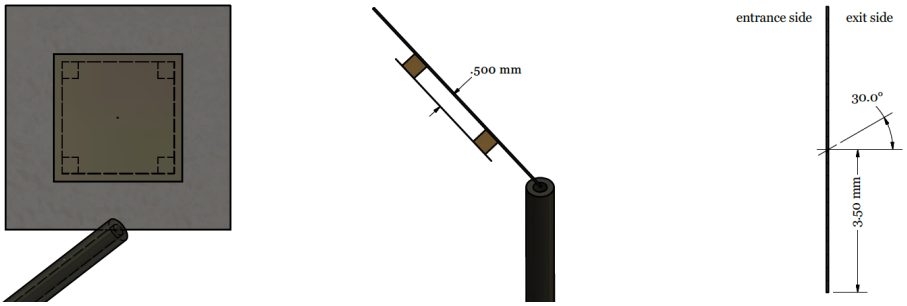

Figure 5.17: Backlighter mechanical design. CAD drawings from Sallee Klein. Left: top view of the backlighter target, showing the laser-irradiated surface of the Ni foil above the pinhole. Center: side-view of the complete backlighter target. Right: side-view of the pinhole substrate, showing the direction of tapered pinhole.

5.6.3 Detectors

In addition to the 60 target chamber ports for laser beam lines, there are numerous other ports dedicated for experimental diagnostics, target positioners, and various other monitors for operations. Many of these port positions are fixed. A limited set of diagnostics are mounted in the ten-inch manipulator (TIM) platform, which is compatible with multiple target chamber ports and may be extracted, reconfigured, and re-inserted between shots without opening the target chamber. For versatility, I used TIM-based diagnostics along two orthogonal lines of sight. The primary detector in each TIM is a single-strip X-ray framing camera (XRFC). As a contingency, the XRFC may be replaced with a film pack (consisting of two layers of Agfa D7 film [122] inside a light-tight 25 μm-thick black PI envelope). XRFCs have numerous advantages, including electronic triggering, temporal gating (0.2-0.5 ns), and in-situ read-out of image data available within one shot cycle. However, spectral responsivity and gain (a function of bias voltage and electronic pulse-forming module) are uncalibrated and differ significantly among individual cameras. Signal fidelity may be degraded by electronic noise and non-uniform gain across the detector area. Additionally, inconsistent performance between shot days (several months apart) should be expected at a user facility. Film has the advantage of consistent performance and higher signal

flux (at the expense of temporal resolution). The film is un-gated, so the signal is integrated over the backlighter pulse duration (1 ns). Unfortunately, the film is also exposed during the main laser drive. Shielding is provided by target mechanical design (main target cone and backlighter substrate), a nose cone in front the detector (Figure 5.18), and two filter packs (Table 5.1). The blast-shield filter at the front of the nose cone is inspected and, if necessary, replaced after each shot. The rear filter pack provides spectral filtering in the visible and soft-X-ray spectrum to improve SNR. Net signal transmission through the filter stack is 64% (Figure 5.19).

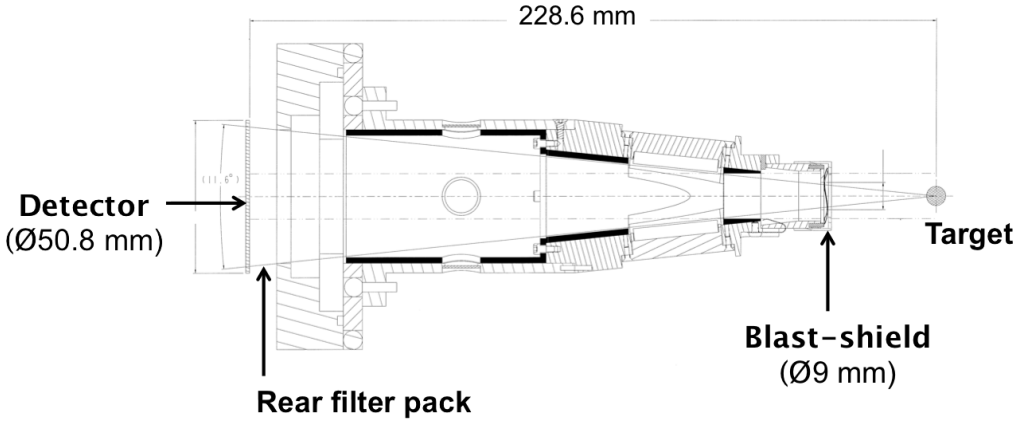

Figure 5.18: TIM-based diagnostic platform with 9 mm aperture nose cone, showing the location of the detector and two filter packs. Drawing provided by the Omega facility.

Blast shield	(target-facing) Polyimide (75 μm) Beryllium (500 μm)
Rear filters	Beryllium (250 μm) Ni (5 μm) (Detector-facing)

Table 5.1: Detector filter packs

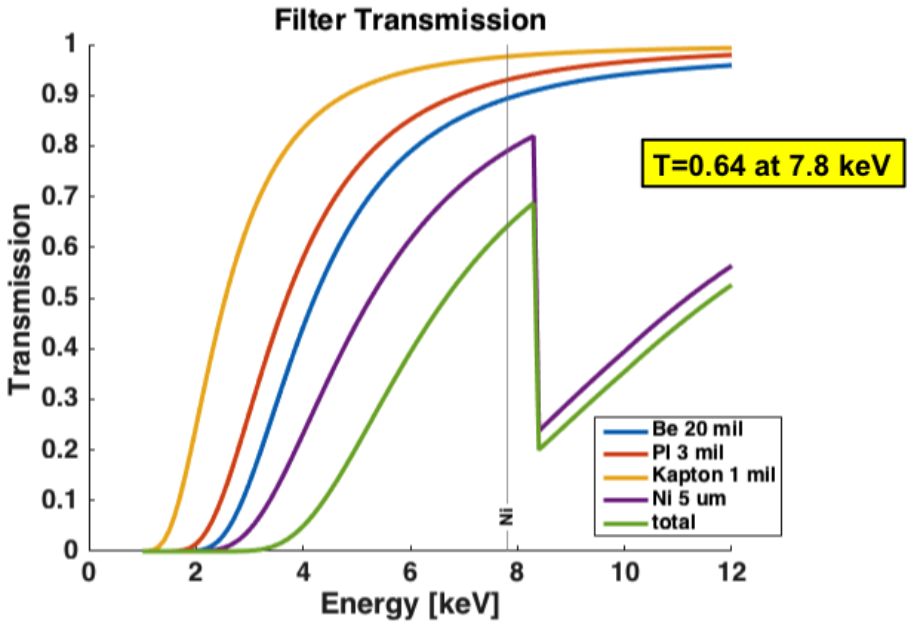

Figure 5.19: Backlighter signal transmission through the various filter components. The net transmission through the complete filter stack is 64%.

CHAPTER VI

Experimental Results

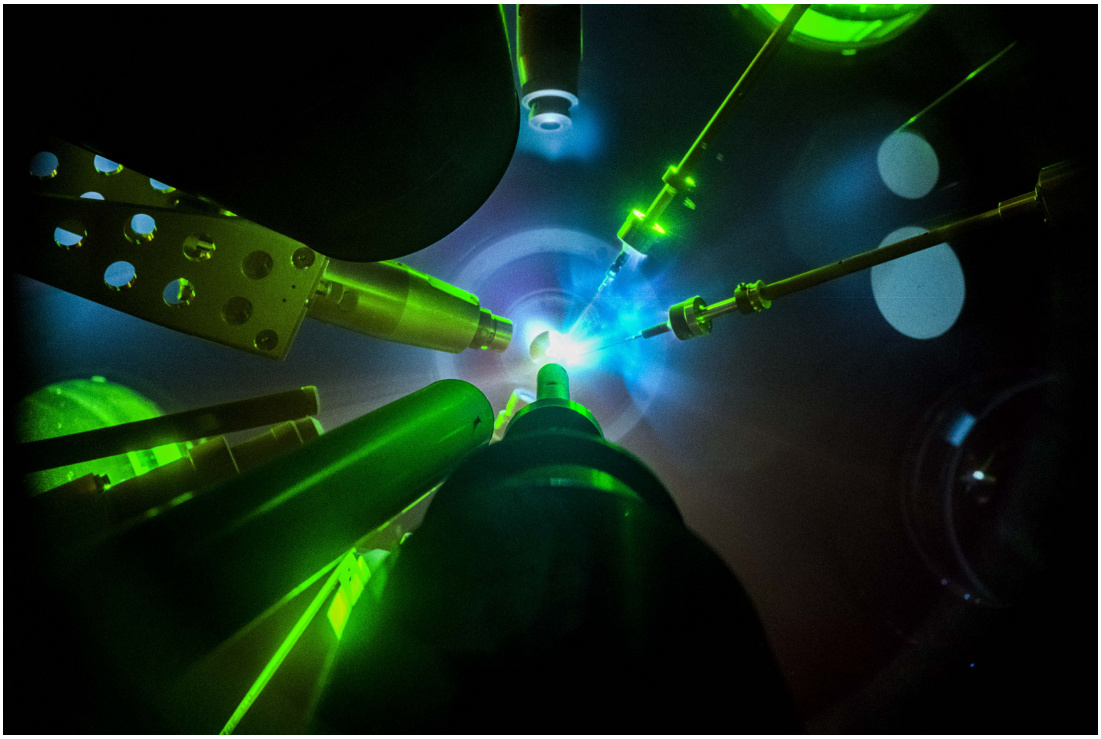

Figure 6.1: Lasers shooting a target at Omega-60: Visible Light Camera (Port P2) image of RID90385. Image provided by Eugene Kowaluk at LLE.

The data set includes measurements in both radiography views of 17 targets total from two shot days at Omega-60 (April 19 and July 18, 2018) with three target variations: 3D targets (Qty. 5), 2D targets (Qty. 9), flat targets (Qty. 3). We captured radiography images at a variety of times, measuring shock-front position

from 17-47 ns, spike-front position from 17-47 ns, and bubble-front position from 20-39 ns. At earlier times, the mixed-fluid region was obscured by the gold shielding on the target. In the secondary radiography view (which integrates through the wide dimension of the tracer strip), only shock- and spike-front positions can be measured due to the opacity contrast and low SNR. Therefore, the number of data points for spike-front position exceeds the number of data points for bubble-front position. For the flat targets, the spike front corresponds to the steepest intensity gradient at the CHI-foam interface (pink squares labeled "flat spike" in Figure 6.2). There are no "flat bubble" data points because gold shielding obscured the bubble front in the primary radiography view for the three flat targets shot.

Figure 6.2 shows three principal results, which will be discussed in turn:

1) There is large shot-to-shot variation in the data.

2) Power-law fits to data indicate that growth of mixed-fluid region is dominated by material decompression after 22 ns (the equal-mass time).

3) Contrary to expectations, there is no measurable difference in the data for 2D, 3D, and flat-interface targets.

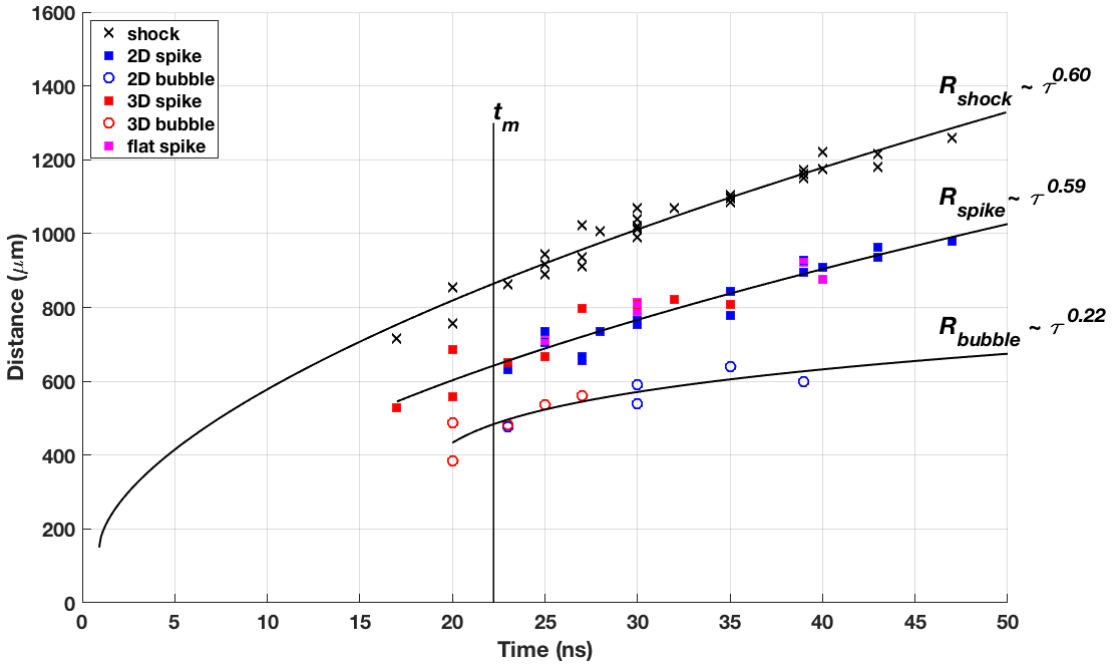

Figure 6.2: Experimentally measured shock-front, spike-front, and bubble-front positions versus time and power-law fits to the data. Distances measured relative to the drive surface of the ablator. For readability, error bars are not shown on individual data points. Systematic measurement errors (typical for all shots) are summarized in Table 6.1.

6.1 Shot-to-Shot variations in the Data

Systematic uncertainties include diagnostic resolution ($\pm 5\,\mu$m) and absolute position of the fiducial reference ($\pm 13\,\mu$m). Additional error may arise from motion-blurring caused by integration of signal intensity over the diagnostic gate time. As a conservative upper-estimate, this translates to +9/-0 μm in shock-front position and +7/-0 μm in spike- and bubble-front positions. In the temporal domain, uncertainty of the absolute timing of the backlighter beams relative to the main drive beams is (at most) ± 0.2 ns. Ablation pressure (P_{abl}) scales with laser intensity (I_L) and shock velocity (u_{sh}) as: $P_{abl} \sim I_L^{2/3}$ and $P_{abl} \sim u_{sh}^2 \rightarrow u_{sh} \sim I_L^{1/3}$ [1]. Intensity of the laser drive varied by less than 10%, which results in $\leq 3\%$ variation in initial shock velocity, and no significant difference in shock-front position at later times.

Table 6.1 summarizes the maximum systematic error expected in the experimental

data. Of note, the shot-to-shot variation in the data is a factor of two larger than the systematic measurement error. For example, Table 6.2 compares measurements at 20 ns of two nominally identical 3D targets (RIDs 90385, 90387, shown in Figure 5.15). For the entire data set, the shot-to-shot variation in measured position (shock-, spike- and bubble-fronts) appears comparable to (and in many cases, smaller than) published results of similar blast-wave-driven experiments at high-Atwood-number ([110] [107] [106] [96], among others).

Measurement	Error (μm)
Shock-front position:	+27/-18 (range 45)
Spike-front position:	+25/-18 (range 43)
Bubble-front position:	+25/-18 (range 43)

Table 6.1: Total systematic measurement error

Position (μm):	Shock	Spike	Bubble
RID 90385:	853	685	488
RID 90387:	757	558	385
range (μm):	96	127	103

Table 6.2: Shot-to-shot variation in measurements of 3D targets at 20 ns

Shot-to-shot variations in excess of systematic measurement error result from differences in target construction and positioning/alignment inside the target chamber. Pre-shot metrology of components and fully-assembled targets revealed irregularities in target materials and fabrication (see Appendix B for details). These internal target defects may have seeded RTI growth with uncontrolled initial conditions or modify the shock velocity in the foam. Target misalignment manifests as asymmetry in the radiography data. Ideally, peak laser irradiance occurs at the center of the ablator and a normal-incidence shock wave is driven into the target. In both radiography views, we expect the target interior to exhibit mirror symmetry about the central axis of the shock tube. In 7 out of 17 shots, we observed asymmetry in the radiography data characteristic of target misalignment. An extreme example is shown in Figure 6.3. For all shots, shock, spike, and bubble positions were measured along a line through

the vertex of the curved front (which may or may not coincide with the central axis of the shock tube). Two types of target misalignment are possible: translational and

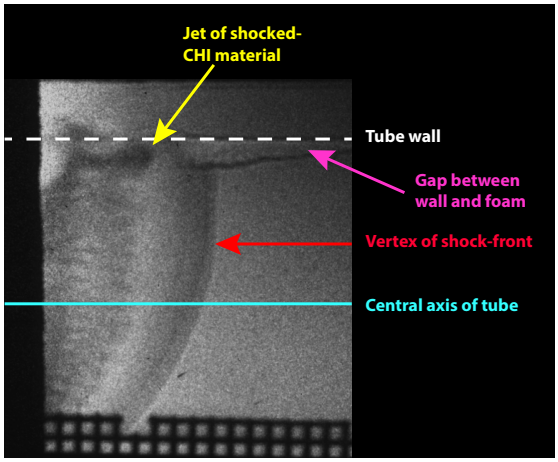

Figure 6.3: Example of target with translational misalignment and gap between the foam and upper shock-tube wall. (RID89390, 2D target at 35 ns.) The vertex of the shock-front is located 200 μm above the central axis of the tube. A jet of shocked-CHI material extends into the wall-gap.

rotational. In the former case, the target is translated in the xy plane. Peak laser irradiance is displaced from the center of the ablator, but a normal-incidence shock is still driven into the target. Interaction with the shock-tube wall occurs earlier in time, both because the region-of-interest is located closer to the wall and because a stronger shock is driven into the wall, and alters the mixing dynamics. Additionally, if there existed a gap between the foam and the tube wall (which was the case for some targets, observed in metrology at the target-assembly level), shocked-plastic material would jet into the gap and affect measurement of spike-front position in the secondary radiography view. For these shots, this data was excluded from the measurement set. In the case of rotational misalignment, the peak laser irradiance occurs at the center of the ablator, but the drive surface is tilted, launching an oblique shock into the target. The effect of rotational misalignment is to decrease the normal component of the shock velocity and increase vorticity deposition at the interface, which could significantly alter the mixing dynamics.

6.2 Power-Law Fits to Shock, Spike, and Bubble Positions and Calculation of the Equal-Mass Time

The shock-front trajectory in the foam should fit a power-law function, characteristic of the self-similar evolution of a blast wave [123]:

$$R_{shock}(t) = R_0\,\tau^{\alpha} + R_0, \text{ where } \tau = \frac{t - t_0}{t_s - t_0} \tag{6.1}$$

$R_0 = 150\ \mu$m is the ablator thickness, which is the initial interface position relative the drive surface. The shock breakout time, $t_s = 2.5$ ns, is when the shock front reaches the ablator-foam interface. This value of t_s is provided by 2D flat-interface CRASH simulations tuned to the experimental data (discussed in Section 6.4.1). A nonlinear regression fit to the shock-front position data, constrained by R_0 and t_s, gives exponent $\alpha = 0.60$ and $t_0 = 0.91$ ns. The shift in temporal origin, t_0, accounts for uncertainty in the shock breakout time and the different temporal dynamics during the brief interval as the shock front crosses the material interface (Richtmyer-Meskhkov phase). The actual value of t_0 has no physical significance.

The characteristic length scale is the equal-mass distance, R_m, which is the distance traveled by the blast wave in the foam when it has swept up mass equal to the total mass of the plastic ablator. This can be readily calculated: $\rho_1 R_0 = \rho_2(R_m - R_0)$, where $\rho_1 = 1.43$, $\rho_2 = 0.38$ g/cm^3 are the initial densities of the plastic and foam, respectively. Note that here, $R_m = 714\,\mu$m is the distance traveled within the foam, so that the distance relative to the drive surface (plotted in Figure 6.2) is $R_m + R_0 = 864\,\mu$m. Solving Equation 6.1 for $R_{shock}(t = t_m) = 864\ \mu$m gives the equal-mass time, $t_m = 22$ ns.

After the equal-mass time, we expect deceleration at the interface to rapidly decay. For $t > t_m$, growth of the mixed-fluid region is dominated by material decompression and the contribution from RTI is small. Using the equal-mass time as a constraint, I fit

power-law functions to the experimentally measured spike- and bubble-front positions:

$$R_{spike}(t) = R_1\,\tau_1^{\alpha_1} + R_0, \text{ where } \tau_1 = \frac{t - t_1}{t_m - t_1} \tag{6.2a}$$

$$R_{bubble}(t) = R_2\,\tau_2^{\alpha_2} + R_0, \text{ where } \tau_2 = \frac{t - t_2}{t_m - t_2} \tag{6.2b}$$

For spikes, the data set includes 3D, 2D, and flat targets, yielding $\alpha_1 = 0.59$, $R_1 = 492\,\mu$m, $t_1 = 5.46$ ns. For bubbles, the data set includes 3D and 2D targets, yielding $\alpha_2 = 0.22$, $R_2 = 334\,\mu$m, $t_2 = 17.93$ ns.

6.2.1 Amplitude-Compression During Shock Transit

As the shock-wave crosses the interface, there is a brief stage of Richtmyer-Meshkov instability growth, during which the peak-to-valley amplitude of the initial perturbation, $a_{\rm PTV}$, is inverted and compressed to a post-shock amplitude, a^*_{PTV}, where $|a^*_{\rm PTV}| < |a_{\rm PTV}|$ (conceptually illustrated in Figure 5.5). For my sign convention, $a_{PTV} = 4\,\mu$m > 0 and $a^*_{\rm PTV} < 0$.

In similar experiments at high-Atwood-number by Drake [110], initial shock velocities in the plastic (u_{sh1}) and foam (u_{sh2}) and the shock transit time across the interface (Δt) were estimated as:

$$u_{sh1} \simeq \frac{R_0}{t_s} \tag{6.3}$$

$$u_{sh2} \simeq \dot{R}_{shock}\Big|_{t=t_s} = \frac{\alpha\,R_0}{(t_s - t_0)} \tag{6.4}$$

$$\Delta t \simeq a_{\rm PTV}/u_{sh1} \tag{6.5}$$

The post-shock peak-to-valley amplitude of the perturbation was then estimated:

$$a^*_{\rm PTV} \simeq a_{\rm PTV} - u_{sh2}\,\Delta t \tag{6.6}$$

This method provides a rough estimate for the post-shock amplitude, but is not intended as a quantitatively accurate calculation. The precise value of t_s depends strongly on the EOS of the plastic and modeling of the laser drive. All other parameters in Equations 6.3, 6.4, 6.5 and 6.6 are calculated by assuming a particular value for t_s. In fitting the shock-front position in the foam to the experimentally measured data (Equation 6.1 for R_{shock}), the parameter t_0 compensates for inaccuracy in the shock breakout time. Consequently, the uncertainty in t_s has little effect on t_m and R_{spike}, R_{bubble}. However, estimates for the initial shock velocity in the plastic and the post-shock perturbation amplitude are strongly affected by the uncertainty in t_s. In Table 6.3, I compare the result of these calculations for various values of t_s. Highlighted in red, $t_s = 2.5$ ns corresponds to the shock breakout time predicted by 2D CRASH simulations, which yields non-physical results. We expect a higher shock velocity in the lower-density material ($u_{sh2} > u_{sh1}$) and inversion of the initial perturbation pattern ($a^*_{\mathrm{PTV}} < 0$).

t_s (ns)	t_0 (ns)	α	u_{sh1} (μm/ns)	u_{sh2} (μm/ns)	$a^*_{\mathbf{PTV}}$ (μm)
2.4	0.7871	0.6034	62.5	56.11	0.4087
2.5	0.9141	0.6008	60	56.83	0.2116
2.6	1.041	0.5982	57.69	57.55	0.0098
2.7	1.167	0.5957	55.56	58.29	-0.1969
2.8	1.2932	0.5931	53.57	59.05	-0.4087

Table 6.3: Estimates of the initial shock velocities in the plastic (u_{sh1}) and the foam (u_{sh2}) and the post-shock perturbation amplitude (a^*_{PTV}) for various values of the shock breaktout time (t_s). Here, t_0, α are the power-law coefficients in Equation 6.1. The row highlighted in red corresponds to the value predicted by 2D CRASH simulations, $t_s = 2.5$ ns.

6.3 Analysis of Spike- and Bubble-Front Measurements for 2D, 3D, and Flat Targets

There are two possible explanations for why we observed no difference in mixed-zone width for 2D, 3D, and flat interface targets: 1) the system has evolved to chaotic mixing and lost memory of the initial conditions; or 2) the system remains single-mode, but experimental errors exceed the difference in spike or bubble height (2D versus 3D) for single-mode RTI growth. As discussed in Section 6.2, deceleration at the interface is not sustained for long enough to drive single-mode RTI growth to chaotic mixing. Internal target imperfections or external target misalignment may have resulted in chaotic mixing for some shots. However, after 22 ns, growth of the mixed-fluid layer is dominated by material decompression. The contribution from RTI may have been small enough that the difference between single-mode and chaotic growth is likely imperceptible in the mixed-zone width data. The analysis in Section 6.4.2 supports this conclusion.

In principle, the radiography images should distinguish between single-mode and chaotic mixing. There is clear single-mode structure in some shots (Figure 5.15), yet not in others where there was no evidence of target misalignment (Figure 6.4). Lack of single-mode structure in the radiography data does not necessarily imply chaotic mixing. Because radiography integrates through the target, a slight angular offset between the perturbation pattern axis and the imaging axis would "smear out" the single-mode structure, even when the target is externally well aligned. The rectangular target design and tolerance stack-up of multiple components in the assembly makes the pattern axis diffult to align to the required accuracy ($\leq 1^{\circ}$). From white-light interferometry scans of the ablator patterned surface, I measured the angle between the pattern axis and the edge of the part. After the ablator was mounted inside the gold base, I measured the angle between the edge of the ablator and a distal

alignment feature on the gold base, which registers the physics package inside the shield cone. Then, the angle of stalk (mounted to the outside of the cone) was manually adjusted to align the pattern axis to the imaging axis. For a complete target assembly, the uncertainty in angular alignment ranges from $1 - 2.5°$. (This does not include additional alignment error from target positioning). In the radiography image, angular misalignment of $2.5°$ corresponds to averaging the signal over 0.26λ across the tracer strip (240 μm in the primary view) and 1.2λ across the entire target (1100 μm).

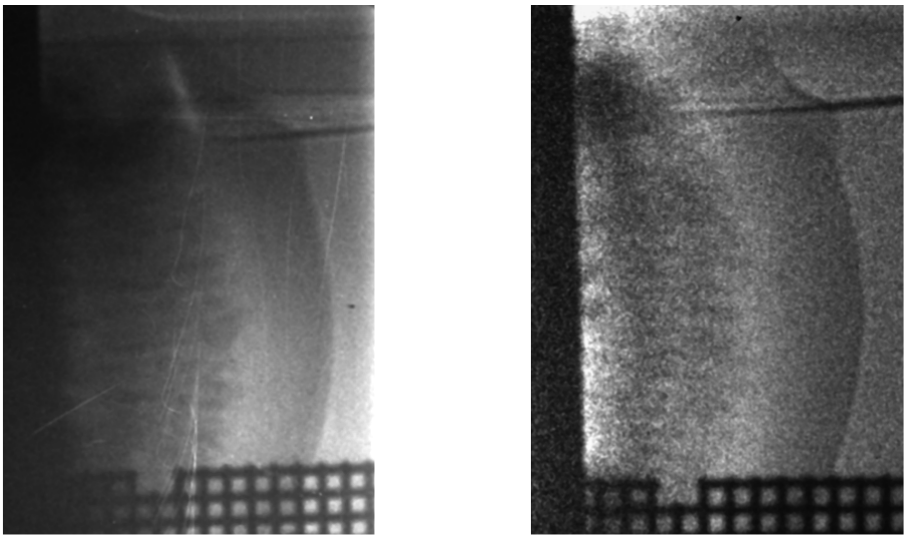

Figure 6.4: Radiography examples of well-aligned targets without clear single-mode structure. Left: RID90382, 3D target at 30 ns, film detector. Right: RID90393, 2D target at 30 ns, XRFC detector.

6.4 Comparison with Simulations and Buoyancy-Drag Models

2D CRASH simulations incorporate the temporal and spatial profile of the laser drive (Figure 5.14), but not a physically accurate model of laser-plasma interactions and energy conversion processes. To compensate for loss at the critical surface, a common approach is to reduce the simulation laser energy by a linear scale factor [106] [101] [42]. Typically, the scale factor is tuned so that the shock front position "best fits" the

experimental data. However, the scaled energy which best fits the shock front position may not be the best fit to the interface position. Miles *et al.* explored some of the factors which contribute to this discrepancy, which include: inaccurate equations-of-state, numerical methods implemented in the simulations, and differences in the curvature of the shock front in simulations versus experiment (which can artificially increase or decrease the normal component of the velocity in the simulation) [105].

6.4.1 2D CRASH Simulations: Laser-Energy Tuning

Since our publication of the low-Atwood number experimental design [42], the CRASH simulations have been updated. In the earlier design, the initial perturbation amplitude ($a = 4\,\mu$m) was twice that used in the final experimental design ($a = 2\,\mu$m). This change has no impact on the 1D dynamics and qualitative interpretation of the simulation results. Of greater importance, the new simulations incorporated a more accurate model of the 2D spatial profile of the laser drive, which resulted in significant, qualitative differences in the simulations and fit to the experimental data. The physical laser drive in the experiments has not changed and is similar to previous experiments at high-Atwood-number.

Previous work approximated the laser spot as a super-Gaussian function fit to the focal spot of a single drive beam at normal incidence with intensity multiplied by 10x (for the ten drive beams). The new CRASH simulations use a super-Gaussian function fit to the spatial distribution of the laser energy deposited on the drive surface. This spatial distribution is output from a Visrad simulation of the experimental design, which combines 10 drive beams at oblique angles of incidence. The beam angles range from 10-50 degrees, relative to normal incidence. None of the beams are actually at normal incidence to the drive surface. Figure 6.5 compares the two different spatial profiles, which have the same total energy in the laser spot, $E_{total} = \int_0^\infty I(r)dr \approx 4.6\,$kJ (in the 1 ns pulse). In the subsequent discussion, I will refer to these two spatial

profiles as the "one-beam" and "ten-beam" models.

For 2D CRASH simulations with the one-beam model, laser-energy scale factors of 60-70% produced excellent fits to shock front position and qualitative agreement in terms of the interface position for high-Atwood-number experiments [106]. In our one-beam simulations with 70% laser energy (for both high-A and low-A designs), the shock breakout time is 2.7 ns, which agrees with the results reported in numerous publications of high-Atwood number experiments and simulations. Referring back to the power-law fit to shock-front position in our low-Atwood-number experiments, $t_s = 2.7$ ns also yields qualitatively correct predictions for the initial shock velocity in the foam and post-shock perturbation amplitude (calculated in Table 6.3).

Figure 6.6 compares the low-Atwood-number experimental data with shock-front and mean-interface positions measured from 2D CRASH simulations of a flat-interface target at various laser-energy scalings with the ten-beam model of the laser drive. At 40% scaling, the simulation shock position (light-blue solid-line) agrees well with the experimental data, and the simulation interface position (green solid-line) agrees well with the CHI front measured for flat-interface targets, although that data set is small. In the ten-beam simulation at 40% laser-energy, the shock breakout time is 2.5 ns. In Figure 6.7, spike- and bubble-front positions are measured from a perturbed-interface simulation at 40% laser-energy and compared with the experimental data. On the same plot, shock and interface positions are included from the flat-interface simulation.

The more accurate model of the laser drive has revealed significant inaccuracies in the EOS for both the plastic and the foam. For these materials, the CRASH simulations used equations of state produced by PrOpacEOS [124], a proprietary program for which limited public documentation exists. Alternative EOS for the ablator and foam may provide better agreement with the experimental data.

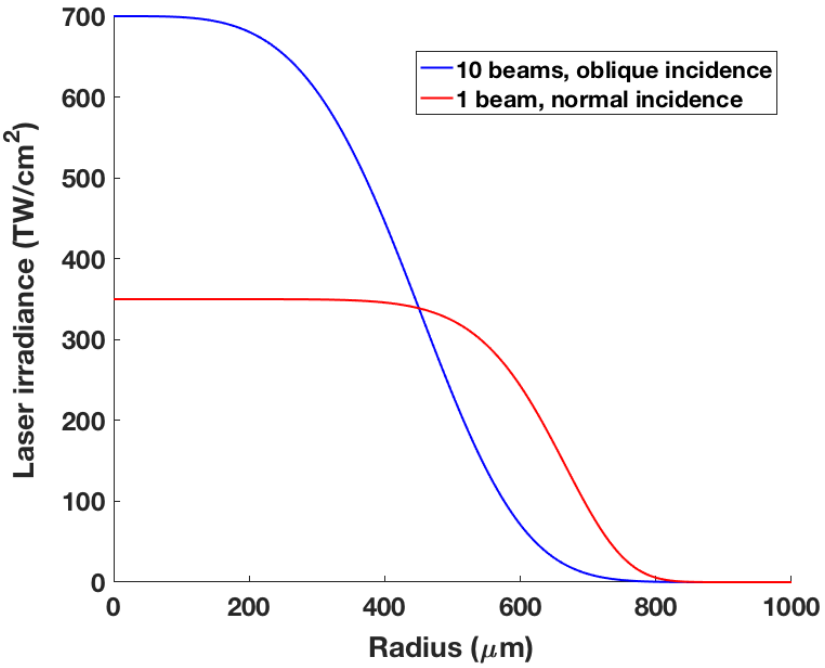

Figure 6.5: 2D CRASH simulations of the final experimental design incorporated a more accurate spatial profile of the laser drive (blue curve), which models the net irradiance from 10 drive beams at oblique angles of incidence. Previous simulations (red curve) modeled the laser spot as a single drive beam at normal incidence with peak irradiance scaled to match the total energy with 10 beams.

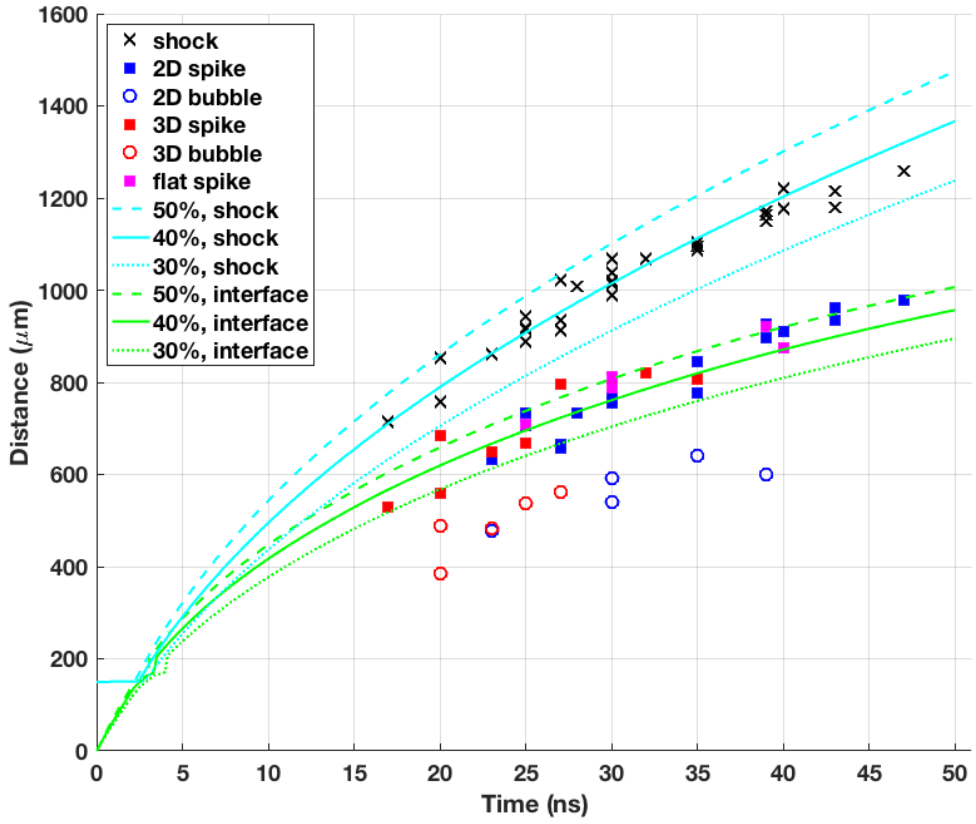

Figure 6.6: Shock and interface positions from 2D CRASH simulations with laser-energy scale factors of 30, 40, and 50 % are compared with the experimental data.

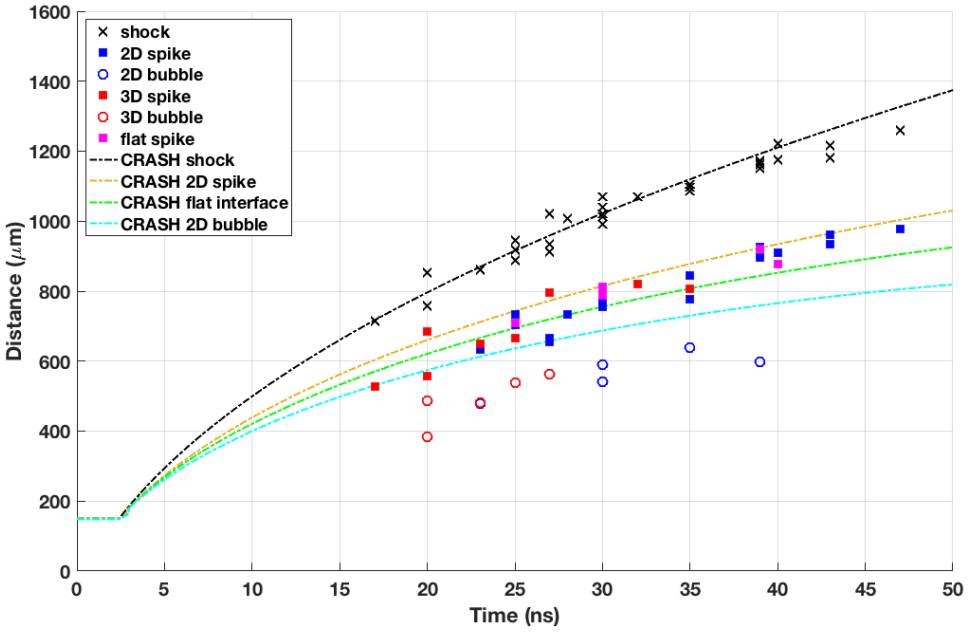

Figure 6.7: 2D CRASH simulations at 40% laser-energy scaling. The spike (orange) and bubble (light blue) positions are measured from a perturbed-interface simulation. The interface (green) and shock (black) positions are measured from a flat-interface simulation. Although the simulations agree with the experimental data in terms of shock and spike positions, the simulation greatly over-predicts the bubble-front position and under-estimates the total mixed-layer height.

6.4.2 Spike and Bubble Height Predicted by the Buoyancy-Drag Model

In Section 6.3, I hypothesized that the experimental platform at Omega 60 did not sustain deceleration for long enough to distinguish between growth rates for 2D and 3D classical, incompressible RTI. To solve the Srebro buoyancy-drag model (Equation 2.19), we need the temporal history of the interface acceleration and densities on either side of the interface. Flat-interface 2D CRASH simulations with 40% laser-energy scaling provide $\rho_1(t), \rho_2(t), A(t)$, and $g(t)$, plotted in Figure 6.8.

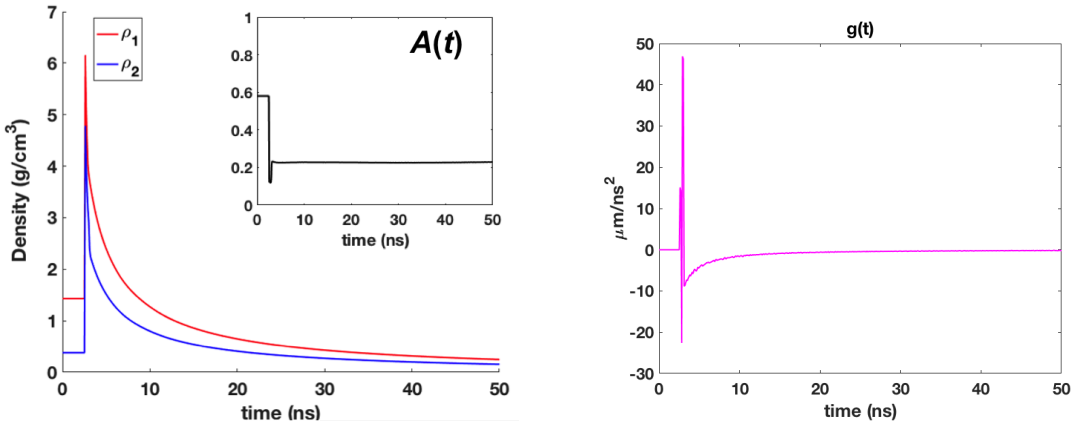

(a) (b)

Figure 6.8: Time-varying parameters measured from flat-interface 2D CRASH simulation at 40% laser energy. (a) densities and Atwood number; (b) interface acceleration.

The CRASH simulations wrote data to output files at 0.1 ns time steps. To calculate time-dependent quantities for the Srebro model, at each time step the simulation data was averaged along the x-axis over a transverse domain spanning three wavelengths: $0 \leq x \leq 120\,\mu$m. Within this domain, ρ_1 is the maximum density to the left of the interface. Similarly, ρ_2 is the minimum density in the region to the right of the interface and the left of the shock front. The peak-finding algorithm gives erroneous results prior to shock breakout ($t_s = 2.5$ ns). For $t < t_s$, I set $g = 0, \rho_1 = 1.43\,\mathrm{g/cm^3}, \rho_2 = 0.38\,\mathrm{g/cm^3}$ and the interface position, $z_{int} = 150\,\mu$m. The interface acceleration, $g(t) = \frac{d^2}{dt^2}(z_{int})$, is calculated by numerical differentiation

of the measured interface position.

The RTI growth phase begins at $t = 3.1$ ns, after which $g(t)$ increases monotonically from its peak negative value of $g(t = 3.1 \text{ ns}) = -8.83\,\mu\text{m/ns}^2$. (In Figure 6.8 (b), the data point $g(t = 2.8 \text{ ns}) = -22.6\,\mu\text{m/ns}^2$ is non-phyiscal and results from numerical noise.) Initial conditions for the Srebro model correspond to the height and velocity of the spike and bubble in the previous time step ($t = 3.0$ ns). The initial heights are calculated as:

$$\begin{aligned} h_{S,0} &= z_{spike}(t = 3.0 \text{ ns}) - z_{int}(t = 3.0 \text{ ns}) = 0.5\,\mu\text{m} \\ h_{B,0} &= z_{int}(t = 3.0 \text{ ns}) - z_{bubble}(t = 3.0 \text{ ns}) = 1.5\,\mu\text{m} \end{aligned} \tag{6.7}$$

However, it is not possible to resolve the initial spike and bubble velocities from the simulation data. As an estimate, I use the Meyer-Blewett formula (Equation 1.32) for the velocity during the Richtmyer-Meshkov growth phase:

$$\begin{aligned} u_{S,0} &= A^*\, k\, (du)\big(\frac{a + h_{S,0}}{2}\big) = 2.15\,\mu\text{m/ns} \\ u_{B,0} &= A^*\, k\, (du)\big(\frac{a + h_{B,0}}{2}\big) = 3.01\,\mu\text{m/ns} \end{aligned} \tag{6.8}$$

The post-shock Atwood number $A^* = 0.22$ is measured at $t = 3.1$ ns, when it reaches a steady value. The velocity induced at the interface is approximated as $du = u_{int}(t = 3.0 \text{ ns})$. Here, $a = 2\,\mu$m is the pre-shock perturbation amplitude for both spike and bubble.

Each buoyancy-drag equation (bubble or spike) constitutes a second-order ordinary differential equation (ODE), which I solve numerically as a system of first-order ODEs in Matlab. The time-dependent quantities $\rho_1(t), \rho_2(t), g(t)$ measured from the simulation data are passed as discrete numerical arrays to symbolic ODE functions. Within the ODE functions, piece-wise linear interpolants are fit to the simulation data, which are then evaluated at the time steps used by the ODE solver. The

buoyancy-drag model is solved using the initial conditions from Equations 6.7 and 6.8 and coefficients for both 2D and 3D geometries, shown in Figure 6.9. At the latest time in the experiment, the difference in mixed-layer width for 2D versus 3D RTI is 58 μm, which is significantly smaller than the shot-to-shot variation (115 μm). This result explains why we observed no difference in spike- and bubble-front positions for 2D, 3D, and flat targets.

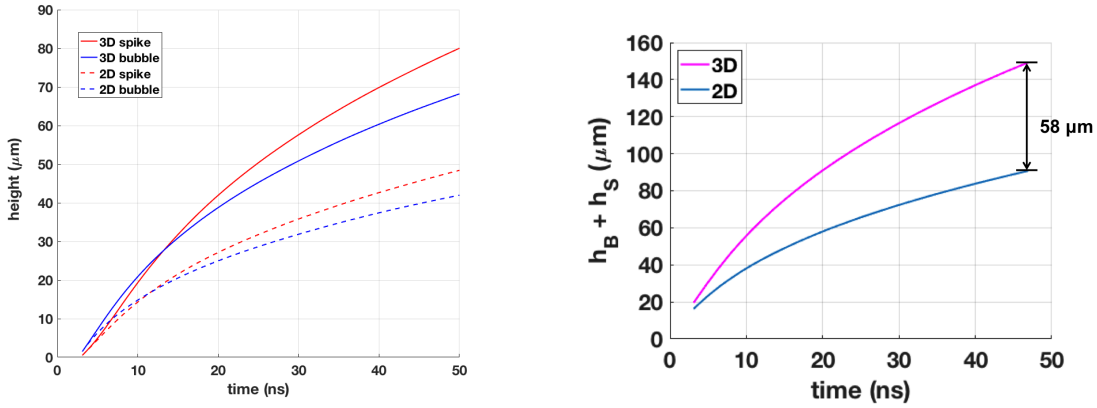

(a) (b)

Figure 6.9: Solution to Srebro buoyancy-drag model for 2D and 3D geometries with time-varying densities and interface acceleration from 2D CRASH simulations tuned to the experimental data. (a) Spike and bubble heights; (b) Total mixed-layer height.

6.4.3 Spike and Bubble Heights Measured in the Perturbed-Interface Simulation

In this blast-wave-driven system, both RTI and material decompression contribute to the measured growth of the mixed-fluid region. If spike and bubble velocities are sufficiently subsonic (relative to the sound speed in the surrounding post-shock fluid region), compressibility does not significantly affect RTI growth and material expansion can be treated as an independent term [110]. This approximation was valid for previous experiments at high-Atwood-number [106]. Expansion-corrected spike

and bubble heights are calculated as follows:

$$
\begin{aligned}
h_S(t) &= \Big[z_{spike}(t) - z_{int}(t)\Big] - \int_0^t \Big[u\big(z_{spike}(t')\big) - u\big(z_{int}(t')\big)\Big]dt' \\
h_B(t) &= \Big[z_{int}(t) - z_{bubble}(t)\Big] - \int_0^t \Big[u\big(z_{int}(t')\big) - u\big(z_{bubble}(t')\big)\Big]dt'
\end{aligned}
\tag{6.9}
$$

The first term represents the total feature height relative to the flat-interface position and the second term accounts for material decompression. Inputs to Equation 6.9 are:

$z_{spike}(t),\ z_{bubble}(t)$	spike- and bubble-tip positions from the perturbed-interface simulation
$z_{int}(t)$	mean-interface position from the flat-interface simulation
$u\big(z_{int}(t')\big)$	instantaneous fluid velocity from the flat-interface simulation, measured at $z_{int}(t')$
$u\big(z_{spike}(t')\big)$	instantaneous fluid velocity from the flat-interface simulation, measured at the position corresponding to $z_{spike}(t')$
$u\big(z_{bubble}(t')\big)$	instantaneous fluid velocity from the flat-interface simulation, measured at the position corresponding to $z_{bubble}(t')$

Figure 6.10 compares the expansion-corrected spike and bubble heights with the 2D buoyancy-drag model. Initially, the spike amplitude is compressed by its proximity to the shock front. This effect is included in the initial conditions for the buoyancy-drag model. However, this model is fundamentally incompressible and predicts faster growth for spikes, as compared to bubbles, in the nonlinear stage. In the model, spike height overtakes bubble height at approximately $t = 11$ ns. In the simulation, numerical noise creates a discontinuity in the expansion-corrected bubble height at $t \approx 9.5$ ns, where the bubble height jumps to a slightly lower value which happens to

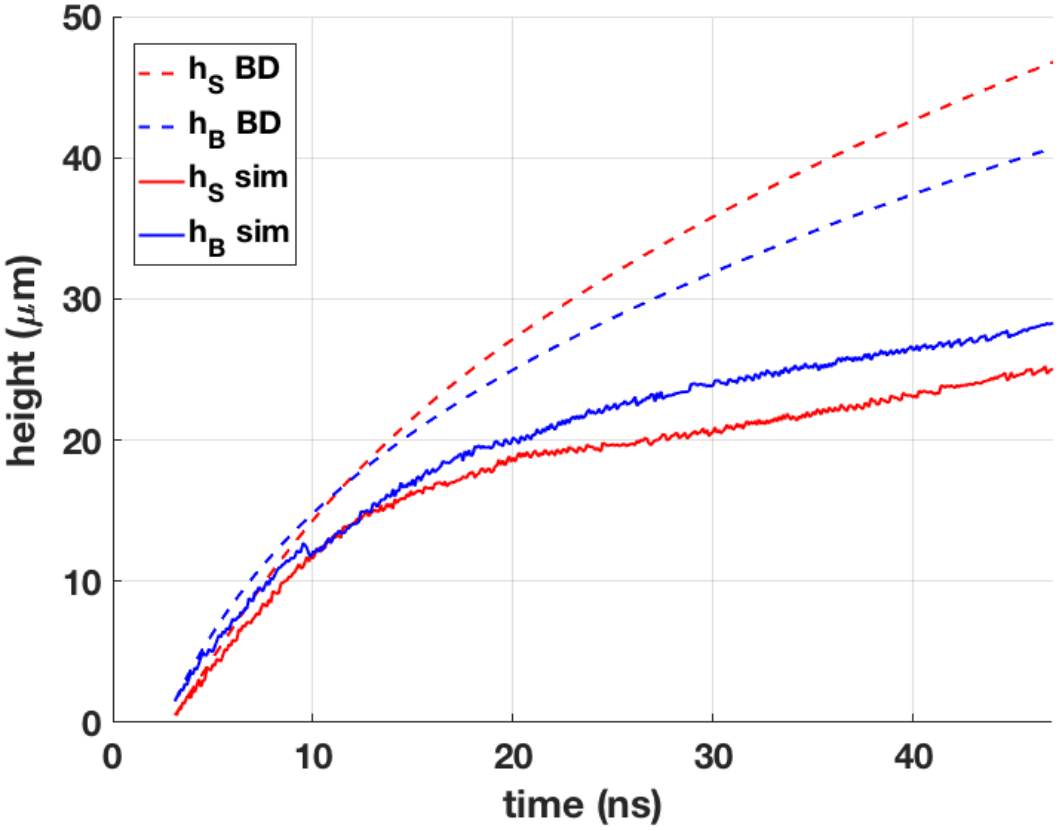

Figure 6.10: Expansion-corrected spike and bubble heights from the 2D CRASH simulation, compared with the 2D buoyancy-drag model.

coincide with the spike height at the same moment in time. This is a non-physical numerical artifact; the bubble continues to grow at a faster rate than the spike in the simulation until the equal-mass time ($t_m \approx 22$ ns), after which the bubble and spike grow at approximately the same rate.

Overall, Figure 6.10 demonstrates that this method for calculating expansion-corrected spike and bubble heights is not valid for the low-Atwood-number design. There are several incorrect assumptions embedded in the calculations:

1. Material compressibility does not significantly affect RTI growth
2. Constant post-shock Atwood number
3. Accuracy of the EOS

In reality, material compressibility reduces spike growth at early times, when the spike front is in close proximity to the shock front. However, it is difficult to quantify this effect due to the lack of experimental data at early times and mis-match between the simulations and the experimental data. Additionally, the post-shock Atwood number defined by our numerical methods may not accurately represent the local Atwood numbers at the spike- and bubble-fronts. More sophisticated post-processing of the simulation data is required. Inaccuracy of the EOS leads to a large discrepancy between the bubble-front position (and total mixed-layer height) in the simulation and the experimental data. The EOS problem also propagates to the buoyancy-drag model, which incorporates the interface acceleration $g(t)$ and compressibility (reflected in the Atwood number) measured from the simulations. The simulations greatly over-predict the interface position, and consequently, the interface acceleration and RTI growth rate.

CHAPTER VII

Conclusions and Future Work

To our knowledge, these experiments represent the first blast-wave-driven study of single-mode RTI growth at low-Atwood-number. Spike- and bubble-front positions and mixed-layer height were measured from 20 to 40 ns, however, growth of the mixed-fluid layer was dominated by material decompression after 22 ns. At earlier times (during the RTI growth phase), observation of the mixed-fluid region was obscured by target shielding. Although the Omega-60 platform did not drive RTI into the late-nonlinear growth stage, our goal was to demonstrate a design which utilizes existing target-fabrication methods and diagnostic capabilities and could be transitioned to a higher-energy facility. At NIF, Nagel *et al.* performed high-Atwood-number experiments of hydrodynamic instabilities (RM and RT) in a planar geometry using a half-hohlraum coupled to the physics package [113]. This platform may be capable of driving RTI growth into the desired regime for a low-Atwood-number target design. During the preliminary design of our Omega-60 experiments, we considered an indirect-drive approach. 1D simulations with a temperature-source model of a half-hohlraum at Omega-60 produced an acceleration profile at the interface, $g(t)$, which would extend the RMI phase and reduce deceleration during the the RTI phase. For the NIF design, the relative contributions from RM and RT instabilities would need to be assessed.

Shot-to-shot variations were comparable to those reported in similar blast-wave-driven experiments at Omega [106] [110]. Although this experimental error is acceptable for observing qualitative trends, the error must be greatly reduced in order to accurately measure the RTI growth rate in the late-nonlinear stage and quantify differences between experimental observations, numerical simulations, and theoretical models. At Omega-60, approximately 10-15 shots/day are possible, which enabled us repeat shots at the same observational times with different targets and measure the shot-to-shot variation in the data. At NIF, only 3 shots/day and 1-2 days of facility time would be possible. Fortunately, we expect the NIF platform to reduce errors related to target positioning and alignment, enable clear imaging of the mixed-fluid region from early to late times (without obstruction from target shielding), and ease manufacturing tolerances. The indirect-drive source provides more uniform pressure over the surface of the ablator and improves alignment because the hohlraum is coupled to the ablator during target assembly. Additionally, the higher-energy laser beams at NIF enable larger targets, thicker ablators, and brighter X-ray sources. In the experiments of Nagel *et al.*, the ablator was 450 μm thick with a cross-sectional area of 2500 x 1900 μm^2. The thicker ablator places the embedded interface farther down the shock tube and clear of shielding. The larger target cross-section ensures that the flow in the center of shock tube is unaffected by wall interactions for the duration of the experiment. For our experiments of single-mode RTI, the perturbation wavelength should be re-optimized for the NIF design (with the same aspect ratio $a/\lambda = 0.1$), in consideration of the amplitude compression during the RMI phase, a longer-duration potential-flow stage (during which longer-wavelength modes grow faster), and the larger transverse domain. A longer-wavelength mode would also improve the quality of the radiography data and ease target fabrication and angular alignment tolerances.

However, the Omega-60 experiments identified target-fabrication issues which are not ameliorated by the NIF platform. The ablator design with an inset tracer strip

pioneered by Robey *et al.* in 2001 [103] has become pervasive in HED experiments of hydrodynamic instabilities ([107] [106] [125] [126] [113] [127] [101] [128] [94] and others). Unfortunately, the expertise and resources required to produce reliable, consistent parts by this manufacturing method have not been sustained. The variability of the perturbation pattern and surface quality (detailed in Appendix B) introduce uncontrolled initial conditions, which may not have been significant in previous experiments, but matter here. The simulations of both Ramaprabhu *et al.* [49] and Wei and Livescu [79] showed that small differences in the initial conditions, although not apparent in the potential-flow stage, seed secondary instabilities which affect the time of onset for the reacceleration and chaotic mixing stages and the instantaneous velocity at the bubble tip within these stages.

The CRF foam also introduces significant uncertainty into the experiment. Although CRF is rigid enough for machining, the material is extremely brittle and prone to chipping and crumbling. Metrology of the machined surface of the foam showed large-scale voids and irregular surface roughness (see Appendix B). In the current target fabrication process, the foam is machined into a rectangular shape with nominally flat surfaces. This rectangular piece is manually inserted into the shock tube and pressed against the ripped surface of the ablator. It is likely that the CRF crumbles at the contact surface. Indeed, it may even be desirable to crush the foam so that particulate material fills the space between the ablator ripples. However, we have no means of inspecting the ablator-foam interface in the fully-assembled targets. In our Omega-60 experiments, the interface was obscured by target shielding, preventing pre-shot X-ray metrology of the interface. For the NIF targets, this should not be a problem; however, such metrology would not reveal the interior structure across the interface. In addition to these uncontrolled mechanical variables, the foam EOS [129] and its dependence on porosity and micro-structure [130], and the effect of preheat [114] on porous materials are poorly understood. The general assumption

is that preheat in advance of the shock front causes pore-collapse and homogenization of the foam at the interface. Simulations typically use an ideal-gas EOS with $\gamma = 1.4$ [110] [106] or a tabular EOS for solid polystyrene with the density scaled to match the foam [105].

Our 2D CRASH simulations used an EOS generated by PrOpacEOS. Previous experiments at high-Atwood-number showed good agreement with CRASH simulations using the same EOS [42]. However, the 2D spatial profile of the laser drive used in those simulations (single beam at normal incidence) was a poor approximation of the laser irradiance in the experiment (ten beams at oblique angles of incidence). New CRASH simulations implemented a more accurate model for the laser irradiance, but showed worse agreement with the experimental data. In the new simulations, 40% laser-energy scaling produced the best fit to shock front position in the foam (as compared to 70% scaling with the less accurate laser model), but resulted in a shock breakout time which did not agree with experimental results at high-Atwood number. In our low-Atwood-number experiments, the foam is 4-10x more dense than the foams used in previous experiments at high-Atwood-number. The denser foam may introduce subtle differences that warrant further study. Additional simulations should be performed using different EOS and compared to the experimental data. Future low-Atwood-number designs might also consider alternatives to CRF, perhaps a liquid or different type of foam which could be synthesized inside the shock tube to fit the shape of the patterned ablator.

Aside from target fabrication, there are more fundamental concerns about the physical observables in the experiment, how they compare with theory and simulations, and how they inform scientific understanding of the problem at hand. At very high Reynolds number, secondary KHI is the physical process which generates small-scale vortices, whose interaction drives reacceleration at the bubble tip and then causes chaotic fluctuations in the instantaneous velocity. The 2D high-resolution DNS of Wei

and Livescu predict that coherent structure and symmetry are preserved and that the bubble acceleration eventually becomes stationary [79]. However, this has yet to be observed in experiments. In the 2D experiments of Morgan *et al.*, secondary instabilities generated three-dimensional small-scale structures and individual spikes and bubbles began to interact and break up [76]. Their 3D experiments had only one wave across the test section and the evolution of the system was affected by wall interactions. The 3D LES of Ramaprabhu *et al.* predicted a stage of single-mode reacceleration followed by turbulent mixing [49].

In laboratory experiments of single-mode RTI at high Reynolds number, many wavelengths should span the transverse domain, in order to observe the late growth stages in a system unaffected by wall interactions and permit the possibility of self-similar growth where $L(t) \sim h(t) > \lambda$. (Here λ is the wavelength of the single-mode seed perturbation.) In any real-world system (whether HED or classical fluids), there will be slight variations and inhomogeneities across the xy-plane, which cause individual spikes and bubbles to evolve differently in the late growth stages. Thus, laboratory experiments diverge from the theoretical description of single-mode RTI and numerical simulations with periodic boundary conditions. The question arises: how should the bubble (or spike) tip be defined for this regime of quasi-single-mode RTI? Morgan *et al.* identify the bubble tip position z_B as the point with the steepest intensity gradient "in the vicinity of the bubble," calculated by numerical analysis of the image data in each camera frame. By this definition, the transverse coordinates of z_B may vary over time and it is unclear how this applies when individual spikes and bubbles interact and break up. In our HED experiments, z_B corresponds to the visually-identified steepest gradient in image intensity (averaged over y) in the vicinity of the x-coordinate which lies along the line normal to the vertex of the shock front. These definitions of bubble tip position are not consistent with either the single-mode definition (which applies at a fixed transverse coordinate through the center of a single

bubble) or a multi-mode definition (such as that of Youngs, Equation 2.25).

Design of a future experiment at NIF should be informed by a rigorous simulation study which:

1. Compares different EOS for the plastic and foam and evaluates the impact of the uncertainty in the EOS and whether the experimental objectives can be achieved.

2. Predicts acceleration at the interface $g(t)$ for the hohlraum drive, the relative contributions of RM and RT instabilities, and whether the blast wave sustains deceleration for long enough to drive single-mode RTI from the potential-flow stage to the reacceleration and chaotic mixing stages.

3. Determines the optimal seed perturbation wavelength for the NIF target design.

4. Calculates and compares spike and bubble height, instantaneousness velocity, and Froude number for both single-mode and multi-mode definitions, during all growth stages.

5. Includes synthetic diagnostics which model the radiography (including spatial integration along y, spatial resolution in x, z, and background noise), the uncertainty in the absolute position of the fiducial reference (from target metrology), the detector integration time, and the temporal sampling rate of the experiment (number of shots and interval between observation times).

6. Uses the synthetic diagnostic data to calculate spike and bubble height, instantaneous velocity and Froude number by the same methods that will be applied to the actual experimental data. This should then be compared with the spike and bubble growth found in step 3.

Experiments at NIF are extremely expensive and involve years of advanced planning. Further simulations studies are needed to determine whether the NIF platform is

capable of driving single-mode RTI growth to the reacceleration and chaotic growth stages and whether the diagnostics can measure a trend in mean-velocity which accurately describes the late stages of the instability growth. Additionally, significant improvements to target fabrication and metrology methods would be required.

APPENDICES

APPENDIX A

Matlab Image Processing

A.1 Spatial Calibration with Fiducial Grids

Gold grids are mounted on the exterior walls of the shock tube facing the imaging diagnostics. Grid specifications are as follows: square pitch = 64 μm, bar width = 26 μm, hole width = 38 μm. This enables calibration of the spatial scale in the radiography images. Along the top edge of each grid, gold bars are clipped at designated locations to create two notches that serve as absolute spatial references. The notch nearest the drive surface is 2 squares wide; the farther notch is 3 squares wide. During target assembly, the position of each notch is measured relative to the PI-coated surface of the target base, which is assumed to be coplanar with the drive surface of the ablator.

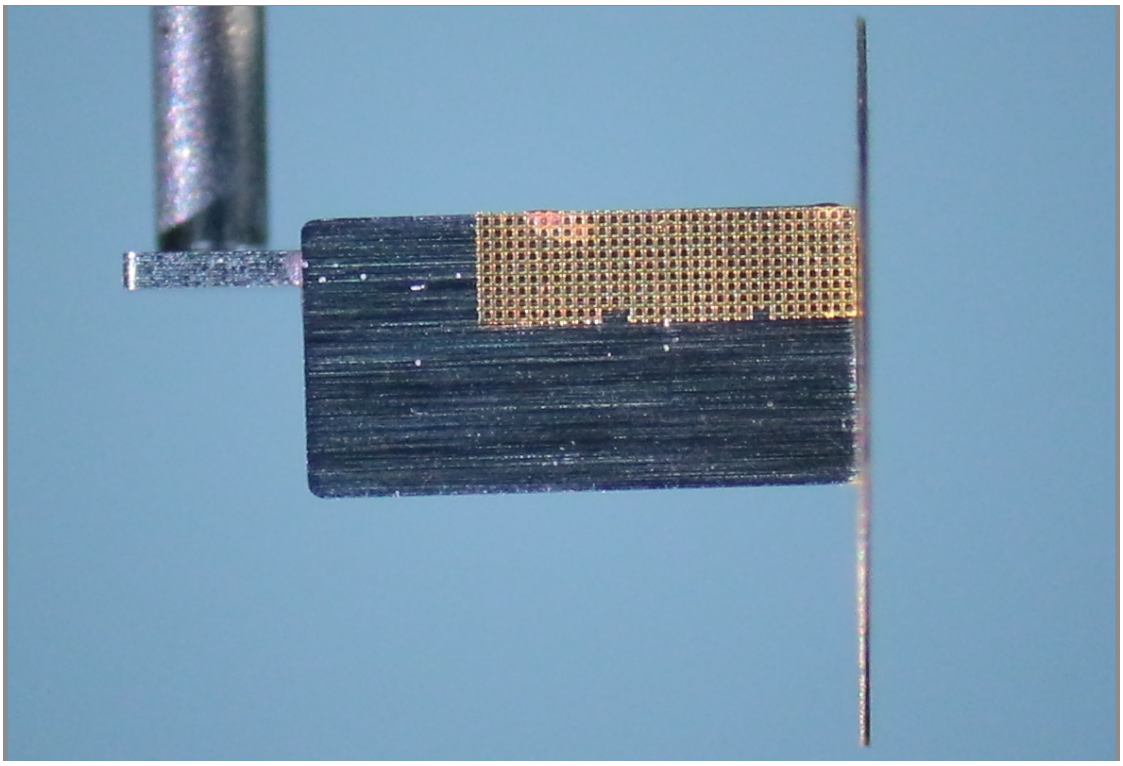

Figure A.1: The targets are assembled in stages so that interior features can be measured relative to the drive surface and fiducial grid references. This photo shows a metrology view equivalent to TIM4 during assembly of the target shot in RID90382.

A.2 Matlab Methods for Image Processing

The facility (LLE) provides the raw data from diagnostics in .hdf file format. As an example, I will use the image data from RID90382-TIM4. This shot demonstrates the impact of inadequate target shielding. In an attempt to obtain data at earlier times, some targets were built with the gold foil on the outside of the acrylic cone (Figure 5.12) positioned closer to the drive surface. Part of the detector FOV was exposed to background noise (laser and X-ray emission at the drive surface).

Shot day:	July 18, 2019
Target type:	Low-A, 3D perturbation
Measurement time:	30 ns
Backlighter pinhole exit diameter:	20 μm
Detector:	film (ungated)
TIM4 radiography axis:	primary

My Matlab code performs the following steps for image processing and analysis:

1. Read dataset from .hdf file. This is a 2D array of unsigned 16-bit integer values representing the image intensity at each pixel of the detector. Figure A.2 shows a histogram of the raw data.

2. Convert data to gray-scale image, shown in Figure A.3. This is a 2D array of double-precision floating-point numbers in the range [0,1].

3. Crop image and rescale intensity range, shown in Figure A.4.

4. Take a lineout parallel to the horizontal axis of the fiducial grid, shown in Figure A.7(a). Using this lineout, calculate the average number of pixels between grid squares and convert distance units from pixels to microns. For this image, the conversion factor is 2.63 μm/pixel.

5. Determine the spatial resolution using the method described in Section A.3. For this image, $N = 3$, which corresponds to spatial resolution: 3 pixels $\times$ 2.63 μm/pixel = 8 μm. (Note that the measured resolution element is 40% the size of the pinhole exit diameter, which indicates significant pinhole closure.)

6. Apply an image filter which averages over the spatial resolution element, shown in Figure A.5.

7. Measure shock, spike, and bubble front positions relative to the fiducial reference.

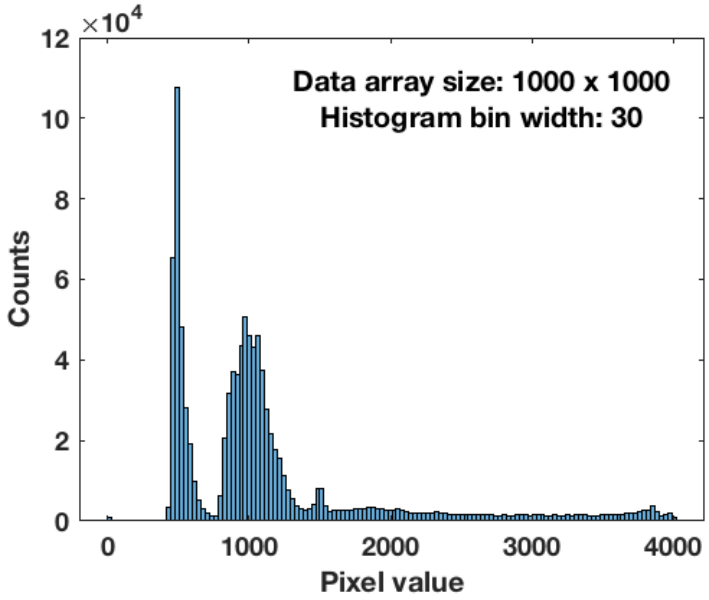

Figure A.2: RID90382-TIM4: Histogram of the raw image data.

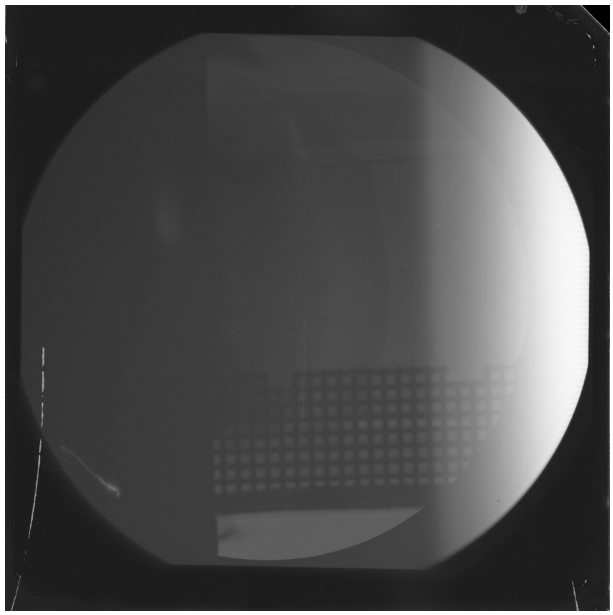

Figure A.3: RID90382-TIM4: Original gray-scale image. The circular apertures correspond to the nose-cone and vignetting from the filter packs. The bright white band on the right side of the image results from inadequate target shielding. The thin white lines are scratches in the film.

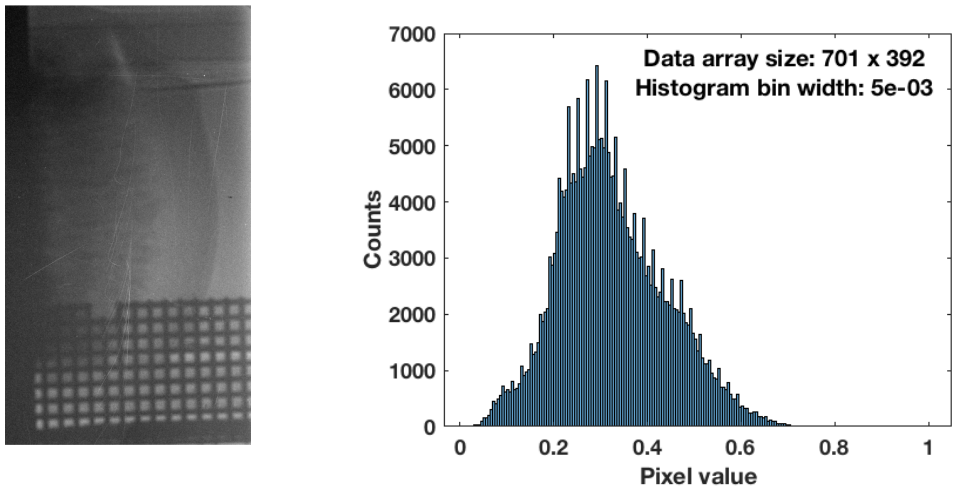

Figure A.4: RID90382-TIM4. Left: image cropped and intensity rescaled. Right: histogram of rescaled intensity values for the cropped image.

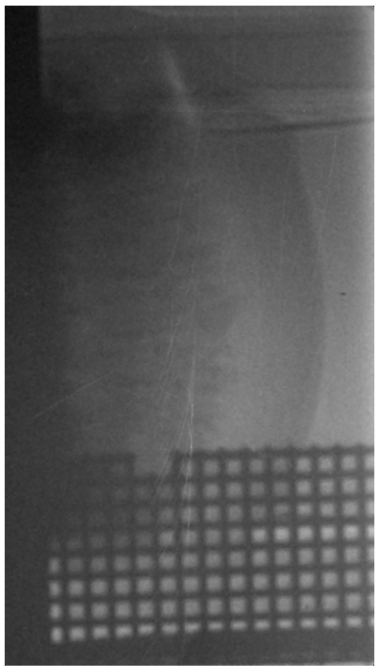

Figure A.5: RID90382-TIM4. Filtered image with averaging over the spatial resolution.

A.3 Method to Determine Spatial Resolution of the Image

From the cropped image with scaled intensity, I take a lineout parallel to the horizontal axis of the fiducial grid, as shown in Figure A.7(a). Next, I average the image over $N = 3$ pixels using the method described below and take a lineout from the averaged image at the same position as the original lineout. Then I increase N until the peaks and troughs in the lineout (corresponding to the edges of the grid bars) begin to broaden–this indicates that the image data is being averaged over a domain larger than the resolution element.

Algorithm for sliding-neighborhood averaging operation:

1. For each pixel $px(j)$ in the input image (j ranges from 1 to the total number of pixels), determine the pixel's neighborhood. This is an array of $N \times N$ pixels centered about $px(j)$. (N is an odd integer.)

2. Apply a function to the values of the pixels in the neighborhood. This function is an averaging operation which sums the values of the pixels in the neighborhood and then divides the result by the number of pixels in the neighborhood (N^2). The result of this calculation is the value of the output pixel.

3. Find the pixel in the output image whose position corresponds to that of $px(j)$ in the input image. Set this output pixel to the value returned by the averaging function. The size of the output image is the same as the size of the input image.

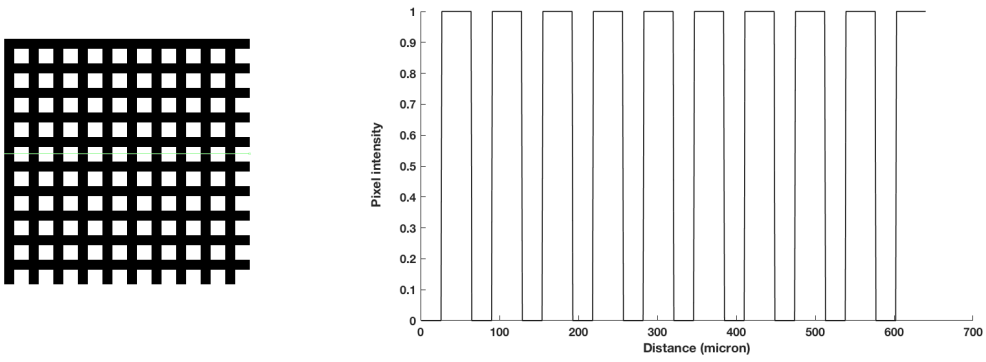

Figure A.6: Ideal synthetic grid. Left: image of the grid. Right: Horizontal line-out through the center of the grid.

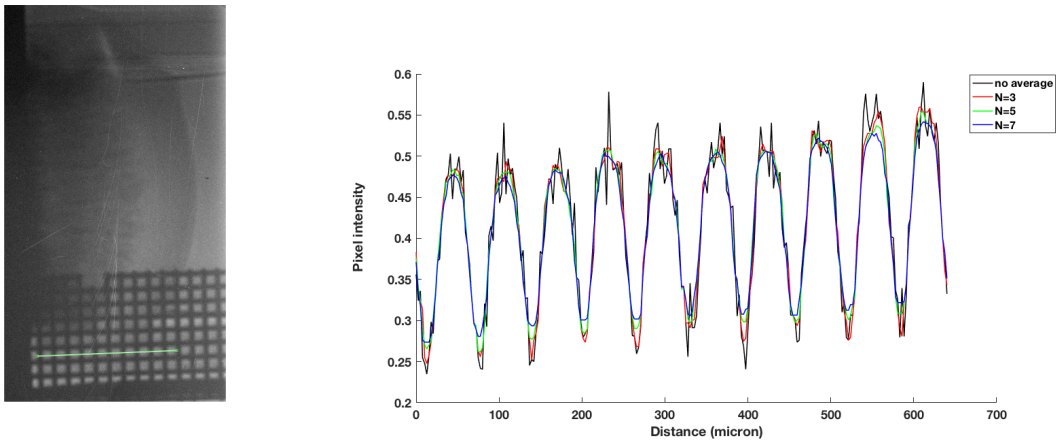

(a) (b)

Figure A.7: RID90382-TIM4. For this image, the spatial resolution element is approximately 8 μm , corresponding to $N = 3$ pixels in each linear dimension. (a) Location of line-out shown on the image; (b) Line-outs without spatial averaging and with averaging over $N = 3, 5, 7$ pixels.

APPENDIX B

Target Metrology

B.1 Patterned Surface of the Ablator

The manufacturer of the ablators provided raw data from white-light interferometry (WLI) scans of the patterned surface of each part. In Matlab, I wrote scripts to import the WLI data, perform planar tilt correction (to compensate for the WLI platform tilt), plot surface contour maps, take line-outs across the part, and measure:

- Pattern amplitude and wavelength
- For 3D parts, phase ϕ along the center of the part: $\cos(kx) + \cos(ky + \phi)$
- Phase-drift across the part
- Alignment of pattern axes to edges of the part
- 2D FFT of perturbation spectrum
- Bowing across the part
- CHI depression

An extensive data set exists for all this metrology. Figure B.1 shows only a few images which highlight discrepancies between the ideal pattern specifications and the parts delivered.

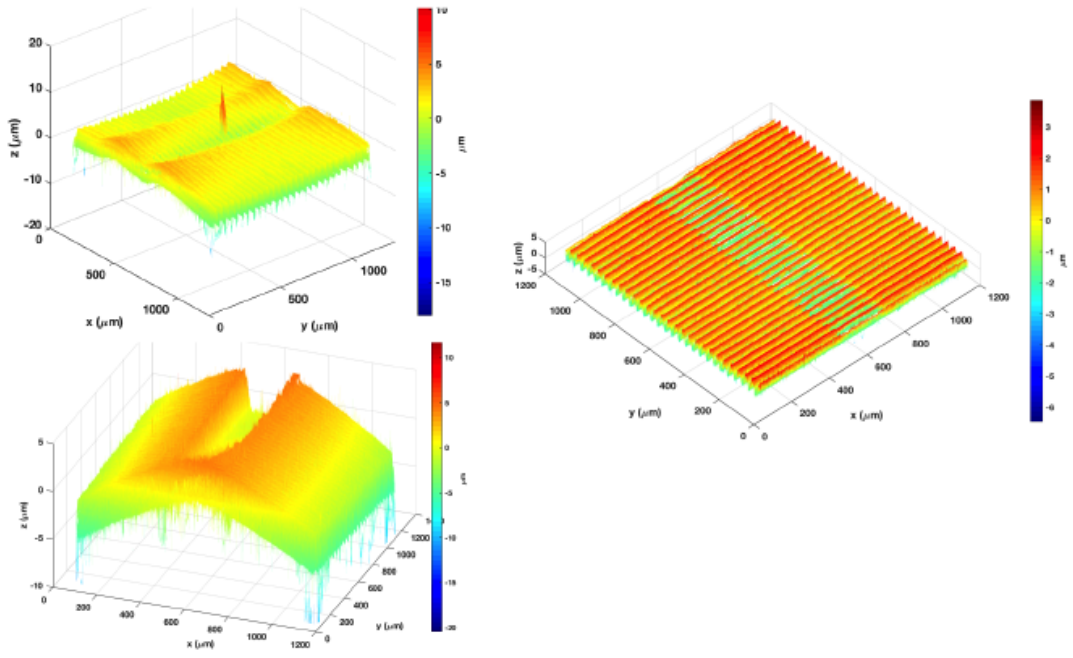

Figure B.1: White-light interferometry scans of the surfaces of three different ablator parts (with 2D perturbation patterns)

B.2 CHI Material

During target assembly, we observed large bubbles and voids in the tracer strip (in the interior of the CHI material). Several examples are shown in Figure B.2. We performed higher resolution scans of the surface of a flat ablator using a dual-confocal scanning microscope with 10 nm spatial resolution. This metrology was performed at the Lurie Nanofabrication Facility (LNF) at the University of Michigan. These high-resolution scans (Figure B.3) revealed tool marks (long, narrow scratches) and micron-scale pits across the surface of the part.

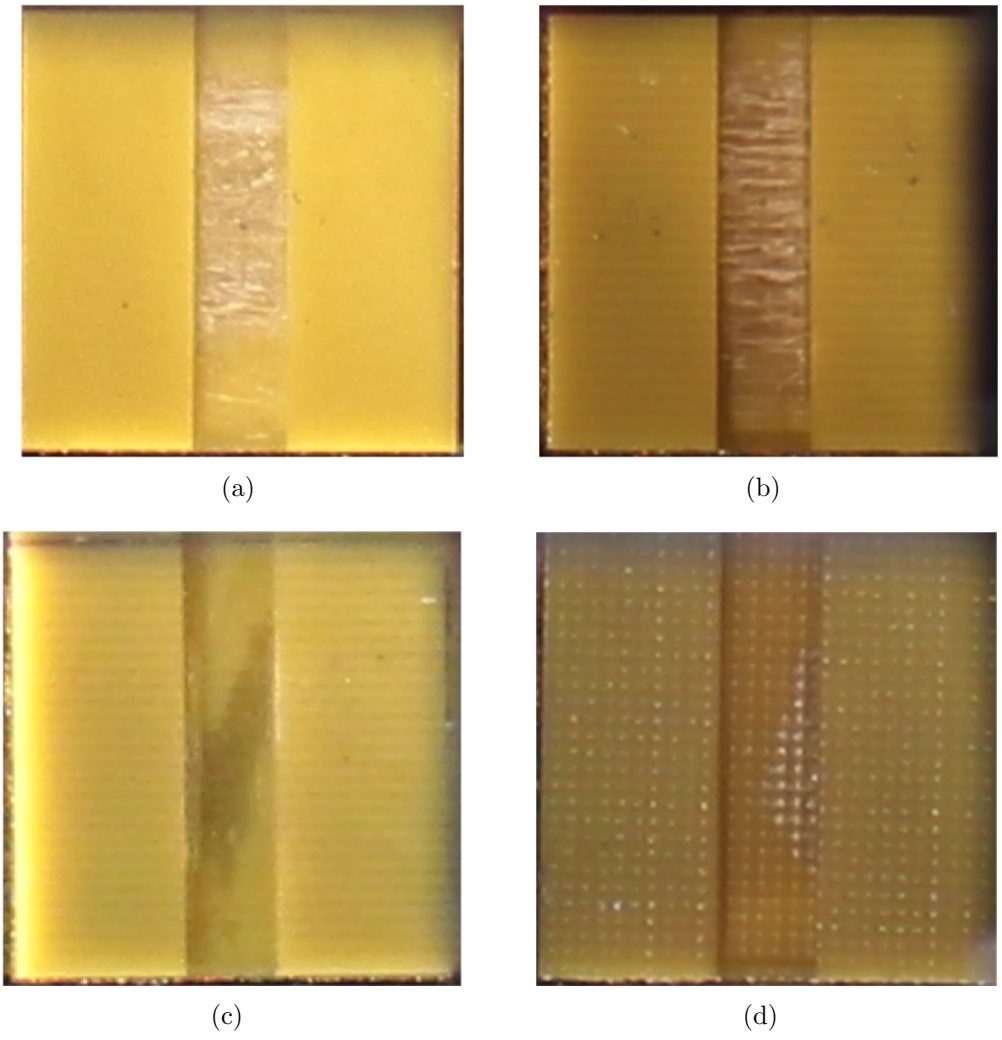

Figure B.2: Metrology photos of the ablator patterned surface ($1100 \times 1100\ \mu m^2$) showing large bubbles and voids in the interior of the CHI tracer strip. (a) Flat target 1103 (not shot); (b) 2D target 2205 (not shot); (c) 2D target 2101 (RID60393); (d) 3D target 3106 (RID90382).

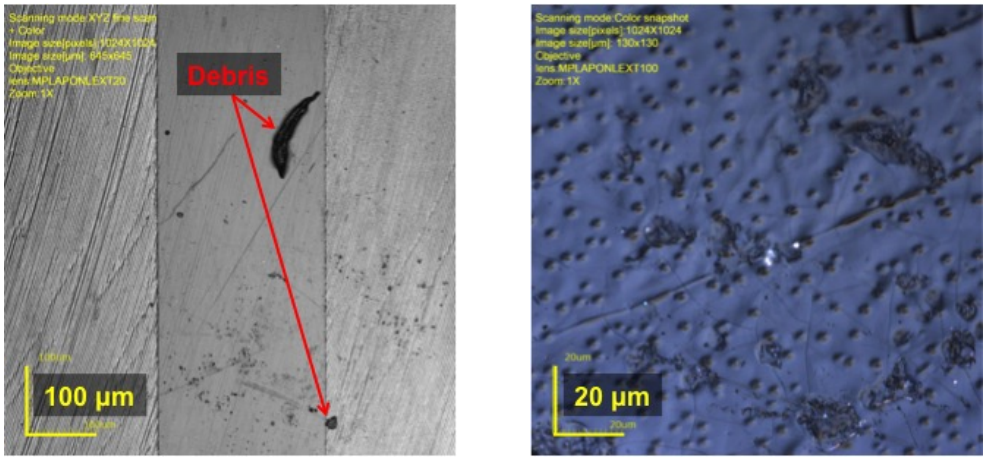

(a) (b)

Figure B.3: Dual-confocal microscope photos of the tracer strip in a flat target. (a) 20× magnification reveals tool marks (slanted lines) across the surface of the part. The two specks of external debris are not target defects; (b) 100× magnification reveals micron-scale pits on the surface of the CHI. Different optical sources and filters were used for these two photographs, creating the false-color appearance.

B.3 CRF Foam

Figure B.4 shows an example of a typical piece of CRF foam ($0.38\,\mathrm{g/cm^3}$), prior to insertion into the shock tube. The material is very brittle and easily damaged by machining and handling. Metrology photos revealed large-scale chips and voids. Additional defects may have been introduced during insertion into the tube. We have no information about the micro-structure of the foam (pore size distribution) or homogeneity of the bulk material.

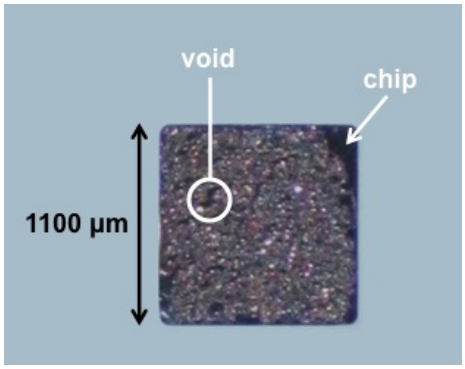

(a)

(b)

Figure B.4: Example of machined CRF foam ($0.38\,\mathrm{g/cm^3}$), prior to insertion into the shock tube. (a) End-view (surface in contact with the ablator); (b) Side-view. Machining and handling of the material introduce large-scale chips and voids (visible in both the end- and side-views). The machining process also introduces periodic tool marks (visible in the side view). On the far end, the "nub" is an intentional design feature to facilitate tool attachment and handling. The large chip near the nub was accidental, but inconsequential because the shock front will not travel that far down the tube at the latest observation time in the experiment.

B.4 X-ray Scans of Physics Packages Extracted from Unused Targets

Target shielding prevented pre-shot X-ray metrology of the fully assembled targets. We extracted physics packages from unused targets and mounted them in custom holders for X-ray scans at Los Alamos National Laboratory (LANL) with a Cr source (5.4 keV). Nominally, the interface is positioned 100 μm above the top surface of the gold base (a 50 μm thick, 4 mm diameter circular disk). Unfortunately, the interface was still obscured by the gold in most of the images due to a slight tilt on the platform. (For these targets, 3.4 degrees tilt results in complete obscuration of the interface.) Figure B.5 shows a CAD model of the extracted physics package. Figure B.6 shows how the physics package is mounted inside the holder for the X-ray scans at LANL. Although the sample size was small, we observed significant differences in the quality of the targets. Figure B.7 shows an example of a good-quality target. Figure B.8 shows an example of a poor-quality target with large gaps between the ablator, foam, and shock tube walls.

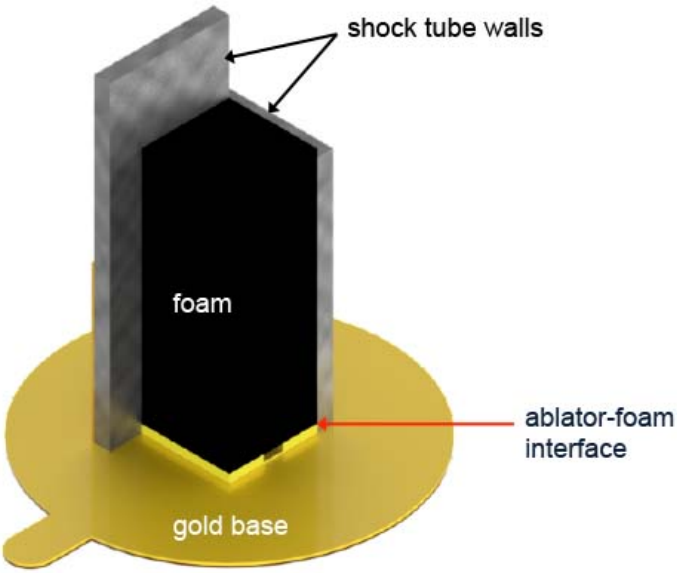

Figure B.5: CAD model of extracted physics package (by Sallee Klein). For illustration purposes, two of the shock tube walls are not shown (all four walls of the tube are intact in the actual part).

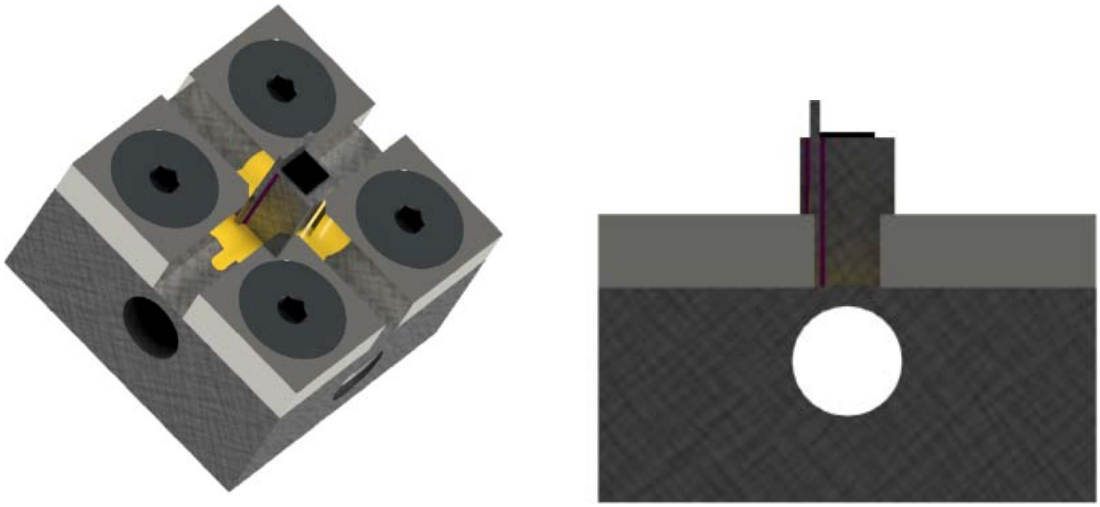

(a) (b)

Figure B.6: CAD model of the physics package inside the holder for X-ray scans at LANL (by Sallee Klein). (a) perspective view; (b) view corresponding to the anti-TIM4 axis in the Omega-60 target chamber.

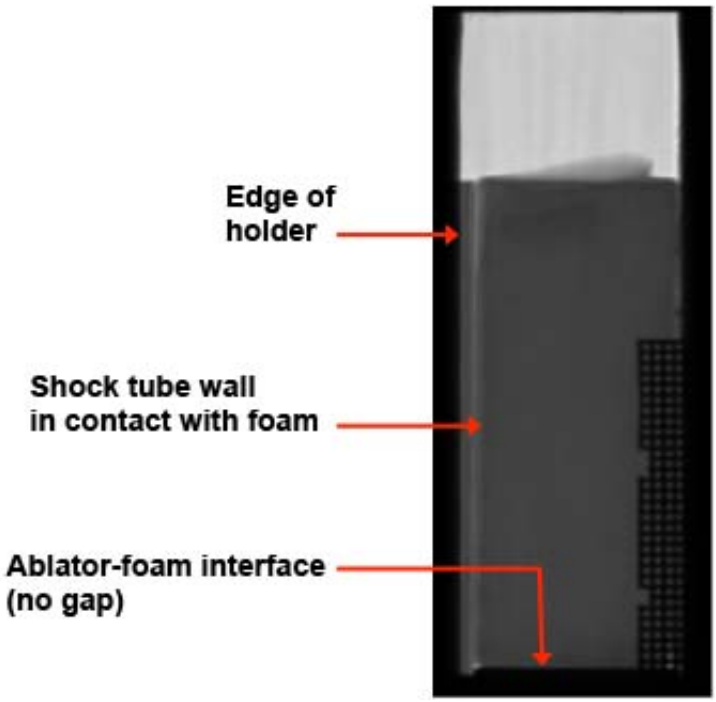

Figure B.7: LANL X-ray scan: example of a good-quality target. The fiducial grid provides the spatial scale (64 μm square pitch).

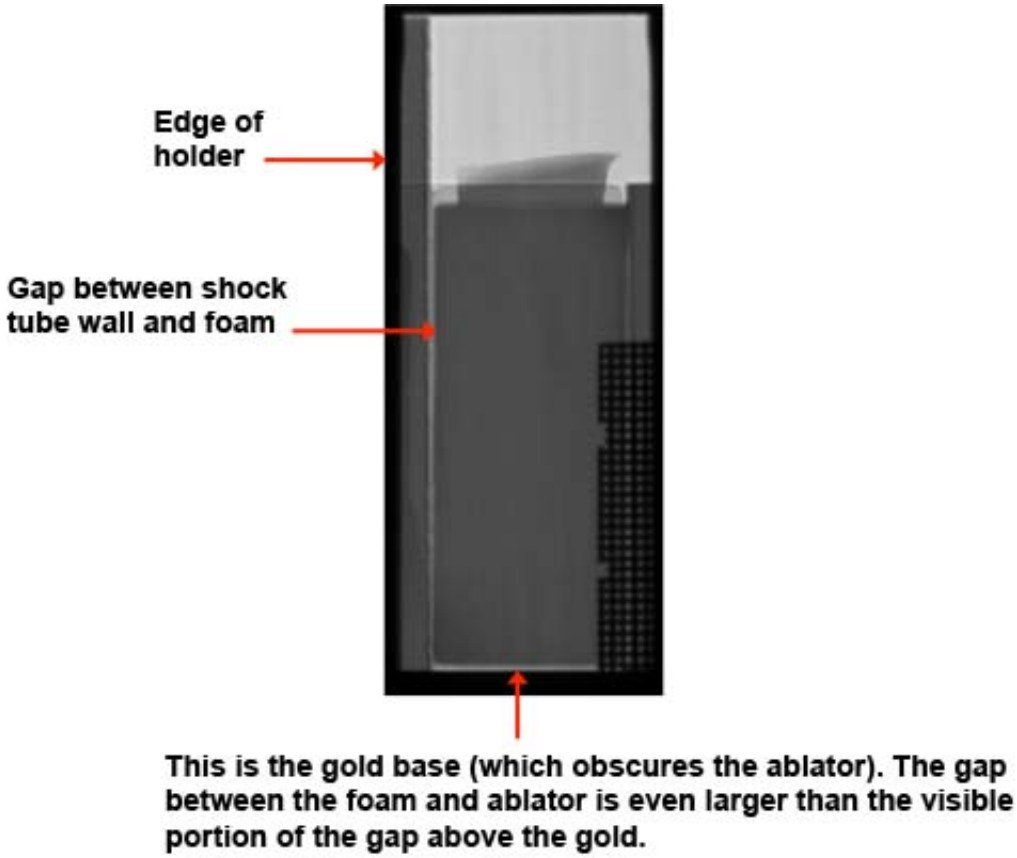

Figure B.8: LANL X-ray scan: example of a poor-quality target with large gaps between the ablator, foam, and shock tube walls. The fiducial grid provides the spatial scale (64 μm square pitch).

APPENDIX C

Shot Day Summary

This appendix summarizes the data obtained on each of the four shot days: October 6, 2016, April 6, 2017, April 19, 2018, and July 18, 2018. Two different types of detectors were used: gated X-ray framing cameras (XRFC) and un-gated direct-exposure X-ray film. The image intensity data has been scaled for optimal visibility in the figures below. The XRFC images include the entire detector FOV. The film images have been cropped to exclude regions saturated by background noise (for example, see Figure A.3).

C.1 Shot Day: October 6, 2016

RID	SRF	Target ID	Target type	Primary Axis (TIM3c) Time	BL	Det.	Secondary Axis (TIM4) Time	BL	Det.	Notes
83093	59810	test target			test BL	XRFC3		test BL	XRFC4	1
83094	59421	0	high-A, 3D λ_{71}	15 ns	V10	XRFC3	15 ns	V20	XRFC4	
83095	59057	30	high-A, 3D λ_{40}	15 ns	V10	XRFC3	15 ns	V10	XRFC4	
83097	59161	31	high-A, 3D λ_{40}	25 ns	V10	XRFC3	25 ns	V10	XRFC4	2
83098	59162	3	low-A, 3D λ_{71}	20 ns	Ni10	XRFC3	25 ns	Ni20	XRFC4	
83099	59822	22	low-A, flat-λ_{71}	40 ns	Ni10	XRFC3	40 ns	Ni10	XRFC4	
83100	59164	10	low-A, flat	40 ns	Ni10	XRFC3	40 ns	Ni20	XRFC4	
83101	59163	11	low-A, flat	30 ns	Ni10	XRFC3	30 ns	Ni10	XRFC4	
83103	59823	4	low-A, 3D λ_{71}	30 ns	Ni20	XRFC3	30 ns	Ni10	XRFC4	
83104	59824	23	low-A, flat-λ_{71}	30 ns	Ni20	XRFC3	30 ns	Ni10	XRFC4	
83105	59825	21	high-A, flat-λ_{71}	15 ns	V10	XRFC3	15 ns	V20	XRFC4	
83106	59827	32	high-A, 3D λ_{40}	25 ns	V10	XRFC3	25 ns	V10	XRFC4	
83107	59828	33	high-A, 3D λ_{40}	20 ns	V10	XRFC3	20 ns	V10	XRFC4	
83108	59926	1	high-A, 3D λ_{71}	20 ns	V20	XRFC3	20 ns	Ni10	XRFC4	3

Table C.1: Shot Log for October 6, 2016

Notes:

1. Debris test shot
2. XRFC4 error (no TIM4 data)
3. Ran out of V BLs, used Ni BL for secondary axis

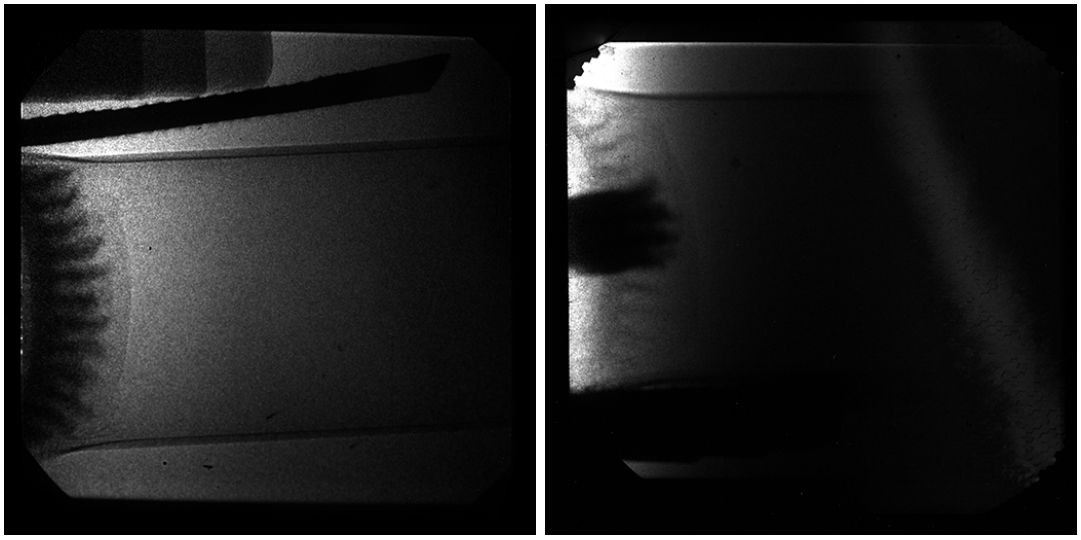

(a) TIM3c (b) TIM4

Figure C.1: RID 83094: image data

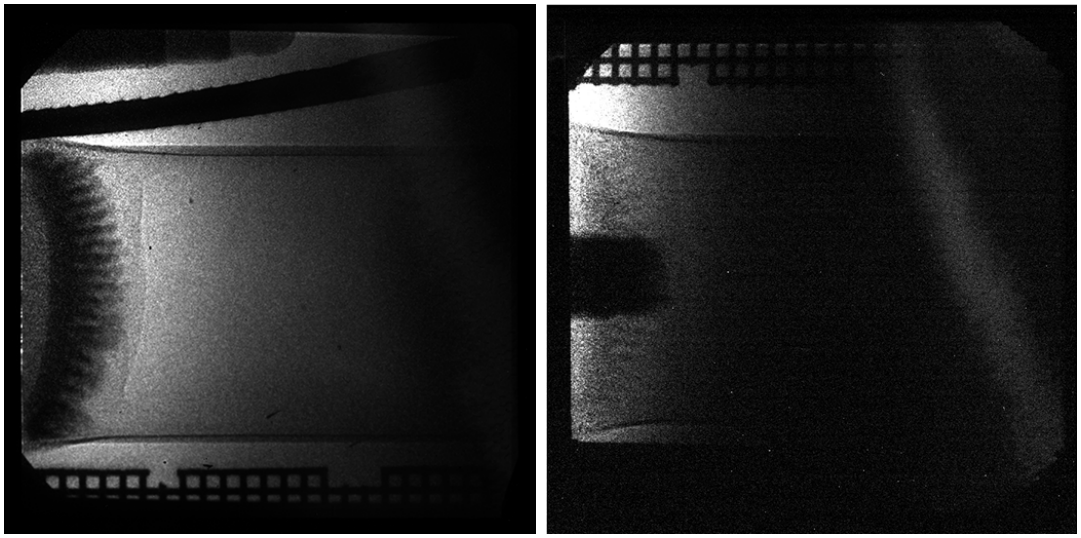

(a) TIM3c (b) TIM4

Figure C.2: RID 83095: image data

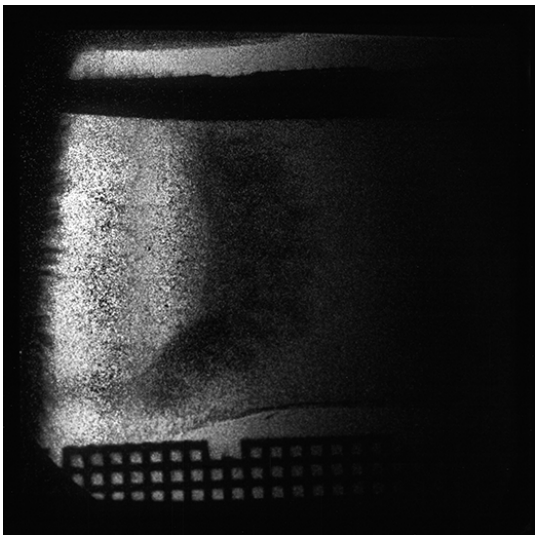

TIM3c

Figure C.3: RID 83097: image data

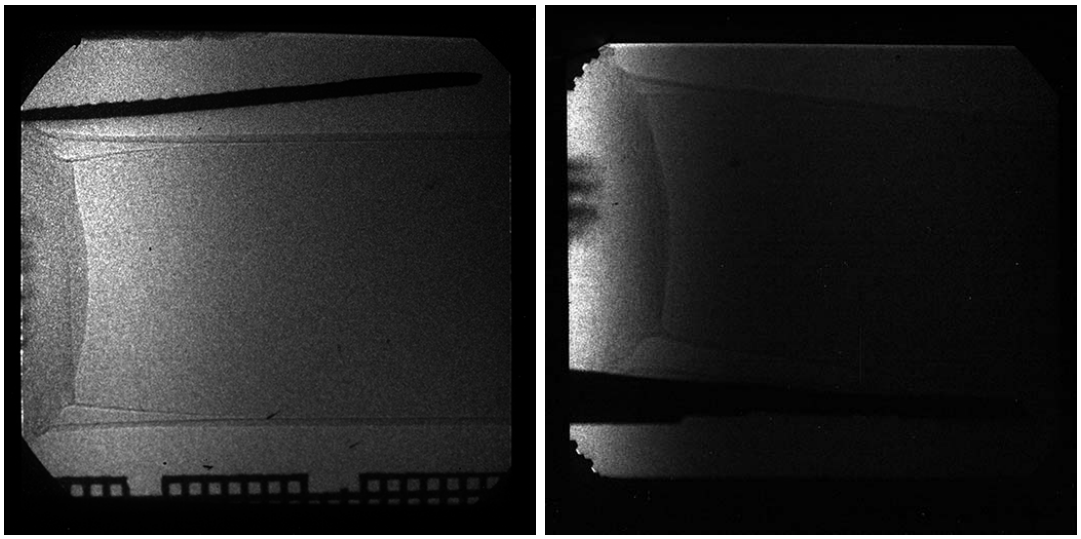

(a) TIM3c (b) TIM4

Figure C.4: RID 83098: image data

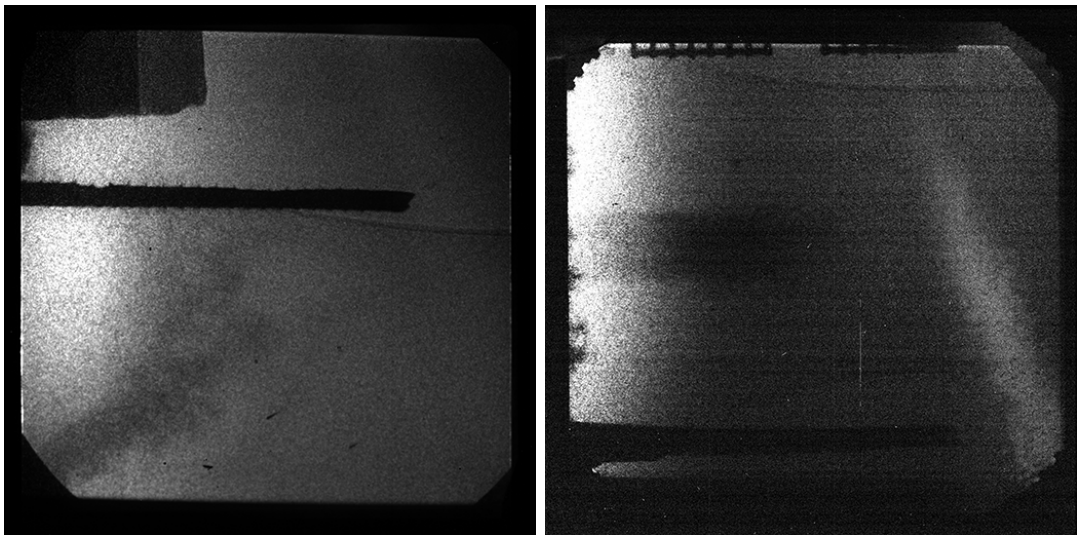

(a) TIM3c (b) TIM4

Figure C.5: RID 83099: image data

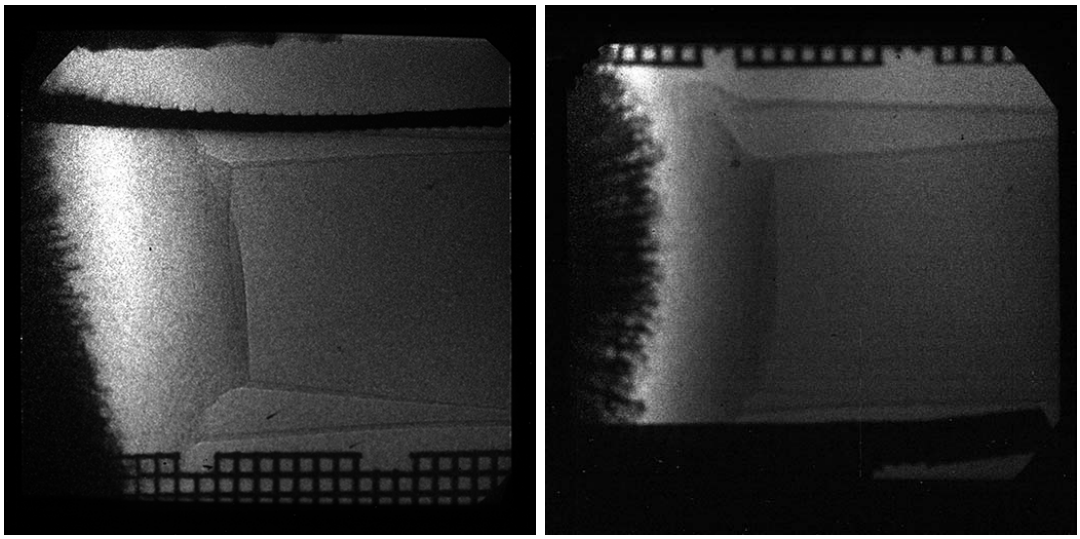

(a) TIM3c (b) TIM4

Figure C.6: RID 83100: image data

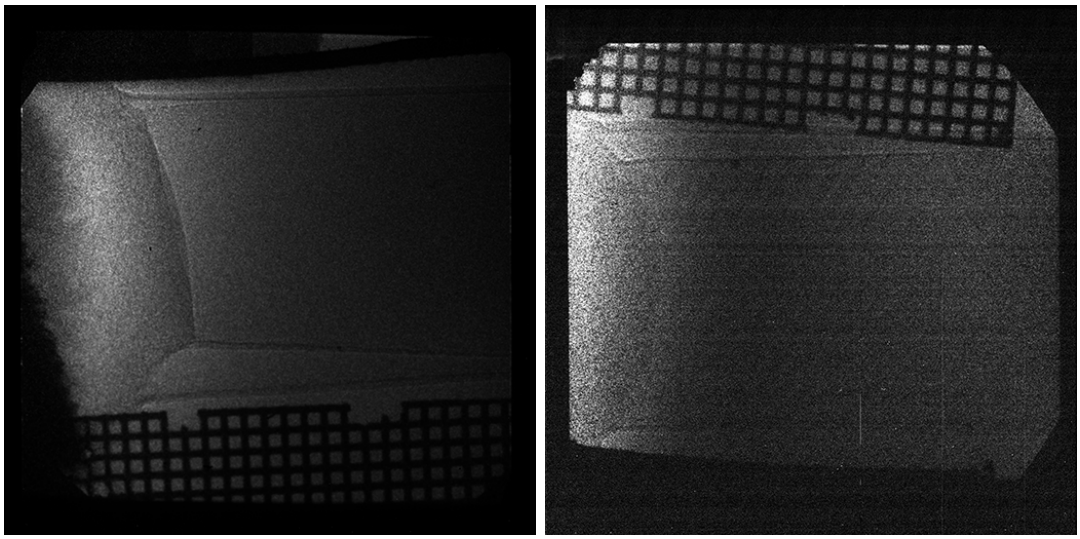

(a) TIM3c (b) TIM4

Figure C.7: RID 83101: image data

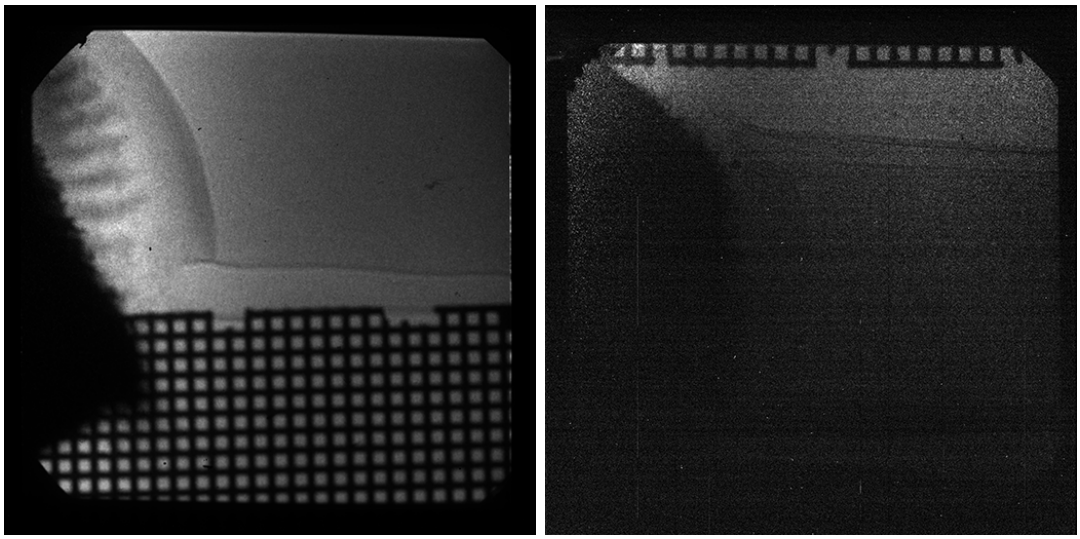

(a) TIM3c (b) TIM4

Figure C.8: RID 83103: image data

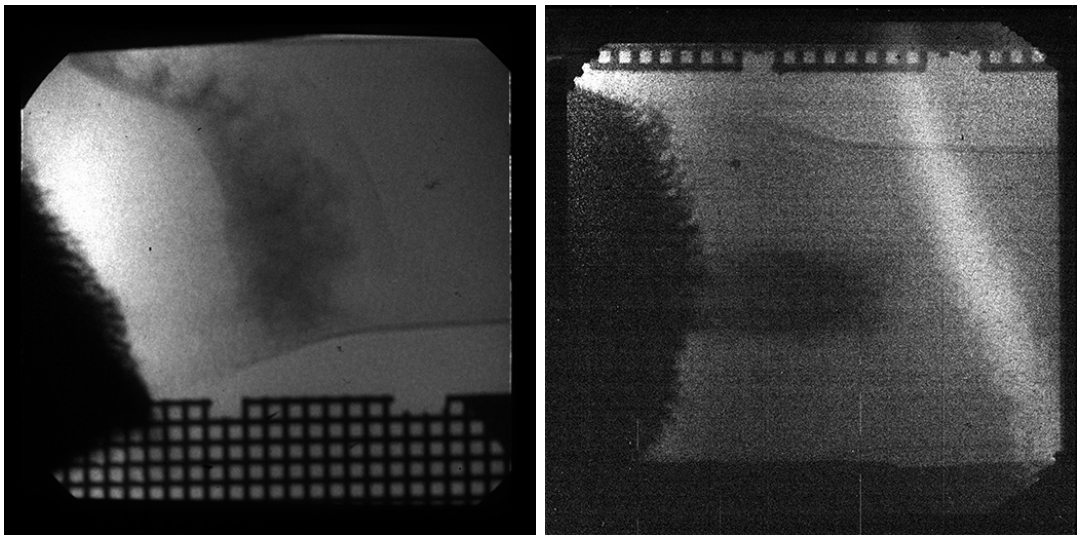

(a) TIM3c (b) TIM4

Figure C.9: RID 83104: image data

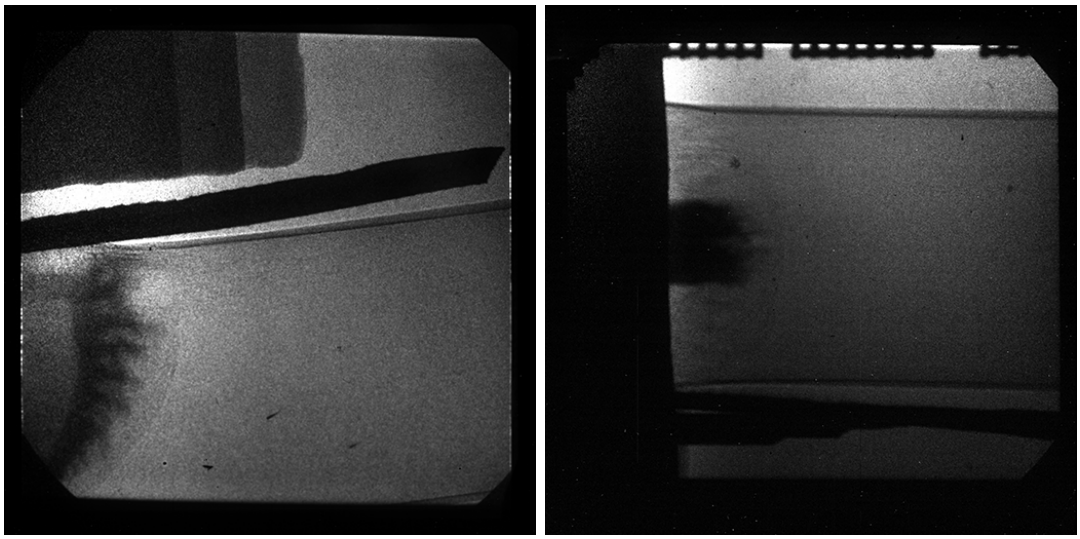

(a) TIM3c (b) TIM4

Figure C.10: RID 83105: image data

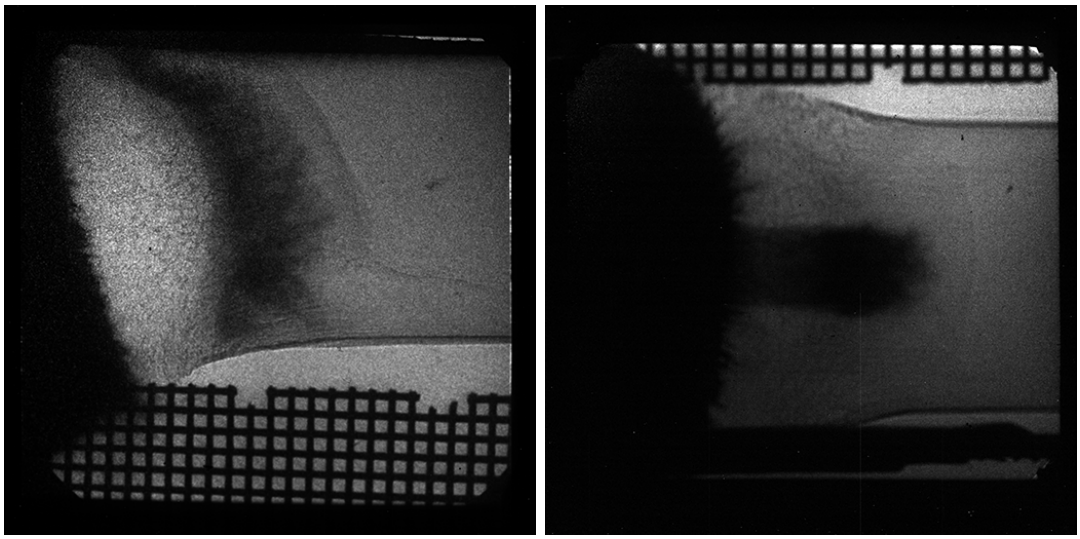

(a) TIM3c (b) TIM4

Figure C.11: RID 83106: image data

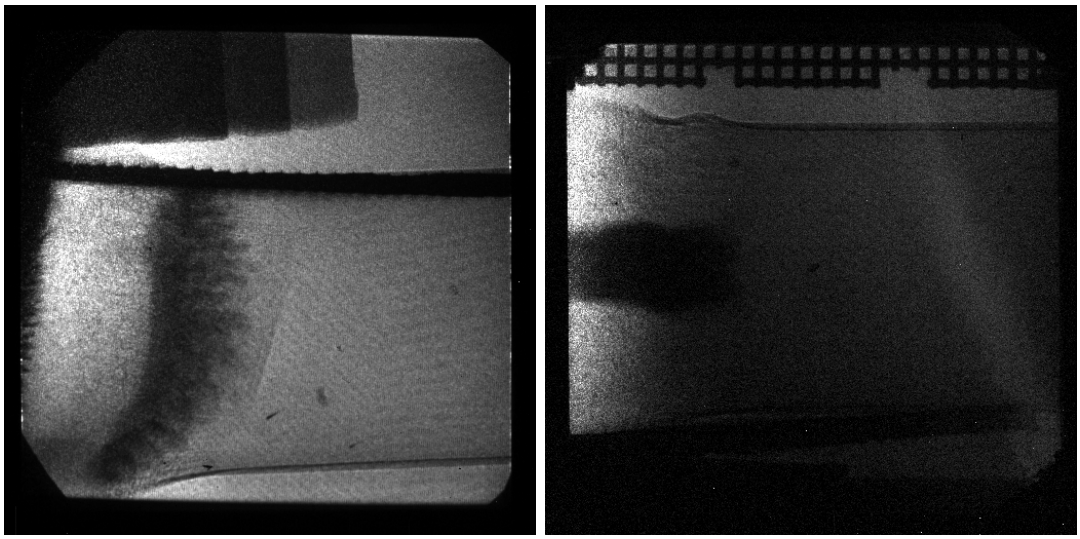

(a) TIM3c (b) TIM4

Figure C.12: RID 83107: image data

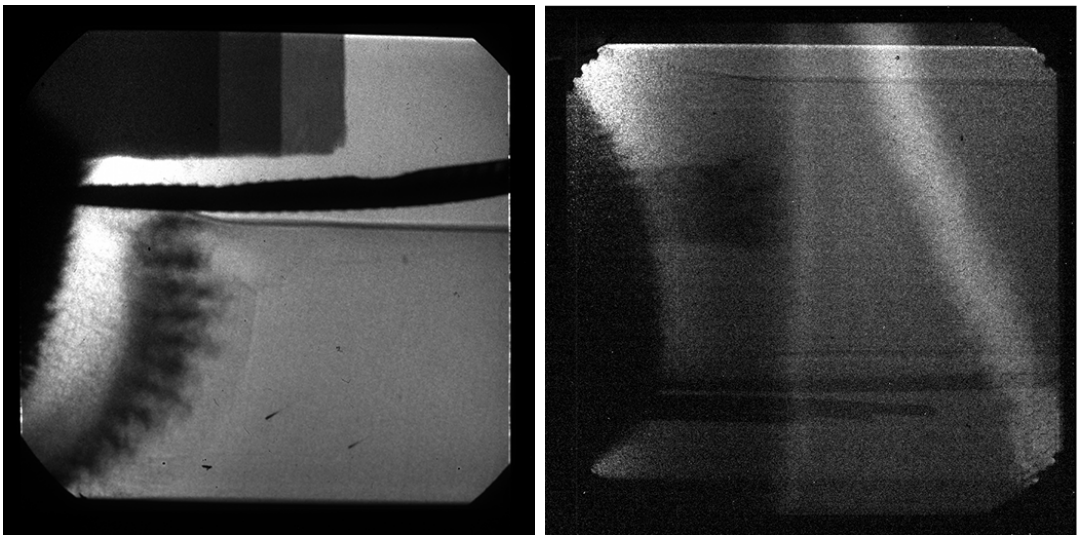

(a) TIM3c (b) TIM4

Figure C.13: RID 83108: image data

C.2 Shot Day: April 6, 2017

RID	SRF	Target ID	Target type	Primary Axis (TIM3c) Time	BL	Det.	Secondary Axis (TIM4) Time	BL	Det.	Notes
85098	60993	test target			test BL	XRFC3		test BL	XRFC5	1
85099	60987	024	low-A, 2D	30 ns	Ni10	XRFC3	30 ns	Ni10	XRFC5	
85101	62230	026	low-A, 2D	30 ns	Ni10	XRFC3	30 ns	Ni20	XRFC5	
85102	62231	023	low-A, 2D	22 ns	Ni10	XRFC3	26 ns	Ni20	XRFC5	
85103	62234	031	low-A, 3D	22 ns	Ni10	XRFC3	26 ns	Ni10	XRFC5	
85104	62239	034	high-A, 3D	22 ns	V10	XRFC3	26 ns	V10	XRFC5	
85105	62235	033	low-A, 3D	30 ns	Ni10	XRFC3	26 ns	Ni10	XRFC5	
85106	62240	038	high-A, 3D	15 ns	V10	XRFC3	19 ns	V10	XRFC5	
85107	62242	022	low-A, 2D	22 ns	Ni10	XRFC3	18 ns	Ni10	XRFC5	
85108	62243	027	low-A, 2D	35 ns	Ni10	XRFC3	39 ns	Ni10	XRFC5	
85109	62236	032	low-A, 3D	22 ns	Ni20	XRFC3	18 ns	Ni10	XRFC5	
85110	62232	001	low-A, flat	22 ns	Ni20	XRFC3	18 ns	Ni20	XRFC5	
85111	62233	004	low-A, flat	26 ns	Ni20	XRFC3	30 ns	Ni20	XRFC5	

Table C.2: Shot Log for April 6, 2017

Notes:

1. Debris test shot

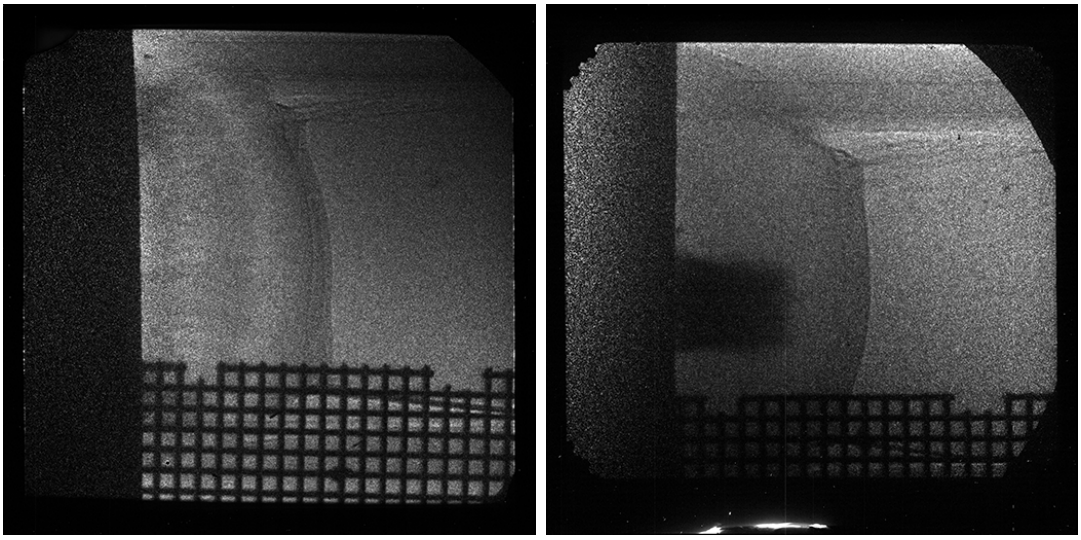

(a) TIM3c (b) TIM4

Figure C.14: RID 85099: image data

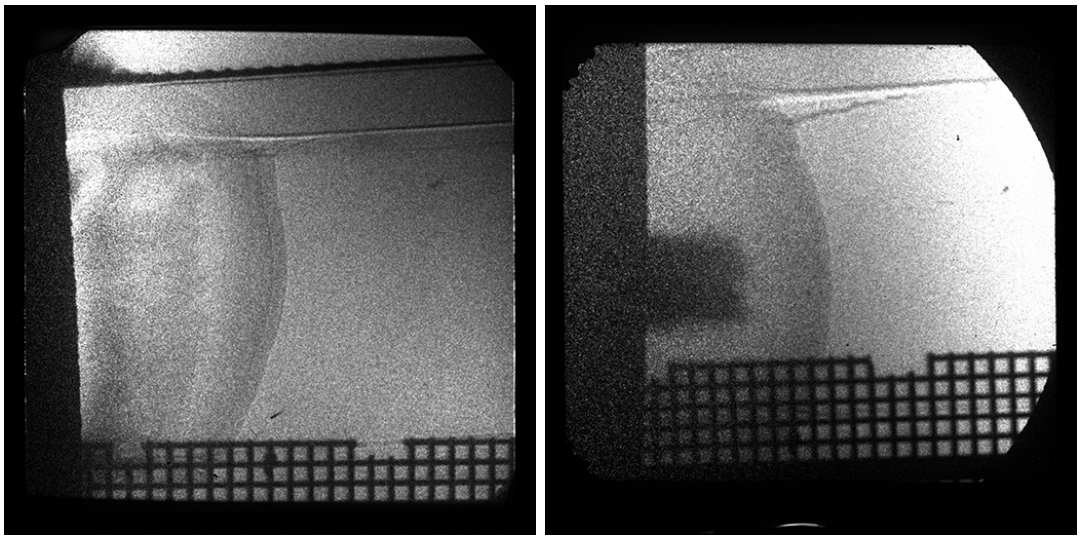

(a) TIM3c (b) TIM4

Figure C.15: RID 85101: image data

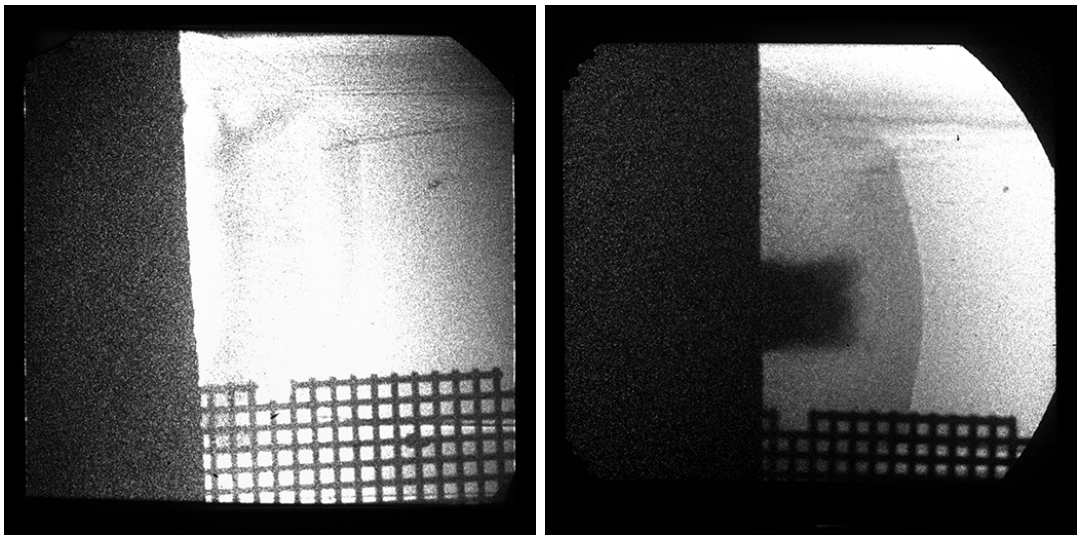

(a) TIM3c (b) TIM4

Figure C.16: RID 85102: image data

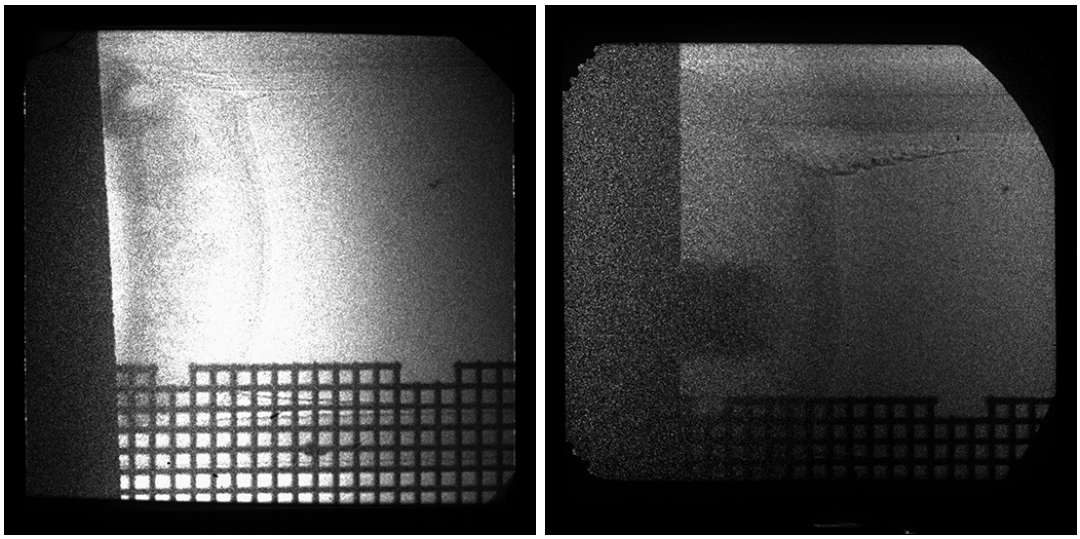

(a) TIM3c (b) TIM4

Figure C.17: RID 85103: image data

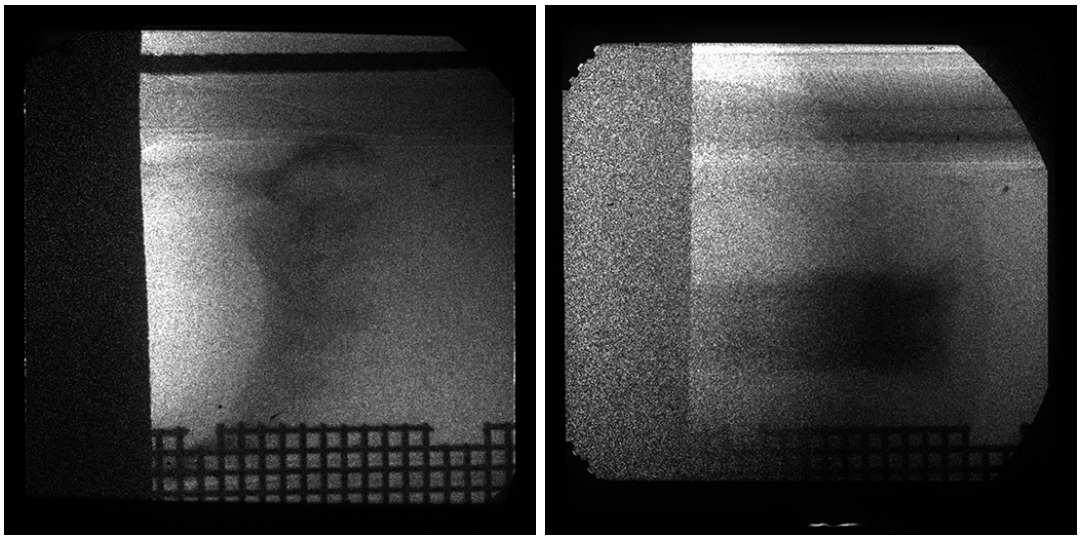

(a) TIM3c (b) TIM4

Figure C.18: RID 85104: image data

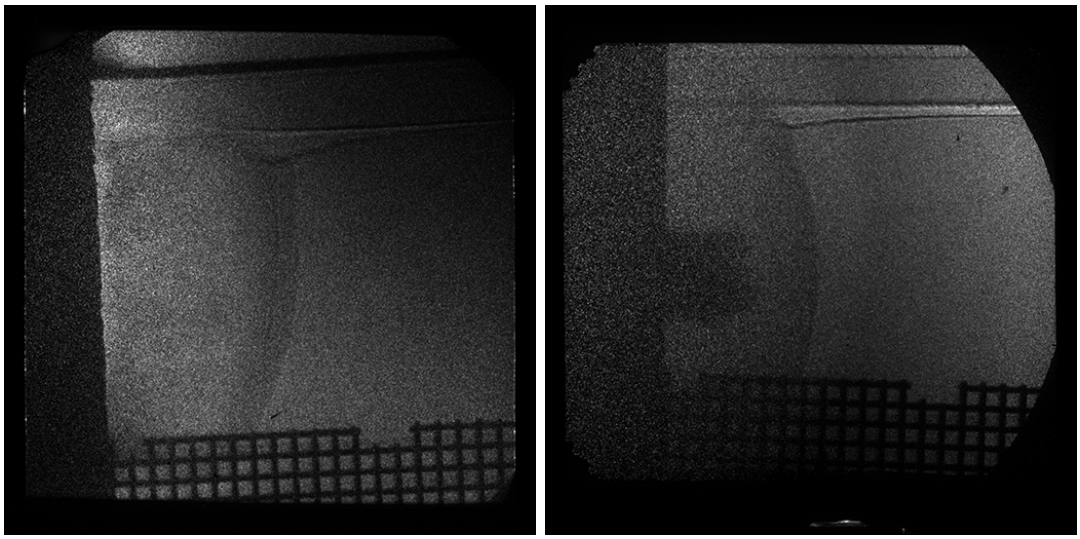

(a) TIM3c (b) TIM4

Figure C.19: RID 85105: image data

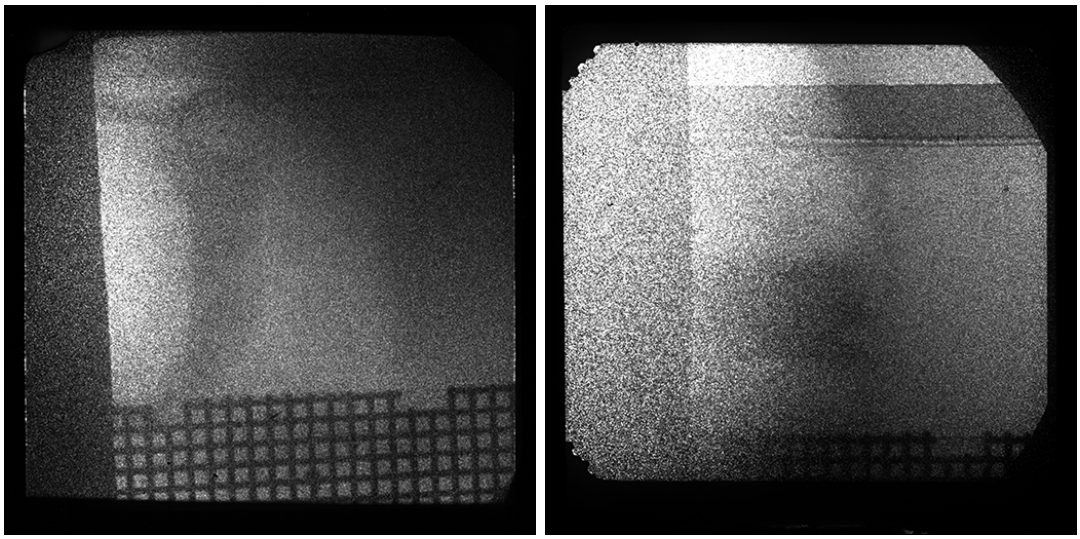

(a) TIM3c (b) TIM4

Figure C.20: RID 85106: image data

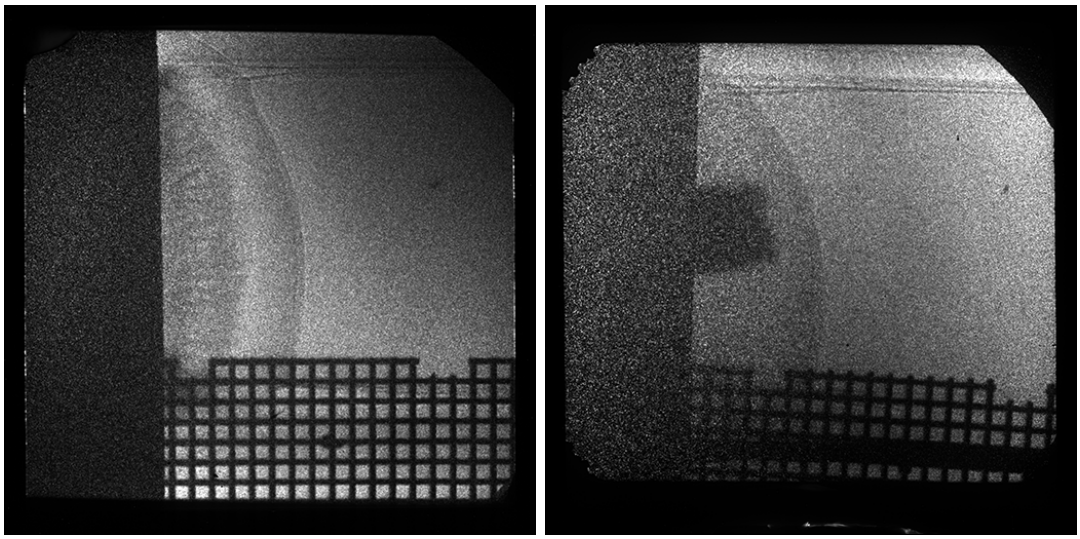

(a) TIM3c (b) TIM4

Figure C.21: RID 85107: image data

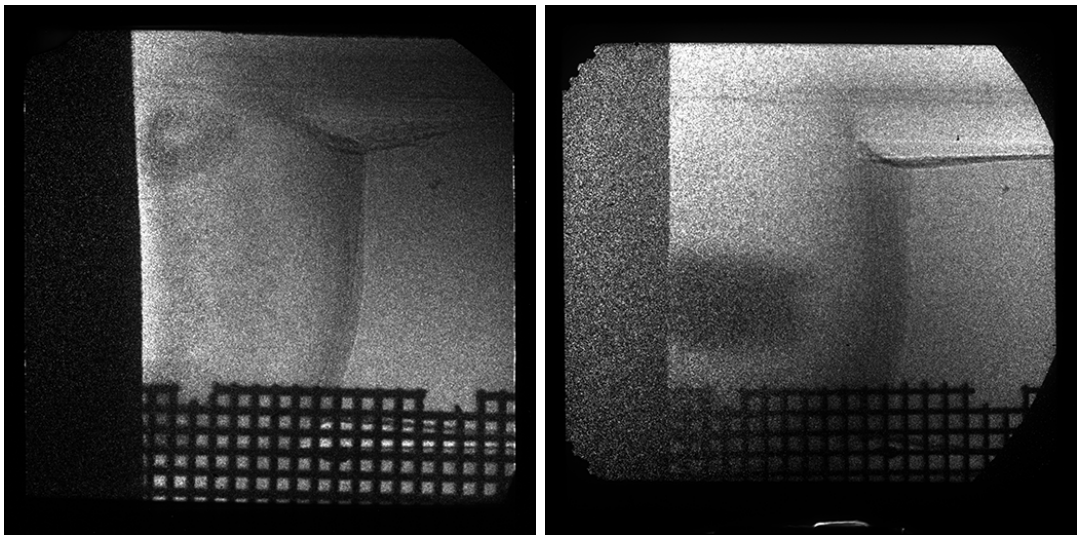

(a) TIM3c (b) TIM4

Figure C.22: RID 85108: image data

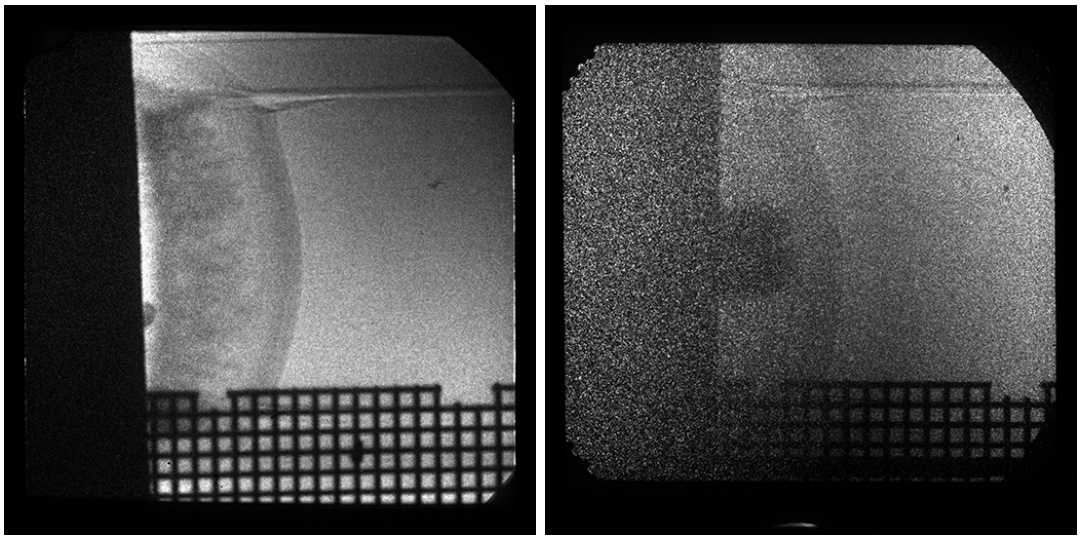

(a) TIM3c (b) TIM4

Figure C.23: RID 85109: image data

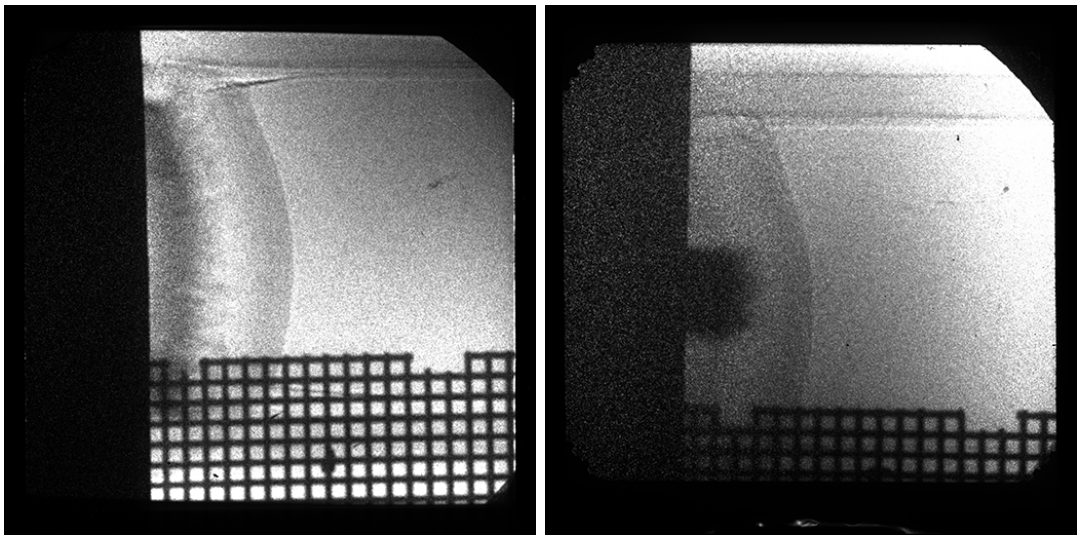

(a) TIM3c (b) TIM4

Figure C.24: RID 85110: image data

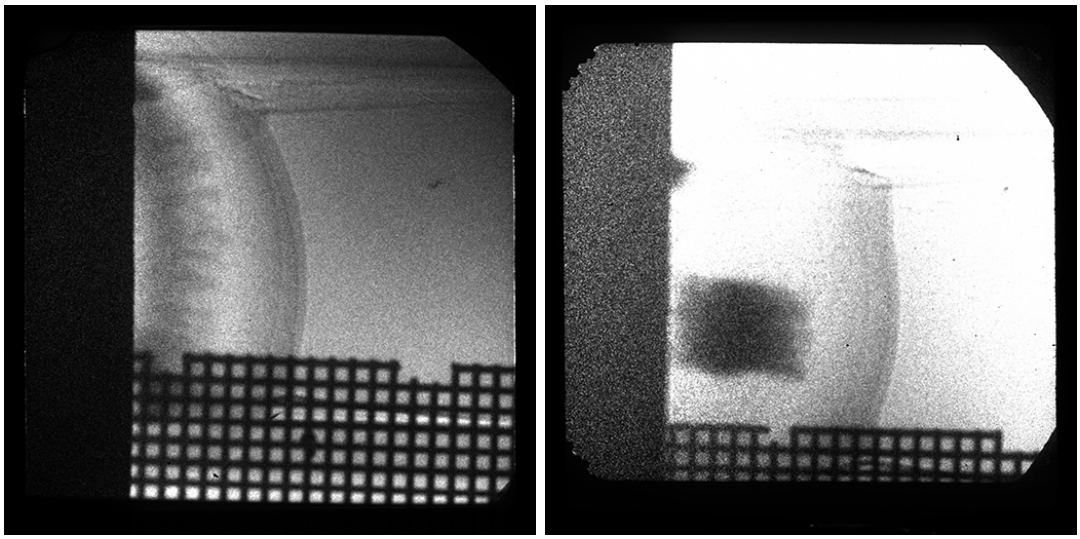

(a) TIM3c (b) TIM4

Figure C.25: RID 85111: image data

C.3 Shot Day: April 19, 2018

RID	SRF	Target ID	Target type	Primary Axis (TIM3c) Time	BL	Det.	Secondary Axis (TIM4) Time	BL	Det.	Notes
89381	65630	test target			test BL	XRFC3		test BL	XRFC4	1
89383	65631	1101	low-A, flat	30 ns	Ni20	XRFC3	39 ns	Ni20	XRFC4	
89384	67456	2104	low-A, 2D	30 ns	Ni20	XRFC3	39 ns	Ni20	XRFC4	
89385	67457	2105	low-A, 2D	39 ns	Ni10	XRFC3	43 ns	Ni10	XRFC4	
89386	67455	2103	low-A, 2D	25 ns	Ni10	XRFC3	25 ns	Ni10	XRFC4	
89387	67459	1101	low-A, flat	25 ns	Ni10	XRFC3	30 ns	Ni10	XRFC4	
89388	67458	2101	low-A, 2D	39 ns	Ni10	XRFC3	43 ns	Ni10	XRFC4	
89389	67469	1103	low-A, flat	35 ns	Ni10	XRFC3	40 ns	Ni10	XRFC4	
89390	67467	2102	low-A, 2D	35 ns	Ni20	XRFC3	40 ns	Ni20	XRFC4	
89391	67470	2107	low-A, 2D	39 ns	Ni20	XRFC3	47 ns	Ni20	XRFC4	
89392	67471	2203	high-A, 2D	30 ns	V20	XRFC3	35 ns	V20	XRFC4	
89393	67472	2202	high-A, 2D	20 ns	V20	XRFC3	25 ns	V20	XRFC4	
89394	67461	2201	high-A, 2D	15 ns	V10	XRFC3	20 ns	V10	XRFC4	

Table C.3: Shot Log for April 19, 2018

Notes:

1. Debris test shot

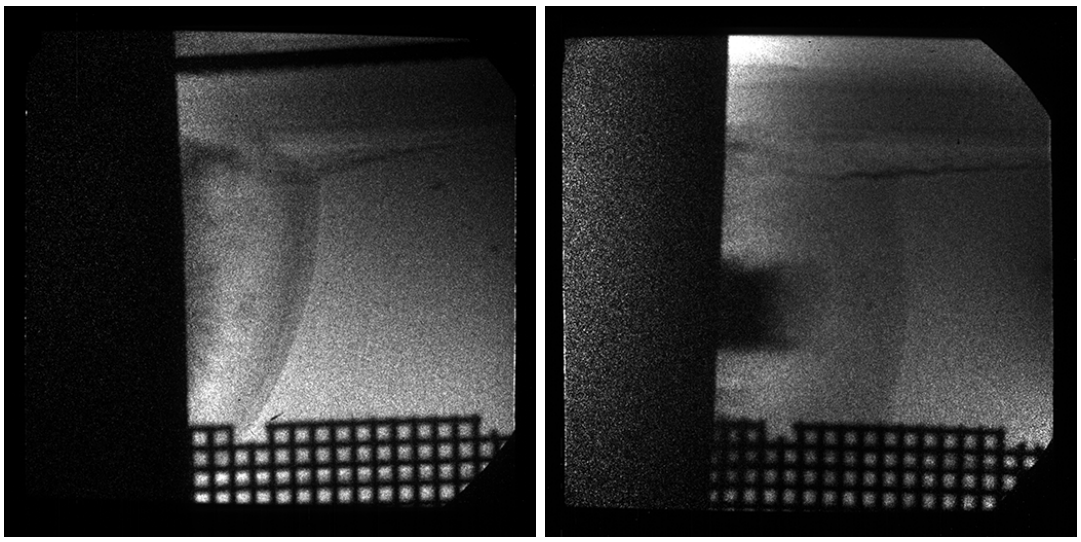

(a) TIM3c (b) TIM4

Figure C.26: RID 89383: image data

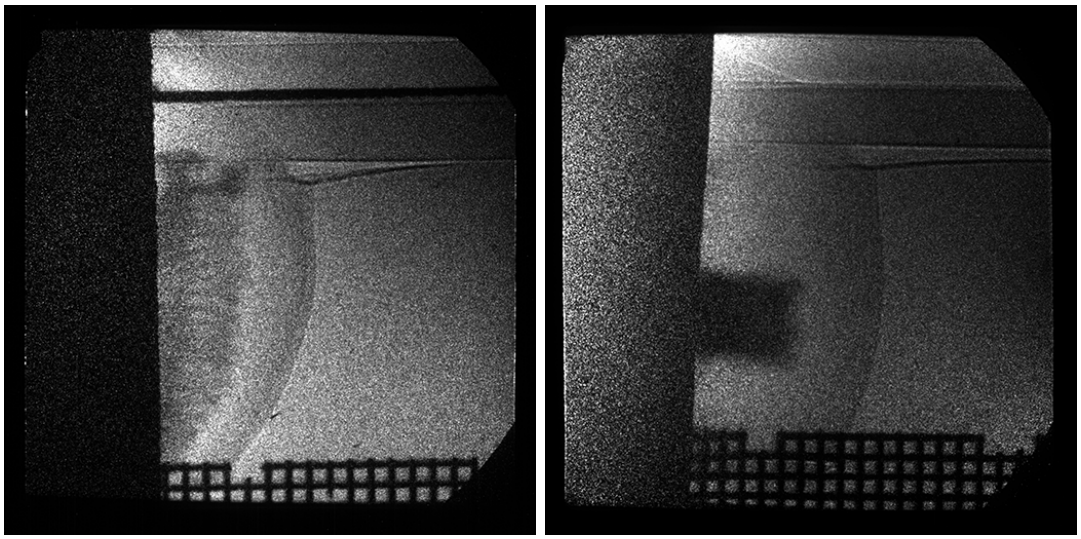

(a) TIM3c (b) TIM4

Figure C.27: RID 89384: image data

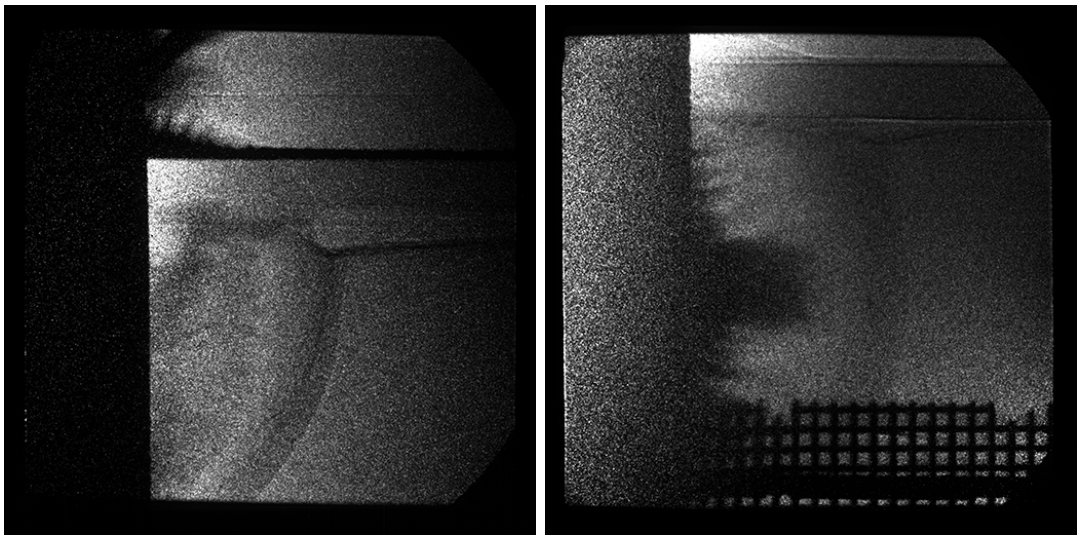

(a) TIM3c (b) TIM4

Figure C.28: RID 89385: image data

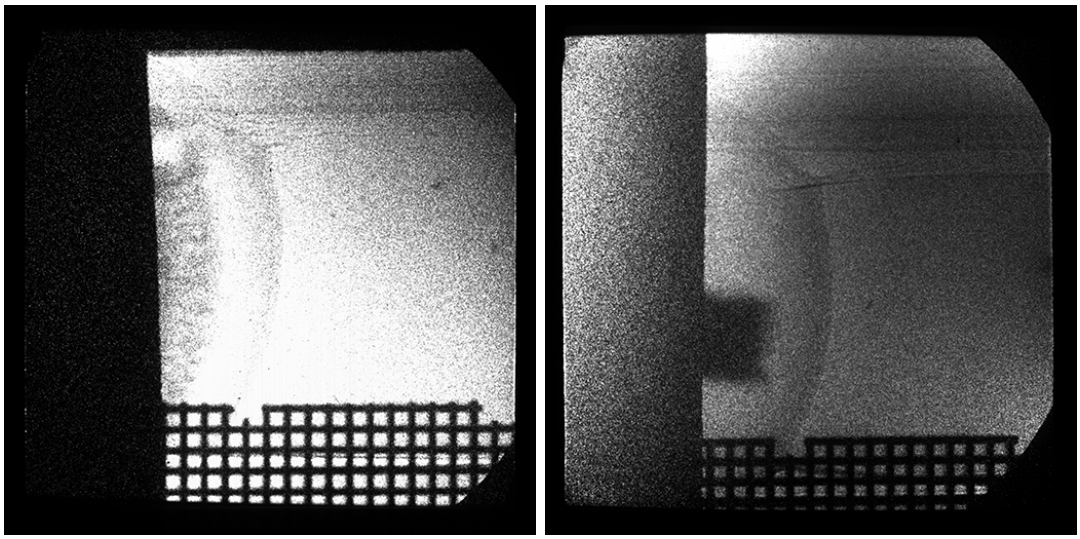

(a) TIM3c (b) TIM4

Figure C.29: RID 89386: image data

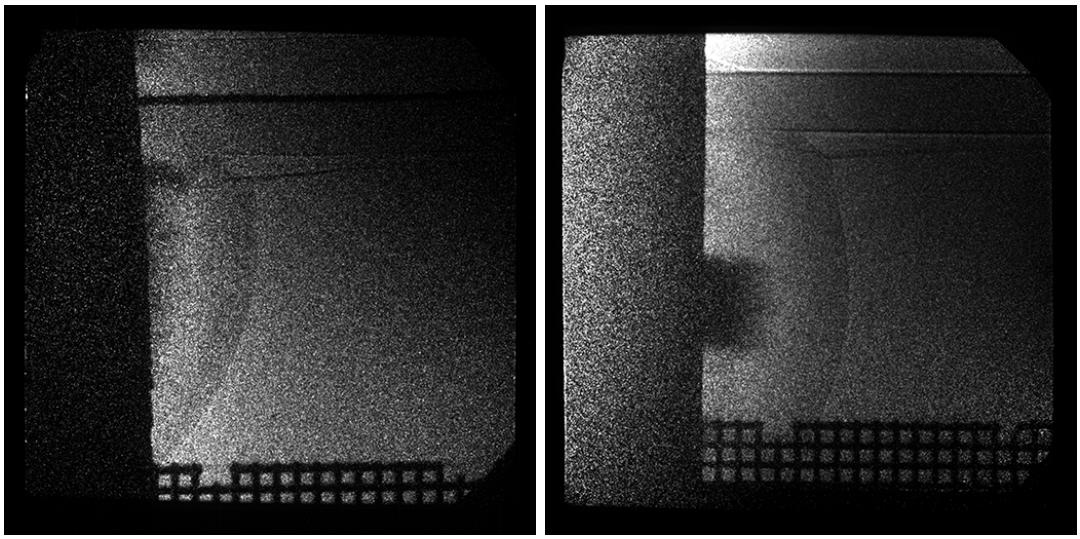

(a) TIM3c (b) TIM4

Figure C.30: RID 89387: image data

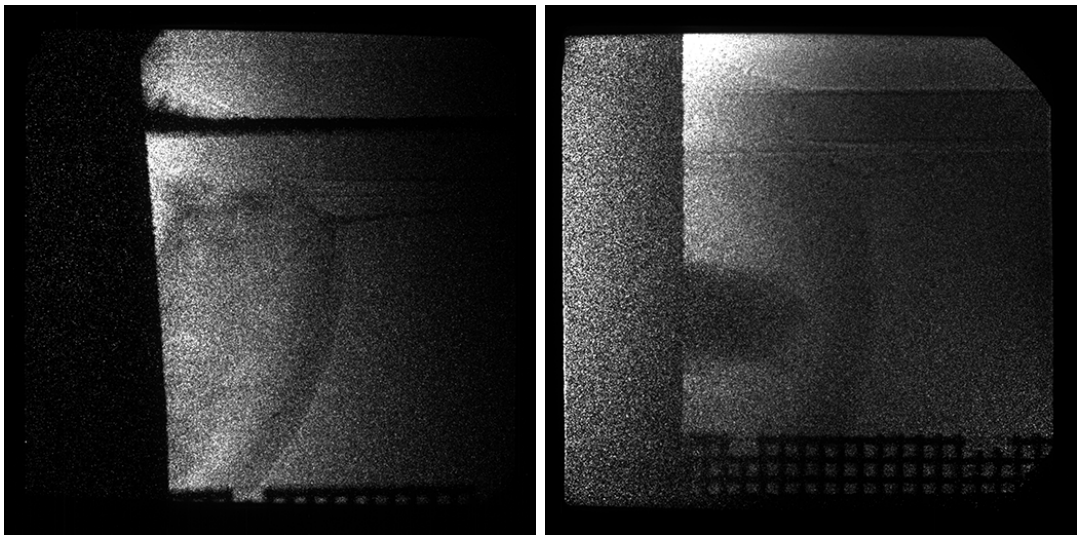

(a) TIM3c (b) TIM4

Figure C.31: RID 89388: image data

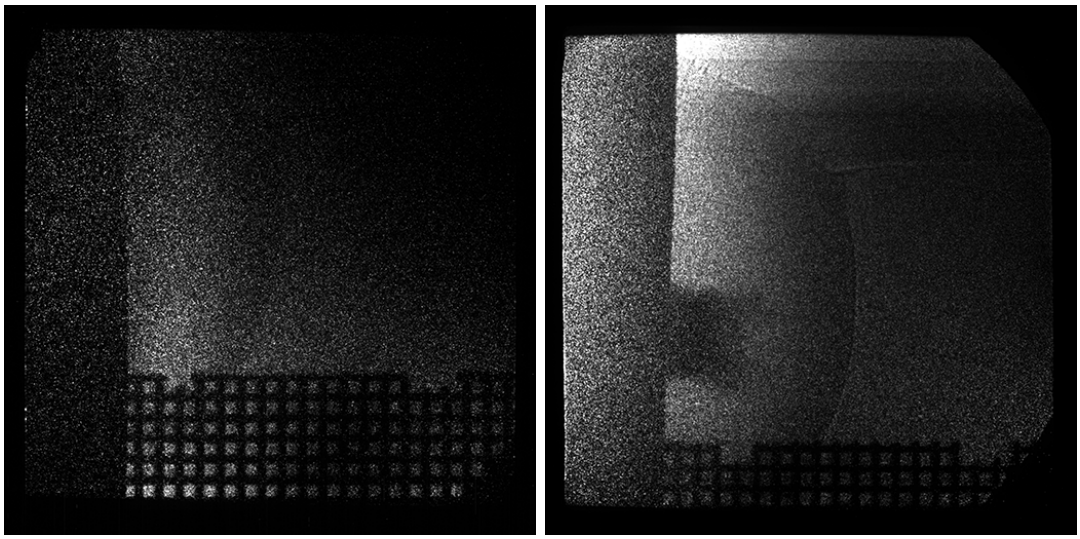

(a) TIM3c (b) TIM4

Figure C.32: RID 89389: image data

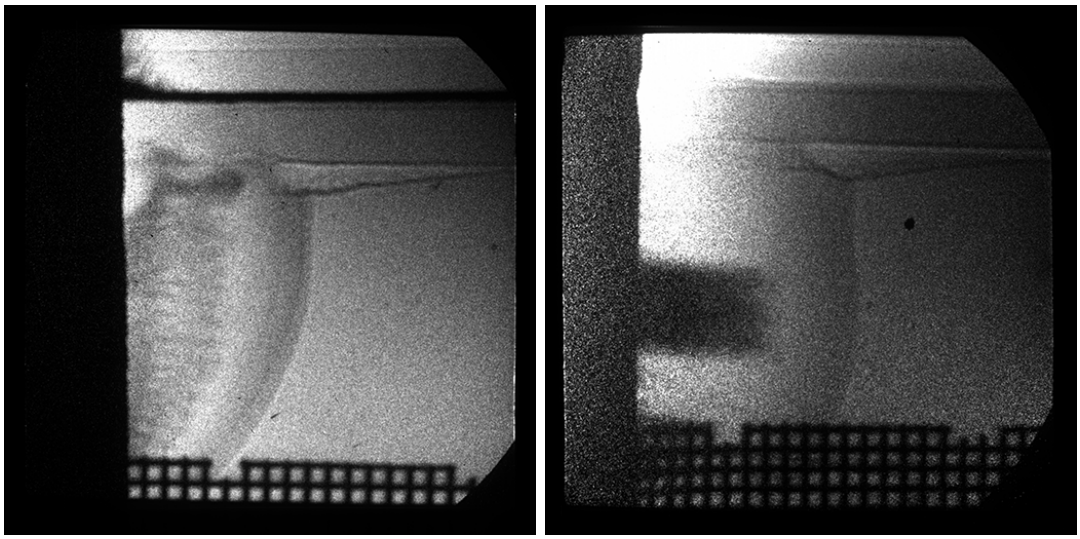

(a) TIM3c (b) TIM4

Figure C.33: RID 89390: image data

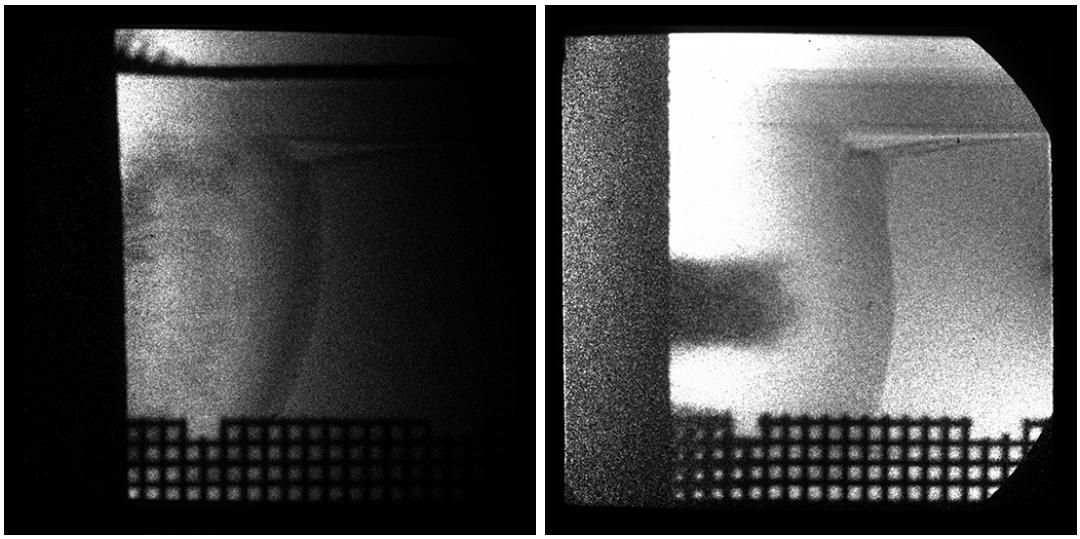

(a) TIM3c (b) TIM4

Figure C.34: RID 89391: image data

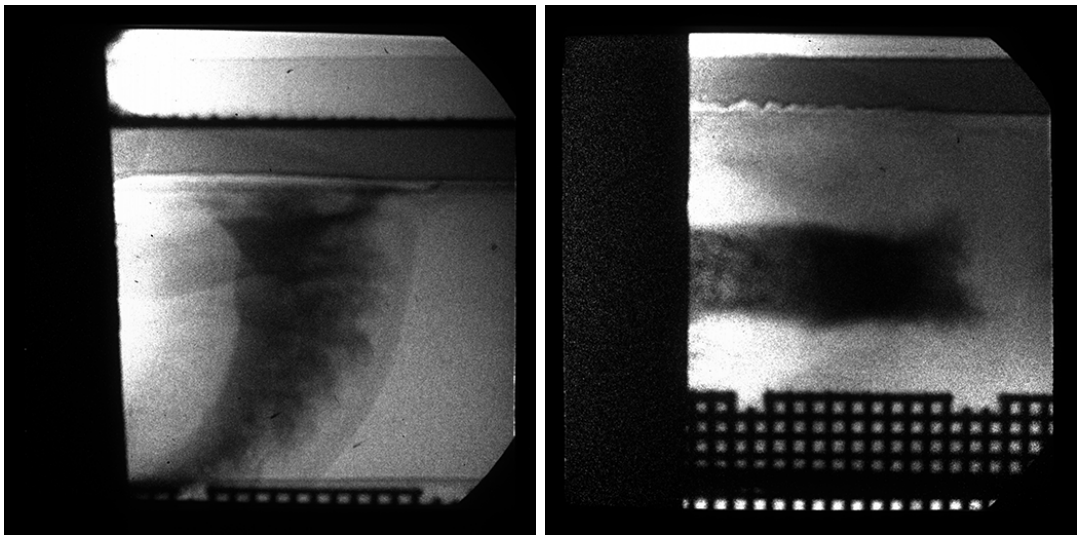

(a) TIM3c (b) TIM4

Figure C.35: RID 89392: image data

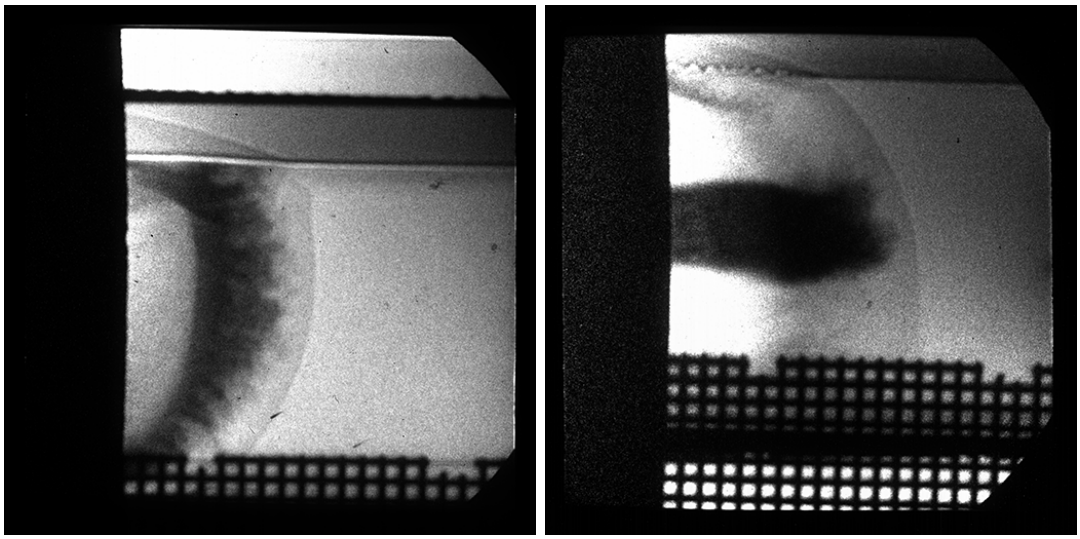

(a) TIM3c (b) TIM4

Figure C.36: RID 89393: image data

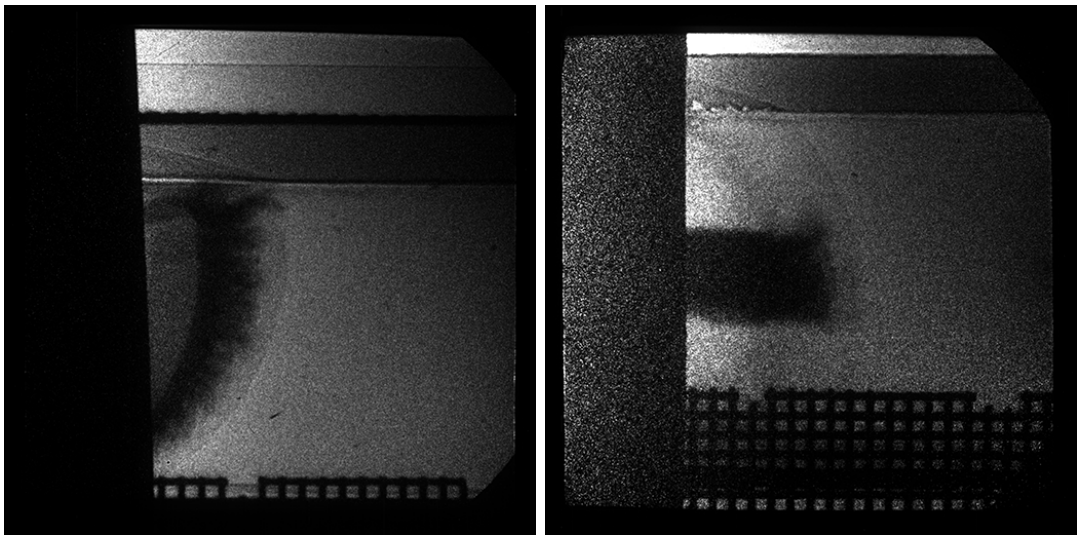

(a) TIM3c (b) TIM4

Figure C.37: RID 89394: image data

C.4 Shot Day: July 18, 2018

RID	SRF	Target ID	Target type	Primary Axis (TIM4) Time	BL	Det.	Secondary Axis (TIM3c) Time	BL	Det.	Notes
90381	68162	3108	low-A, 3D	25 ns	Ni20	film	17 ns	Ni20	film	
90382	68935	3106	low-A, 3D	30 ns	Ni20	film	35 ns	Ni10	film	
90383	68936	3104	low-A, 3D	27 ns	Ni20	film	32 ns	Ni10	film	1
90384	68947	3201	high-A, 3D	17 ns	V20	film	22 ns	V10	film	2
90385	68939	3110	low-A, 3D	20 ns	Ni20	film	N/A			3
90386	68941	2103	low-A, 2D	23 ns	Ni20	film	27 ns	Ni10	film	
90387	68937	3103	low-A, 3D	23 ns	Ni10	film	20 ns	Ni10	film	
90388	68163	3105	low-A, 3D	35 ns	Ni20	XRFC3	40 ns	Ni10	film	4
90390	68943	2104	low-A, 2D	27 ns	Ni20	XRFC3	35 ns	Ni10	film	5
90393	68938	2101	low-A, 2D	30 ns	Ni20	XRFC3	28 ns	Ni10	film	5
90394	68950	3207	high-A, 3D	17 ns	V20	XRFC3	22 ns	V10	film	5

Table C.4: Shot Log for July 18, 2018

Notes:

1. Dropped beam 59 (BL1 cluster)
2. Dropped beam 51 (BL1 cluster)
3. Dropped beam 51 (BL1 cluster); No BL2
4. Main target poorly aligned because XTVS reticle not visible; XRFC3 trigger error
5. XRFC3 performance inconsistent with prior shot days (for same bias voltage & PFM, responsivity is much lower)

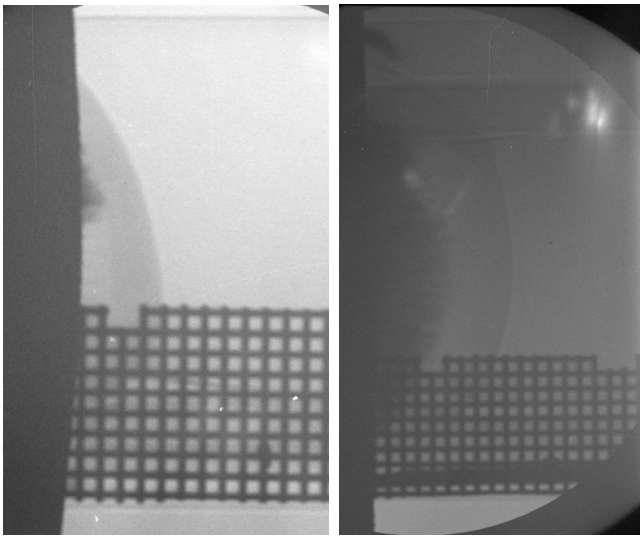

(a) TIM3c (b) TIM4

Figure C.38: RID 90381: image data

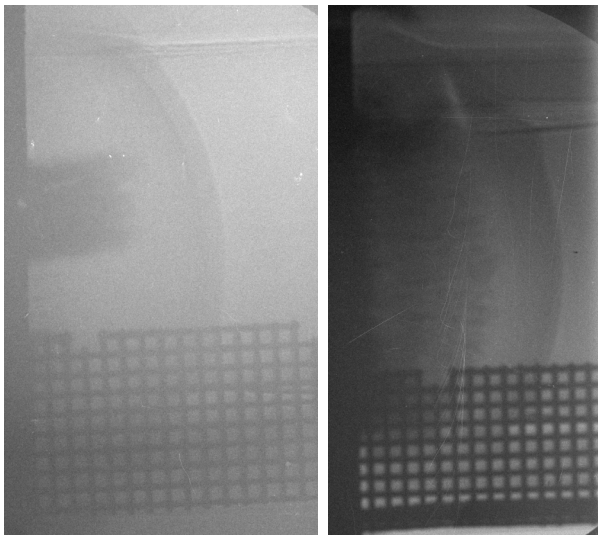

(a) TIM3c (b) TIM4

Figure C.39: RID 90382: image data

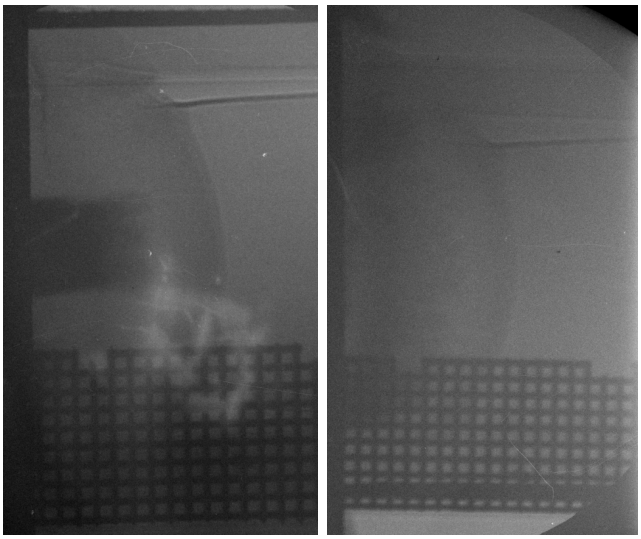

(a) TIM3c (b) TIM4

Figure C.40: RID 90383: image data

TIM4

Figure C.41: RID 90384: image data

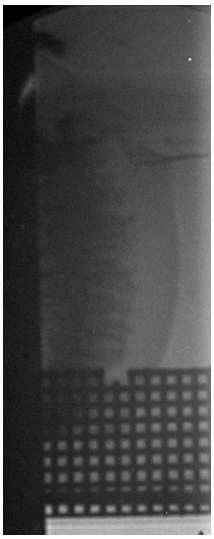

TIM4

Figure C.42: RID 90385: image data

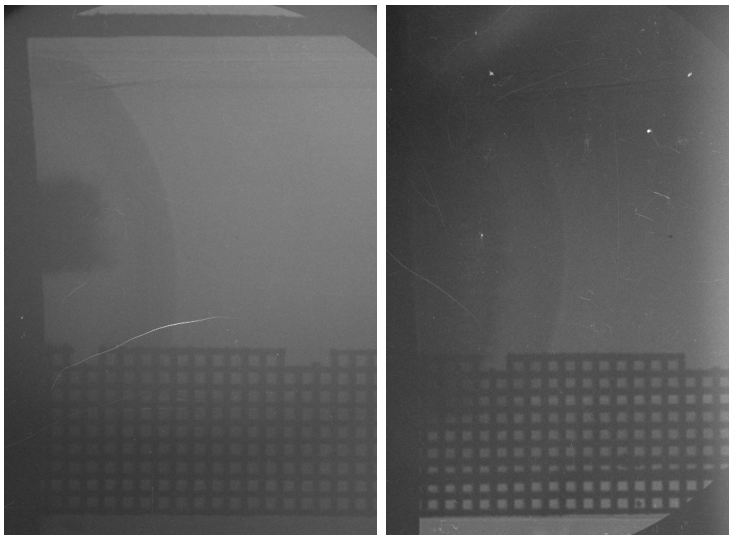

(a) TIM3c (b) TIM4

Figure C.43: RID 90386: image data

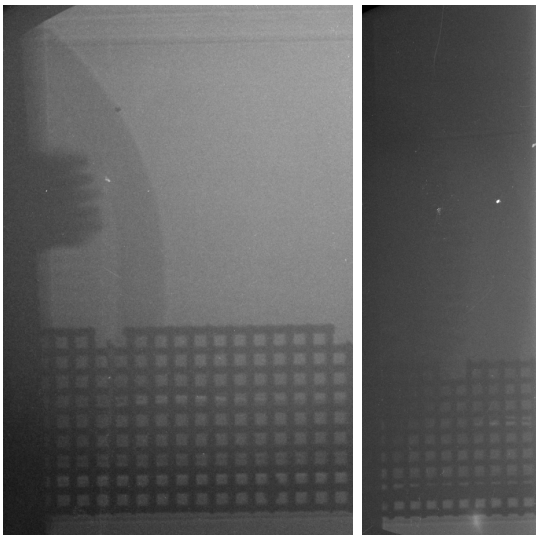

(a) TIM3c (b) TIM4

Figure C.44: RID 90387: image data

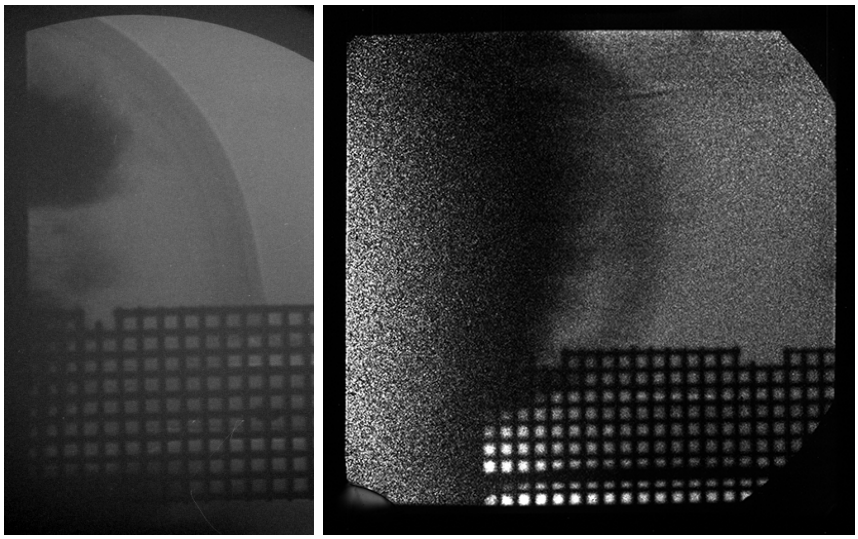

(a) TIM3c (b) TIM4

Figure C.45: RID 90388: image data

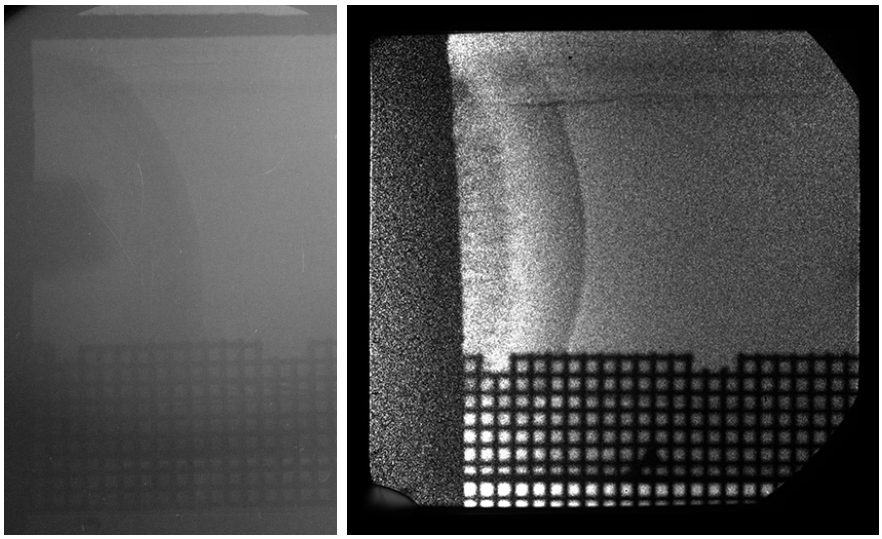

(a) TIM3c (b) TIM4

Figure C.46: RID 90390: image data

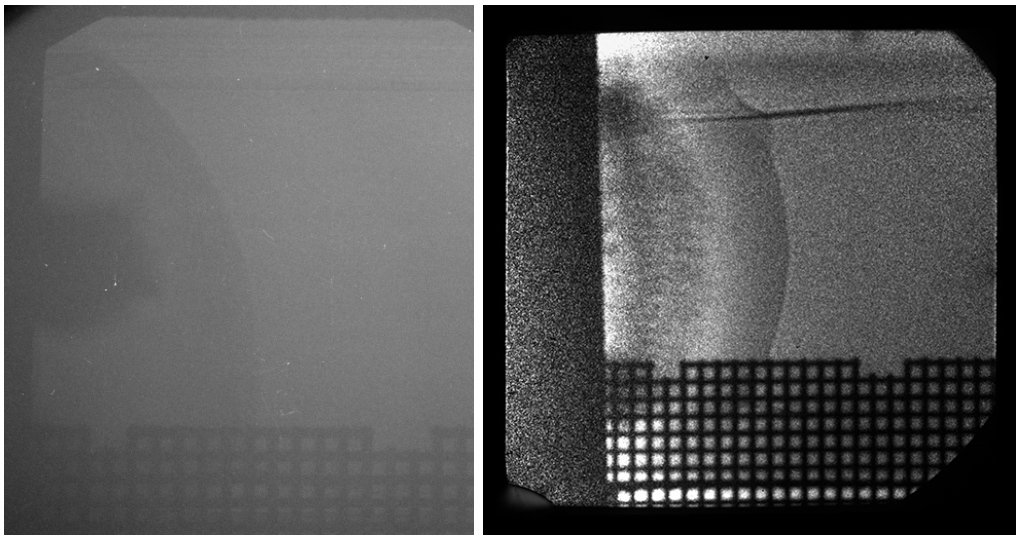

(a) TIM3c (b) TIM4

Figure C.47: RID 90393: image data

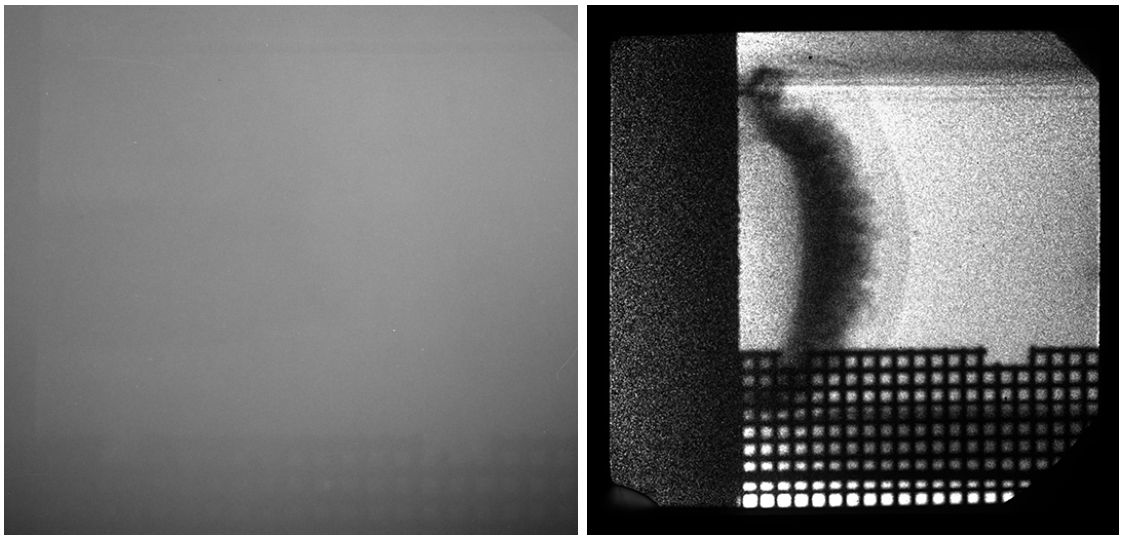

(a) TIM3c (b) TIM4

Figure C.48: RID 90394: image data

BIBLIOGRAPHY

BIBLIOGRAPHY

[1] R. Drake, *High-energy-density physics: fundamentals, inertial fusion, and experimental astrophysics*. Springer, 2 ed., 2018.

[2] C. Stolz, "The national ignition facility: The path to a carbon-free energy future," *Philosophical transactions. Series A, Mathematical, physical, and engineering sciences*, vol. 370, pp. 4115–29, 2012.

[3] `http://www.lle.rochester.edu/omega_facility/omega`. Accessed: 2019-08-02.

[4] S. Haan, "On target designing for ignition." `https://str.llnl.gov/str/Haan.html`. Accessed: 2019-08-02.

[5] B. Remington, D. Arnett, R. Drake, and H. Takabe, "Modeling astrophysical phenomena in the laboratory with intense lasers," *Science*, vol. 284, pp. 1488–1493, 1999.

[6] D. Bolster, R. Hershberger, and R. Donnelly, "Dynamic similarity, the dimensionless science," *Physics Today*, vol. 64, p. 42, 2011.

[7] D. Ryutov, R. Drake, J. Kane, E. Liang, B. Remington, and W. Wood-Vasey, "Laboratory simulation of supernova hydrodynamics," *Astrophysical Journal*, vol. 518, no. 2, pp. 821–832, 1999.

[8] R. Drake, "Center for Radiative Shock Hydrodynamics," final report DOE cooperative agreement number DE-FC5208NA28616, University of Michigan, 2014.

[9] `https://mechaengineerings.wordpress.com/2015/05/25/viscosity/`. Accessed: 2019-08-20.

[10] `https://en.wikipedia.org/wiki/Viscosity#Amorphous_materials`. Accessed: 2019-08-20.

[11] S. Braginskii, "Transport processes in a plasma," *Reviews of Plasma Physics*, vol. 1, p. 205, 1965.

[12] J. Clérouin, M. Cherfi, and G. Zérah, "The viscosity of dense plasmas mixtures," *Europhysics Letters*, vol. 42, no. 1, pp. 37–48, 1998.

[13] https://www.americangeosciences.org/critical-issues/faq/how-many-tornadoes-have-there-been-my-state-or-county. Accessed: 2019-08-19.

[14] Walter Baxter. https://commons.wikimedia.org/wiki/File:The_Corryvreckan_Whirlpool_-_geograph-2404815-by-Walter-Baxter.jpg. Accessed: 2019-08-19.

[15] L. R. C. (NASA-LaRC). https://en.wikipedia.org/wiki/File:Airplane_vortex_edit.jpg. Photo ID EL-1996-00130. Accessed: 2019-08-19.

[16] D. Tritton, *Physical Fluid Dynamics*. Clarendon Press; Oxford University Press, 2nd ed. ed., 1988.

[17] P. Kundu, I. Cohen, and D. Dowling, *Fluid mechanics*. Academic Press, 6th ed., 2016.

[18] NASA/GSFC/JPL, MISR Team. https://visibleearth.nasa.gov/view.php?id=987. Accessed: 2019-08-19.

[19] G. Taylor, "I. eddy motion in the atmosphere," *Philosophical Transactions of the Royal Society of London. Series A, Containing Papers of a Mathematical or Physical Character*, vol. 215, no. 523-537, pp. 1–26, 1915.

[20] L. Prandtl, "Report on investigation of developed turbulence," tech. rep., National Advisory Committee for Aeronautics, Washington, D.C., 1949. Translation of: "Bericht über Untersuchungen zur ausgebildeten Turbulenz," *Zeitschrift für angewandte Mathematik und Mechanik*, vol. 5, no. 2, April 1925. Report date: September 19, 1949. Report No. NACA TM 1231.

[21] Th. von Kármán, "The fundamentals of the statistical theory of turbulence," *Journal of the Aeronautical Sciences*, vol. 4, no. 4, pp. 131–138, 1937.

[22] J. Smagorinsky, "General circulation experiments with the primitive equations," *Monthly Weather Review*, vol. 91, no. 3, pp. 99–164, 1963.

[23] https://www.pinterest.com/pin/624875135526026 80. Accessed: 2019-08-02.

[24] https://www.eso.org/public/images/eso9948f. Accessed: 2019-08-02.

[25] https://str.llnl.gov/str/December04/Rathkopf.html. Accessed: 2019-08-02.

[26] J.W. Strutt (Lord Rayleigh), "Investigation of the character of the equilibrium of an incompressible heavy fluid of variable density," *Proceedings of the London Mathematical Society*, vol. s1-14, no. 1, pp. 170–177, 1883.

[27] G. Taylor, "The instability of liquid surfaces when accelerated in a direction perpendicular to their planes," *Proceedings of the London Mathematical Society A*, vol. 201, no. 1, p. 192, 1950.

[28] J. Kane, D. Arnet, B. Remington, S. Glendinning, J. Castor, R. Wallace, A. Rubenchik, and B. Fryxell, "Supernova-relevant hydrodynamic instability experiments on the Nova laser," *Astrophysical Journal*, vol. 478, p. L75, 1997.

[29] J. Knauer, R. Betti, D. Bradley, T. Boehly, T. Collins, V. Goncharov, P. McKenty, D. Meyerhofer, V. Smalyuk, C. Verdon, S. Glendinning, D. Kalantar, and R. Watt, "Single-mode, Rayleigh-Taylor growth-rate measurements on the OMEGA laser system," *Physics of Plasmas*, vol. 7, no. 1, pp. 338–345, 2000.

[30] R. Morgan, R. Aure, J. Stockero, and J. Greenough, "On the late-time growth of the two-dimensional Richtmyer-Meshkov instability in shock tube experiments," *Journal of Fluid Mechanics*, vol. 712, pp. 354–383, 2012.

[31] R. Richtmyer, "Taylor instability in shock acceleration of compressible fluids," *Communications on Pure and Applied Math*, vol. 13, p. 297, 1960.

[32] E. Meshkov, "Instability of the interface of two gases accelerated by a shock wave," *USSR Fluid Dynamics*, vol. 4, p. 101, 1969.

[33] K. Meyer and P. Blewett, "Numerical investigation of the stability of a shock accelerated interface between two fluids," *Physics of Fluids*, vol. 15, p. 753, 1972.

[34] `https://strangesounds.org/2015/12/like-a-tsunami-in-the-sky-`kelvin-helmholtz-clouds-engulf-the-sky-of-snowbasin-utah.html. Accessed: 2019-08-02.

[35] K. Gill. `https://www.flickr.com/photos/kevinmgill/28062689029/`. Accessed: 2019-08-18.

[36] Thomson William (Lord Kelvin, "XLVI. hydrokinetic solutions and observations," *The London, Edinburgh, and Dublin Philosophical Magazine and Journal of Science*, vol. 42, no. 281, pp. 362–377, 1871.

[37] Helmholtz, "XLIII. on discontinuous movements of fluids," *The London, Edinburgh, and Dublin Philosophical Magazine and Journal of Science*, vol. 36, no. 244, p. 337346, 1868.

[38] S. Chandrasekhar, *Hydrodynamic and hydromagnetic stability*. International series of monographs on physics (Oxford, England), Clarendon Press, 1961.

[39] P. Philippi, K. Mattila, L. Hegele, and D. Siebert, "Kinetic projection and stability in lattice-boltzmann schemes," in *CILAMCE Proceedings*, 11 2015.

[40] D. M. V. Martinez, E. B. C. Schettini, and J. H. Silvestrini, "The influence of stable stratification on the transition to turbulence in a temporal mixing layer," *Journal of the Brazilian Society of Mechanical Sciences and Engineering*, vol. 28, pp. 242–252, 2006.

[41] J. Larsen and S. Lane, "HYADES–a plasma hydrodynamics code for dense plasma studies," *Journal of Quantitative Spectroscopy and Radiative Transfer*, vol. 51, pp. 179–186, 2002.

[42] G. Malamud, L. Elgin, T. Handy, C. Huntington, R. Drake, D. Shvarts, A. Shimony, and C. Kuranz, "Design of a single-mode Rayleigh-Taylor instability experiment in the highly nonlinear regime," *High Energy Density Physics*, vol. 32, pp. 18–30, 2019.

[43] G. Ben-Dor, O. Igra, and T. Elperin, *Handbook of Shock Waves*, vol. 2. Academic Press, 2001.

[44] D. Layzer, "On the instability of superposed fluids in a gravitational field," *Astrophysical Journal*, vol. 122, no. 1, pp. 1–12, 1955.

[45] V. Goncharov, "Analytical model of nonlinear, single-mode, classical Rayleigh-Taylor instability at arbitrary Atwood numbers," *Physical Review Letters*, vol. 88, no. 13, p. 134502, 2002.

[46] Y. Srebro, Y. Elbaz, O. Sadot, L. Arazi, and D. Schvarts, "A general Buoyancy-drag model for the evolution of the Rayleigh-Taylor and Richtmyer-Meshkov instabilities," *Laser and Particle Beams*, vol. 21, no. 3, pp. 347–353, 2003.

[47] G. Dimonte, "Spanwise homogeneous buoyancy-drag model for Rayleigh-Taylor mixing and experimental evaluation," *Physics of Plasmas*, vol. 7, no. 6, pp. 2255–2269, 2000.

[48] D. Oron, L. Arazi, D. Kartoon, A. Rikanati, U. Alon, and D. Shvarts, "Dimensionality dependence of the Rayleigh-Taylor and Richtmyer-Meshkov instability late-time scaling laws," *Physics of Plasmas*, vol. 8, no. 6, pp. 2883–2889, 2001.

[49] P. Ramaprabhu, D. Dimonte, P. Woodward, C. Fryer, G. Rockefeller, K. Muthuraman, P.-H. Lin, and J. Jayaraj, "The late-time dynamics of the single-mode Rayleigh-Taylor instability," *Physics of Fluids*, vol. 24, pp. 074107–1–21, 2012.

[50] S.-I. Sohn, "Simple potential-flow model of Rayleigh-Taylor and Richtmyer-Meshkov instabilities for all density ratios," *Physical Review E*, vol. 67, p. 026301, 2003.

[51] S. Abarzhi, K. Nishiharab, and J. Glimm, "Rayleigh-Taylor and Richtmyer-Meshkov instabilities for fluids with a finite density ratio," *Physical Review Letters A*, vol. 317, pp. 470–476, 2003.

[52] K. Mikaelian, "Explicit expressions for the evolution of single-mode Rayleigh-Taylor and Richtmyer-Meshkov instabilities at arbitrary atwood numbers," *Physical Review E*, vol. 67, p. 026319, 2003.

[53] Y. Zhou, "Rayleigh-Taylor and Richtmyer-Meshkov instability induced flow, turbulence, and mixing. I," *Physics Reports*, vol. 720-722, pp. 1–136, 2017.

[54] Y. Zhou, "Rayleigh-Taylor and Richtmyer-Meshkov instability induced flow, turbulence, and mixing. II," *Physics Reports*, vol. 723-725, pp. 1–160, 2017.

[55] R. Nourgaliev and T. Theofanous, "High-fidelity interface tracking in compressible flows: Unlimited anchored adaptive level set," *Journal of Computational Physics*, vol. 224, pp. 836–866, 2007.

[56] S. Haan, "Onset of nonlinear saturation for Rayleigh-Taylor growth in the presence of a full spectrum of modes," *Physical Review A*, vol. 39, pp. 5812–5825, 1989.

[57] D. Sharp, "An overview of Rayleigh-Taylor instability," *Physica D: Nonlinear Phenomena*, vol. 12, pp. 3–10, 1984.

[58] D. Ofer and D. Shvarts, "Mode coupling in nonlinear Rayleigh-Taylor instability," *Physics of Fluids B*, vol. 4, p. 3549, 1992.

[59] D. Ofer, U. Alon, D. Shvarts, R. L. McCrory, and C. P. Verdon, "Modal model for the nonlinear multimode Rayleigh-Taylor instability," *Physics of Plasmas*, vol. 3, no. 8, pp. 3073–3090, 1996.

[60] D. Shvarts, "Nonlinear evolution of multimode Rayleigh-Taylor instability in two and three dimensions," *Physics of Plasmas*, vol. 2, p. 2465, 1995.

[61] U. Alon, D. Shvarts, and D. Mukamel, "Scale-invariant regime in Rayleigh-Taylor bubble-front dynamics," *Physical Review Letters E*, vol. 48, no. 2, 1995.

[62] A. Miles, "Bubble merger model for the nonlinear Rayleigh-Taylor instability driven by a strong blast wave," *Physics of Plasmas*, vol. 11, no. 11, p. 5140, 2004.

[63] D. Livescu, J. Ristorcelli, R. Gore, S. Dean, W. Cabot, and A. Cook, "High-Reynolds number Rayleigh-Taylor turbulence," *Journal of Turbulence*, vol. 10, no. 13, pp. 1–32, 2009.

[64] D. Youngs, "Three-dimensional numerical simulation of turbulent mixing by Rayleigh-Taylor instability," *Physics of Fluids A: Fluid Dynamics*, vol. 3, no. 5, pp. 1312–1320, 1991.

[65] W. Cabot and A. Cook, "Reynolds number effects on Rayleigh-Taylor instability with possible implications for type-1a supernovae," *Nature Physics*, vol. 2, pp. 562–568, 2006.

[66] J. Ristorcelli and T. Clark, "Rayleigh-Taylor turbulence: Self-similar analysis and direct numerical simulations," *Journal of Fluid Mechanics*, vol. 507, pp. 213–253, 2004.

[67] A. Cook, W. Cabot, and P. Miller, "The mixing transition in Rayleigh-Taylor instability," *Journal of Fluid Mechanics*, vol. 511, pp. 333–362, 2004.

[68] G. Dimonte, D. Youngs, A. Dimits, S. Weber, M. Marinak, S. Wunsch, C. Garasi, A. Robinson, M. J. Andrews, P. Ramaprabhu, A. Calder, B. Fryxell, J. Biello, L. Dursi, P. MacNeice, K. Olson, P. Ricker, R. Rosner, F. Timmes, H. Tufo, Y.-N. Young, and M. Zingale, "A comparative study of the turbulent Rayleigh-Taylor instability using high-resolution three-dimensional numerical simulations: The Alpha-Group collaboration," *Physics of Fluids*, vol. 16, no. 5, p. 1668, 2004.

[69] A. Shimony, G. Malamud, and D. Shvarts, "Density ratio and entrainment effects on asymptotic Rayleigh-Taylor instability," *Journal of Fluids Engineering*, vol. 140, pp. 050906–1–8, 2018.

[70] P. Dimotakis, "The mixing transition in turbulent flows," *Journal of Fluid Mechanics*, vol. 409, pp. 69–98, 2000.

[71] H. Tennekes and J. Lumley, *A first course in turbulence*. The MIT Press, 1972.

[72] Y. Zhou, B. Remington, H. Robey, A. Cook, S. Gendinning, A. Dimits, A. Buckingham, G. Zimmerman, E. Burke, T. Peyser, W. Cabot, and D. Eliason, "Progress in understanding turbulent mixing induced by Rayleigh-Taylor and Richtmyer-Meshkov instabilities," *Physics of Plasmas*, vol. 10, no. 5, pp. 1883–1896, 2003.

[73] Y. Zhou, "Unification and extension of the similarity scaling criteria and mixing transition for studying astrophysics using high energy density laboratory experiments or numerical simulations," *Physics of Plasmas*, vol. 14, p. 082701, 2007.

[74] D. Youngs, "Rayleigh-Taylor mixing: direct numerical simulation and implicit large eddy simulation," *Physica Scripta*, vol. 92, p. 074006, 2017.

[75] A. Miles, B. Blue, M. Edwards, J. Greenough, J. Hansen, H. Robey, R. Drake, C. Kuranz, and D. Leibrandt, "Transition to turbulence and effect of initial conditions on three-dimensional compressible mixing in planar blast-wave-driven systems," *Physics of Plasmas*, vol. 12, no. 5, p. 056317, 2005.

[76] R. Morgan, W. Cabot, J. Greenough, and J. Jacobs, "Rarefaction-driven Rayleigh-Taylor instability. part 2. experiments and simulations in the nonlinear regime," *Journal of Fluid Mechanics*, vol. 838, pp. 320–355, 2018.

[77] J. Wilkinson and J. Jacobs, "Experimental study of the single-mode three-dimensional Rayleigh-Taylor instability," *Physics of Fluids*, vol. 19, no. 12, p. 124102, 2007.

[78] R. Betti and J. Sanz, "Bubble acceleration in the ablative Rayleigh-Taylor instability," *Physical Review Letters*, vol. 97, pp. 205002–1–4, 2006.

[79] T. Wei and D. Livescu, "Late-time quadratic growth in single-mode Rayleigh-Taylor instability," *Physical Review E*, vol. 86, p. 046405, 2012.

[80] J. Waddell, C. Niederhaus, and J. Jacobs, "Experimental study of Rayleigh-Taylor instability: Low atwood number liquid systems with single-mode initial perturbations," *Physics of Fluids*, vol. 13, no. 5, pp. 1263–1273, 2001.

[81] P. Linden, J. Redondo, and D. Youngs, "Molecular mixing in Rayleigh-Taylor instability," *Journal of Fluid Mechanics*, vol. 265, pp. 97–124, 1994.

[82] N. Mueschke, M. Andrews, and O. Schilling, "Experimental characterization of initial conditions and spatio-temporal evolution of a small-Atwood-number Rayleigh-Taylor mixing layer," *Journal of Fluid Mechanics*, vol. 567, pp. 27–63, 2006.

[83] M. Andrews and S. Dalziel, "Small Atwood number Rayleigh-Taylor experiments," *Philosophical Transactions of the Royal Society A*, vol. 368, pp. 1663–79, 2010.

[84] R. Morgan, O. Likhachev, and J. Jacobs, "Rarefaction-driven Rayleigh-Taylor instability. part 1. diffuse-interface linear stability measurements and theory," *Journal of Fluid Mechanics*, vol. 791, pp. 34–60, 2016.

[85] K. Mikaelian, "Reshocks, rarefactions, and the generalized Layzer model for hydrodynamic instabilities," *Physics of Fluids*, vol. 21, p. 024103, 2009.

[86] B. Remington, S. Haan, S. Glendinning, J. Kilkenny, D. Munro, and R. Wallace, "Large growth, planar Rayleigh-Taylor experiments on Nova," *Physics of Fluids B*, vol. 4, no. 4, p. 967, 1992.

[87] J. Kilkenny, S. Glendinning, S. Haan, B. Hammel, J. Lindl, D. Munro, B. Remington, S. Weber, J. Knauer, and C. Verdon, "A review of the ablative stabilization of the Rayleigh-Taylor instability in regimes relevant to inertial confinement fusion," *Physics of Plasmas*, vol. 1, no. 5, pp. 1379–1389, 1994.

[88] M. Marinak, B. Remington, S. Weber, R. Tipton, S. Haan, K. Budil, O. Landen, J. Kilkenny, and R. Wallace, "Three-dimensional single mode Rayleigh-Taylor experiments on Nova," *Physical Review Letters*, vol. 75, no. 20, p. 3677, 1995.

[89] B. Remington, S. Weber, M. Marinak, S. Haan, J. Kilkenny, R. Wallace, and G. Dimonte, "Single-mode and multimode Rayleigh-Taylor experiments on Nova," *Physics of Plasmas*, vol. 2, no. 1, pp. 241–255, 1995.

[90] K. Budil, B. Remington, T. Peyser, K. Mikaelian, P. Miller, N. Woolsey, W. Wood-Vasey, and A. Rubenchik, "Experimental comparison of classical versus ablative Rayleigh-Taylor instability," *Physical Review Letters*, vol. 76, no. 24, p. 4536, 1996.

[91] R. Betti, V. Goncharov, R. McCrory, and C. Verdon, "Growth rates of the ablative Rayleigh-Taylor instability in inertial confinement fusion," *Physics of Plasmas*, vol. 5, no. 5, pp. 1446–1454, 1998.

[92] J. Sanz, J. Ramirez, R. Ramis, R. Betti, and R. Town, "Nonlinear theory of the ablative Rayleigh-Taylor instability," *Physical Review Letters*, vol. 89, no. 19, p. 195002, 2002.

[93] H. Azechi, T. Sakaiya, S. Fujioka, Y. Tamari, K. Otani, K. Shigemori, M. Nakai, H. Shiraga, N. Miyanaga, and K. Mima, "Comprehensive diagnosis of growth rates of the ablative Rayleigh-Taylor instability," *Physical Review Letters*, vol. 98, p. 045002, 2007.

[94] B. A. Remington, H.-S. Park, D. T. Casey, R. M. Cavallo, D. S. Clark, C. M. Huntington, C. C. Kuranz, A. R. Miles, S. R. Nagel, K. S. Raman, and V. A. Smalyuk, "Rayleigh-Taylor instabilities in high-energy density settings on the National Ignition Facility," in *Proceedings of the National Academy of Sciences*, National Academy of Sciences, 2018.

[95] A. Miles, M. Edwards, and J. Greenough, "Effect of initial conditions on two-dimensional Rayleigh-Taylor instability and transition to turbulence in planar blast-wave-driven systems," *Physics of Plasmas*, vol. 11, no. 11, pp. 5278–5296, 2004.

[96] C. Kuranz, R. Drake, M. Grosskopf, A. Budde, C. Krauland, D. Marion, A. Visco, J. Ditmar, H. Robey, B. Remington, A. Miles, A. Cooper, C. Sorce, T. Plewa, N. Hearn, K. Killebrew, J. Knauer, D. Arnett, and T. Donajkowski, "Three-dimensional blast-wave-driven Rayleigh-Taylor instability and the effects of long-wavelength modes," *Physics of Plasmas*, vol. 16, p. 056310, 2009.

[97] A. Miles, M. Edwards, B. Blue, J. Hansen, H. F. Robey, R. Drake, C. Kuranz, and D. Leibrandt, "The effect of a short-wavelength mode on the evolution of a long-wavelength perturbation driven by a strong blast wave," *Physics of Plasmas*, vol. 11, no. 12, p. 5507, 2004.

[98] S. Abarzhi, "Coherent structures and pattern formation in Rayleigh-Taylor turbulent mixing," *Physica Scripta*, vol. 78, p. 015401, 2008.

[99] R. Drake, H. Robey, O. Hurricane, Y. Zhang, B. Remington, J. Knauer, J. Glimm, D. Arnett, J. Kane, K. Budil, and J. Grove, "Experiments to produce a hydrodynamically unstable, spherically diverging system of relevance to instabilities in supernovae," *Astrophysical Journal*, vol. 564, pp. 896–908, 2002.

[100] C. Kuranz, H.-S. Park, B. Remington, R. Drake, A. Miles, H. Robey, J. Kilkenny, C. Keane, D. Kalantar, C. Huntington, C. Krauland, E. Harding, M. Grosskopf, D. Marion, F. Doss, E. Myra, B. Maddox, B. Young, J. Kline, G. Kyrala, T. Plewa, J. Wheeler, W. Arnett, R. Wallace, E. Giraldez, and A. Nikroo, "Astrophysically relevant radiation hydrodynamics experiment at the National Ignition Facility," *Astrophysics and Space Science*, vol. 336, pp. 207–211, 2011.

[101] C. Kuranz, H.-S. Park, C. Huntington, A. Miles, B. Remington, T. Plewa, M. Trantham, H. Robey, D. Shvarts, A. Shimony, K. Raman, S. MacLaren,

W. Wan, F. Doss, J. Kline, K. Flippo, G. Malamud, T. Handy, S. Prisbrey, C. Krauland, S. Klein, E. Harding, R. Wallace, M. J. Grosskopf, D. Marion, D. Kalantar, E. Giraldez, and R. Drake, "How high energy fluxes may affect Rayleigh-Taylor instability growth in young supernova remnants," *Nature Communications*, vol. 9, no. 1564, 2018.

[102] J. Kane, D. Arnett, B. Remington, S. Glendinning, G. Bazan, R. Drake, B. Fryxell, R. Teyssier, and K. Moore, "Scaling supernova hydrodynamics to the laboratory," *Physics of plasmas*, vol. 6, no. 5, pp. 2065–2071, 1999.

[103] H. Robey, J. Kane, B. Remington, R. Drake, O. Hurricane, H. Louis, R. Wallace, J. Knauer, P. Keiter, D. Arnett, and D. Ryutov, "An experimental testbed for the study of hydrodynamic issues in supernovae," *Physics of Plasmas*, vol. 8, no. 5, pp. 2446–2453, 2001.

[104] K. Nagai, C. Musgrave, and W. Nazarov, "A review of low density porous materials used in laser plasma experiments," *Physics of Plasmas*, vol. 25, p. 030501, 12018.

[105] A. Miles, D. Braun, M. Edwards, H. Robey, R. Drake, and D. Leibrandt, "Numerical simulation of supernova-relevant laser-driven hydro experiments on OMEGA," *Physics of Plasmas*, vol. 11, no. 7, pp. 3631–3645, 2004.

[106] C. Kuranz, R. Drake, E. Harding, M. Grosskopf, H. Robey, B. Remington, M. Edwards, A. Miles, T. Perry, B. Blue, T. Plewa, N. Hearn, J. Knauer, D. Arnett, and D. Leibrandt, "Two-dimensional blast-wave-driven Rayleigh-Taylor instability: Experiment and simulation," *Astrophysical Journal*, vol. 696, no. 1, p. 749, 2009.

[107] R. Drake, D. Leibrandt, E. Harding, C. Kuranz, M. Blackburn, H. Robey, B. Remington, M. Edwards, A. Miles, T. Perry, R. Wallace, H. Louis, J. Knauer, and D. Arnett, "Nonlinear mixing behavior of the three-dimensional Rayleigh-Taylor instability at a decelerating interface," *Physics of Plasmas*, vol. 11, no. 5, pp. 2829–2837, 2004.

[108] C. Kuranz, B. E. Blue, R. Drake, H. Robey, J. Hansen, J. Knauer, M. Grosskopf, C. Krauland, and D. C. Marion, "Dual, orthogonal, backlit pinhole radiography in OMEGA experiments," *Review of Scientific Instruments*, vol. 77, pp. 10E327–1–4, 2006.

[109] C. Kuranz, R. Drake, M. Grosskopf, B. Fryxell, A. Budde, J. Hansen, A. Miles, T. Plewa, N. Hearn, and J. Knauer, "Spike morphology in blast-wave-driven instability experiments," *Physics of Plasmas*, vol. 17, no. 052709, 2010.

[110] R. Drake, "Spike penetration in blast-wave-driven instabilities," *Astrophysical Journal*, vol. 744, no. 2, 2012.

[111] C. Di Stefano, C. Kuranz, P. Keiter, S. Klein, D. Marion, and R. Drake, "Late-time breakup of laser-driven hydrodynamics experiments," *High Energy Density Physics*, vol. 8, pp. 360–365, 2012.

[112] H. Robey, Y. Zhou, and A. Buckingham, "The time scale for the transition to turbulence in a high reynolds number, accelerated flow," *Physics of Plasmas*, vol. 10, no. 3, pp. 614–622, 2003.

[113] S. Nagel, K. Raman, C. Huntington, S. MacLaren, P. Wang, M. Barrios, T. Baumann, J. Bender, L. Benedetti, D. Doane, S. Felker, P. Fitzsimmons, K. Flippo, J. Holder, D. Kaczala, T. Perry, R. Seugling, L. Savage, and Y. Zhou, "A platform for studying the Rayleigh-Taylor and Richtmyer-Meshkov instabilities in a planar geometry at high energy density at the National Ignition Facility," *Physics of Plasmas*, vol. 24, pp. 072704–1–10, 2017.

[114] Y. Zhang, R. Drake, and J. Glimm, "Numerical evaluation of the impact of laser preheat on interface structure and instability," *Physics of Plasmas*, vol. 14, p. 062703, 2007.

[115] `http://www.mathworks.com/matlabcentral/fileexchange/11442-photonattenuation`. Original Matlab code was written in 2006 by Jarek Tuszynski (SAIC) and published as package "PhotonAttenuation". Tables are based on "X-Ray Attenuation and Absorption for Materials of Dosimetric Interest" (XAAMDI) database (NIST 5632 report): J. Hubbell and S.M. Seltzer, "Tables of X-Ray Mass Attenuation Coefficients and Mass Energy-Absorption Coefficients 1 keV to 20 MeV for Elements Z = 1 to 92 and 48 Additional Substances of Dosimetric Interest," National Institute of Standards and Technology report NISTIR 5632 (1995).

[116] S. Glendinning, J. Bolstad, D. Braun, M. Edwards, W. Hsing, B. Lasinski, H. Louis, A. Miles, J. Moreno, T. Peyser, B. Remington, H. Robey, E. Turano, C. Verdon, and Y. Zhou, "Effect of shock proximity on Richtmyer-Meshkov growth," *Physics of Plasmas*, vol. 10, no. 5, p. 1931, 2003.

[117] M. Barrios, S. Regan, K. Fournier, R. Epstein, R. Smith, A. Lazicki, R. Rygg, D. Fratanduono, J. Eggert, H.-S. Park, C. Huntington, D. Bradley, L. Landen, and G. Collins, "X-ray area backlighter development at the National Ignition Facility," *Review of Scientific Instruments*, vol. 85, p. 11D502, 2014.

[118] D. Matthews, E. Campbell, N. Ceglio, G. Hermes, A. Kauffman, L. Koppel, A. Lee, K. Manes, V. Rupert, V. Slivinsky, R. Turner, and F. Ze, "Characterization of laser-produced plasma x-ray sources for use in x-ray radiography," *Journal of Applied Physics*, vol. 54, no. 8, pp. 4260–4268, 1983.

[119] A. Bullock, O. Landen, B. Blue, J. Edwards, and D. Bradley, "X-ray induced pinhole closure in point-projection x-ray radiography," *Journal of Applied Physics*, vol. 100, p. 043301, 2006.

[120] J. Fein, J. Peebles, P. Keiter, J. Holloway, S. Klein, C. Kuranz, M.-E. Manuel, and R. Drake, "Investigation of the hard x-ray background in backlit pinhole imagers," *Review of Scientific Instruments*, vol. 85, p. 11E610, 2014.

[121] B. Blue, J. Hansen, M. Tobin, D. Eder, and H. Robey, "Debris mitigation in pinhole-apertured point-projection backlit imaging," *Review of Scientific Instruments*, vol. 75, pp. 4775–4777, 2004.

[122] N. Lanier, J. Cowan, and J. Workman, "Characterization and cross calibration of Agfa D4, D7, and D8 and Kodak SR45 x-ray films against direct exposure film at 4.0-5.5 keV," *Review of Scientific Instruments*, vol. 77, p. 043504, 2006.

[123] A. Miles, "Blast-wave-driven instability as a vehicle for understanding supernova explosion structure," *Astrophysical Journal*, vol. 696, pp. 498–514, 2009.

[124] Prism Computational Sciences, Inc. `http://www.prism-cs.com/Software/Propaceos/major_features.html`. Accessed: 2019-09-12.

[125] C. Di Stefano, G. Malamud, C. Kuranz, S. Klein, and R. Drake, "Measurement of Richtmyer-Meshkov mode coupling under steady shock conditions and at high energy density," *High Energy Density Physics*, vol. 17, pp. 263–269, 2015.

[126] W. Wan, G. Malamud, A. Shimony, C. Di Stefano, M. Trantham, S. Klein, D. Shvarts, C. Kuranz, and R. Drake, "Observation of single-mode, Kelvin-Helmholtz instability in a supersonic flow," *Physical Review Letters*, vol. 115, p. 145001, 2015.

[127] C. Di Stefano, A. Rasmus, F. Doss, K. Flippo, J. Hager, J. Kline, and P. Bradley, "Multimode instability evolution driven by strong, high-energy-density shocks in a rarefaction-reflected geometry," *Physics of Plasmas*, vol. 24, p. 052101, 2017.

[128] C. Huntington, A. Shimony, M. Trantham, C. K. D. Shvarts, C. Di Stefano, F. Doss, R. Drake, K. Flippo, D. Kalantar, S. Klein, J. Kline, S. MacLaren, G. Malamud, A. Miles, S. Prisbrey, K. Raman, B. Remington, H. Robey, W. Wan, and H.-S. Park, "Ablative stabilization of Rayleigh-Taylor instabilities resulting from a laser-driven radiative shock," *Physics of Plasmas*, vol. 25, p. 052118, 2018.

[129] Y. Aglitskiy, A. Velikovich, M. Karasik, A. Schmitt, V. Serlin, J. Weaver, J. Oh, S. Obenschain, and K. Cochrane, "Absolute Hugoniot measurements for CH foams in the 29 Mbar range," *Physics of Plasmas*, vol. 25, p. 032705, 2018.

[130] J. Colvin, H. Matsukuma, K. Brown, J. Davis, G. Kemp, K. Koga, N. Tanaka, A. Yogo, Z. Zhang, H. Nishimura, and K. Fournier, "The effects of microstructure on propagation of laser-driven radiative heat waves in under-dense high-Z plasma," *Physics of Plasmas*, vol. 25, p. 032702, 2018.